TAMPEREEN TEKNILLINEN YLIOPISTO
TAMPERE UNIVERSITY OF TECHNOLOGY

Saara Söyrinki

Structured ZnO and Al_2O_3/Ag Surfaces

Antibacteriality, Photocatalytic Activity and Durability

Julkaisu 1599 • Publication 1599

Tampere 2018

Tampereen teknillinen yliopisto. Julkaisu 1599
Tampere University of Technology. Publication 1599

Saara Söyrinki

Structured ZnO and Al_2O_3/Ag Surfaces

Antibacteriality, Photocatalytic Activity and Durability

Thesis for the degree of Doctor of Science in Technology to be presented with due permission for public examination and criticism in Konetalo Building, Auditorium K1702, at Tampere University of Technology, on the 29th of November 2018, at 12 noon.

Tampereen teknillinen yliopisto - Tampere University of Technology
Tampere 2018

Doctoral candidate: Saara Söyrinki, M. Sc.
Laboratory of Materials Science
Faculty of Engineering Sciences
Tampere University of Technology
Finland

Supervisor: Erkki Levänen, Dr. Tech., Prof.
Laboratory of Materials Science
Faculty of Engineering Sciences
Tampere University of Technology
Finland

Instructors: Juha-Pekka Nikkanen, Dr. Tech.
Laboratory of Materials Science
Faculty of Engineering Sciences
Tampere University of Technology
Finland

Erkki Levänen, Dr. Tech., Prof.
Laboratory of Materials Science
Faculty of Engineering Sciences
Tampere University of Technology
Finland

Pre-examiners: Suresh Pillai, PhD, Prof.
Nanotechnology and Bio-Engineering Research Division
Institute of Technology Sligo
Ireland

Jari Koskinen, Dr. Tech., Prof.
Department of Chemistry and Materials Science
Aalto University
Finland

Opponents: Suresh Pillai, PhD, Prof.
Nanotechnology and Bio-Engineering Research Division
Institute of Technology Sligo
Ireland

Markku Leskelä, Dr. Tech., Prof.
Department of Chemistry
University of Helsinki
Finland

ISBN 978-952-15-4265-7 (printed)
ISBN 978-952-15-4276-3 (PDF)
ISSN 1459-2045

Abstract

Functional coatings, i.e. coatings that possess a property that adds a desirable function onto a surface, offer great potential in numerous situations when specific requirements of a material must be fulfilled. Self-cleaning and antibacterial properties are useful in many cases, for instance in factories to reduce costs caused by washing processes or in hospitals to prevent bacterial infections. The self-cleaning property can be obtained with superhydrophobic, in other words highly water repellent, coatings. Besides the superhydrophobic surface, a photocatalytic surface also possesses self-cleaning capability. Photocatalysis is a phenomenon induced by light that can lead to oxidation and reduction reactions and further decomposition of organic pollutants. Photocatalytic surfaces exhibit antibacterial properties. There are also numerous metals that possess antibacterial properties, especially in the form of nanoparticles. In fact, silver is one of the most studied and used metal in antibacterial applications.

In this study, we have prepared, analyzed, and investigated the properties of two self-cleaning, antibacterial surfaces: a superhydrophobic silver-containing coating and a photocatalytic ZnO film. ZnO is a photocatalyst with an additional antibacterial property that is attributed to its semiconductor properties, in addition to the toxicity of zinc ions against bacteria. In this work, we have demonstrated a route for preparing superhydrophobic silver-containing coatings and studied their antibacterial efficiency. We have also studied the effect of synthesis parameters on the structure of ZnO films. The influence of the structure of the ZnO film on functional properties, photocatalytic, and antibacterial activity has also been investigated. Moreover, we have demonstrated the functionality of silver-containing superhydrophobic surfaces as effective antibacterial coatings. The approach of using two functional mechanisms, superhydrophobicity and antibacterial silver, offers great potential for self-cleaning applications. In addition, this study shows the antibacterial effectiveness of ZnO in dark conditions as well as the relatively high photocatalytic activity of structured ZnO films, on the basis of which we can anticipate enhanced antibacterial activity under irradiation. The chemical stability of the surfaces has been investigated in order to estimate the usability of the surfaces in varying environments. Based on the knowledge obtained in this study, the prospects of using superhydrophobic silver-containing coatings and ZnO films in applications requiring antibacterial and self-cleaning properties are discussed.

Preface

This work was carried out in the Laboratory of Materials Science, Tampere University of Technology. Prof. Erkki Levänen and Dr. Juha-Pekka Nikkanen, to whom I want to express my deepest gratitude for all the help and support, supervised the work. I also want to thank Docent Elina Huttunen-Saarivirta, who provided me valuable guidance over the years.

I am grateful to Dr. Matti Kannisto for all the collaboration and help in this process. I also want to thank Dr. Mari Raulio, Dr. Outi Priha, Dr. Erna Storgårds, Dr. Hanna Hakola, Mr. Jarmo Laakso and Mr. Leo Hyvärinen, Dr. Kimmo Kaunisto, and Prof. Matti Karp for your support, which helped to complete this thesis. I wish to thank Mrs. Marja Asp-Lehtinen and Mrs. Anne-Maarit Tikkanen for your assistance with the AAS measurements, and my colleagues Mr. Aaretti Kaleva, Dr. Matti Järveläinen, Mr. Arnold Ismailov, Mr. Amandeep Singh, Ms. Niina Merilaita, Ms. Nelli Palmu, Dr. Elisa Isotahdon, Dr. Jouni Puranen, Mrs. Sari Lehikoinen, Dr. Arto Ojuva, Professor Emeritus Tapio Mäntylä, Mrs. Merja Ritola, Mrs. Annukka Viitanen, Dr. Hannu Sippola, Dr. Mari Honkanen, Ms. Anna Nykänen, Dr. Xiaoxue Zhang, and all the others who have shared this journey with me and helped me to become a better researcher and a happier person.

The research for this work was funded by Finnish Funding Agency for Technology and Innovation (Tekes) and the Academy of Finland.

Finally, I would like to thank all my friends and my family, especially my sister and my brothers. Thank you mom for everything you have done and being always there for us, and my father for supporting and encouraging us to study and work hard. A special thanks to Markus who is my biggest supporter, and Vilja, my amazing little girl.

Tampere 11.10.2018

Saara Söyrinki

Contents

List of Figures

List of Tables

List of symbols and abbreviations

Symbols

f_1	fraction of the solid surface in contact with liquid
f_2	fraction of the air in contact with liquid
γ_{SV}	surface energy on solid-vapor interface
γ_{SL}	surface energy on solid-liquid interface
γ_{LV}	surface energy on liquid-vapor interface
r	roughness
θ_A	apparent contact angle (Cassie-Baxter state)
θ_R	contact angle of a rough surface (Wenzel state)
θ_Y	Young contact angle
θ_{Adv}	advancing contact angle
θ_{Rec}	receding contact angle
θ_1	contact angle on smooth solid surface

Abbreviations

A	acceptor
Abs	absorption
AgCl	silver chloride
$AgNO_3$	silver nitrate
ALD	atomic layer deposition
Al_2O_3	aluminum oxide
$CF_3(CF_2)_7CH_2$-$CH_2Si(OCH_3)_3$	(heptadecafluoro-1,1,2,2-tetrahydrodecyl)trimethoxysilane

$CH_3OCH_2CH_2OH$	2-methoxyethanol
C_2H_5OH	ethanol
C_3H_7OH	isopropyl alcohol
$C_4H_6O_4Zn{\cdot}2H_2O$	zinc acetate dihydrate
$C_6H_{10}O_3$	ethyl acetoacetate
$C_6H_{12}N$	hexamethylenetetramine
$C_6H_{12}O_6$	glucose
$C_{12}H_{27}AlO_3$	aluminum tri-sec-butoxide
$CuK\alpha$	L to K transition radiation in copper
$Cu(NO_3)_2{\cdot}3H_2O$	copper nitrate trihydrate
CuO	copper oxide
D	donor
DNA	deoxyribonucleic acid
e^-	electron
e_{CB}^-	conduction band electron
E	energy
EDS	energy dispersive X-ray spectroscopy
EIS	electrochemical impedance spectroscopy
eV	electron volt
FAS	(heptadecafluoro-1,1,2,2-tetrahydrodecyl)trimethoxysilane
FESEM	field emission scanning electron microscopy
H^+	proton
h^+	electron hole
h_{VB}^+	valence band hole
HMTA	hexamethylenetetramine

H_2O	water
H_2O_2	hydrogen peroxide
KCl	potassium chloride
NaOH	sodium hydroxide
$NH_2CH_2CH_2OH$	ethanolamine
NH_3	ammonia
NiO	nickel oxide
OH^-	hydroxyl group
OCP	open circuit potential
ROS	reactive oxygen species
rpm	revolutions per minute
R-SH	sulfhydryl
TiO_2	titanium dioxide
UV-vis	ultraviolet-visible
$Zn(NO_3)_2 \cdot 6H_2O$	zinc nitrate hexahydrate
ZnO	zinc oxide
$Zn(OH)_2$	zinc hydroxide
$Zn(OH)_4^{2-}$	tetrahydroxozincate ion
$Zn(NH_3)_4^{2+}$	tetraamine zinc (II) complex
$Zn(NH_4)_2^{+}$	diammonium zinc complex

List of Publications

I. **S. Heinonen**, J.-P. Nikkanen, J. Laakso, M. Raulio, O. Priha, E. Levänen, Bacterial growth on a superhydrophobic surface containing silver nanoparticles, *IOP Conf Series: Mater Sci Eng* 47 (2013) 012064.

II. **S. Heinonen**, E. Huttunen-Saarivirta, J.-P. Nikkanen, M. Raulio, O. Priha, J. Laakso, E. Storgårds, E. Levänen, Antibacterial properties and chemical stability of superhydrophobic silver-containing surface produced by sol-gel route, *Colloids Surf* A *Physicochem Eng Asp 453* (2014) 149–161.

III. **S. Heinonen**, M. Kannisto, J.-P. Nikkanen, E. Huttunen-Saarivirta, M. Karp, E. Levänen, Photocatalytic and antibacterial properties of ZnO films with different surface topographies on stainless steel substrate, *Thin Solid films* 616 (2016) 842–849.

IV. **S. Heinonen**, J.-P. Nikkanen, H. Hakola, E. Huttunen-Saarivirta, M. Kannisto, E. Levänen, Effect of temperature and concentration of precursors on morphology and photocatalytic activity of zinc oxide thin films prepared by hydrothermal route*, IOP Conf Series: Mater Sci Eng* 123 (2016) 012030.

V. **S. Heinonen**, J.-P. Nikkanen, A. Kaleva, L. Hyvärinen and E. Levänen, Structured ZnO films: Effect of copper nitrate addition to precursor solution on topography, band gap energy and photocatalytic activity, *IOP Conf Series: Mater Sci Eng* 175 (2017) 012042.

VI. **S. Heinonen**, J.-P. Nikkanen, E. Huttunen-Saarivirta, E. Levänen, Investigation of long-term chemical stability of structured ZnO films in aqueous solutions of varying conditions. *Thin Solid Films* 638 (2017) 410–419.

Author's contribution

I. The author planned and executed the experimental work including synthesis of superhydrophobic silver doped films and characterization except for the antibacterial tests that were performed by Dr. Mari Raulio and Dr. Outi Priha and SEM imaging that was conducted by Jarmo Laakso M.Sc. The author analyzed the results and wrote the paper considering the viewpoints of the co-authors.

II. The author planned and executed the experimental work including synthesis of superhydrophobic silver doped films and characterization except for the antibacterial tests that were performed by Dr. Mari Raulio and Dr. Outi Priha and the electrochemical characterizations and interpretations that were performed by Adjunct Professor Elina Huttunen-Saarivirta. The SEM imaging was performed by Jarmo Laakso M.Sc. The author analyzed the results and wrote the paper in co-operation with Adjunct Professor Huttunen-Saarivirta and Dr. Juha-Pekka Nikkanen, who participated in the writing as second and third authors.

III. The author planned and executed the experimental work including synthesis of ZnO films and characterization except for the photocatalytic activity tests that were performed by Dr. Juha-Pekka Nikkanen and the antibacterial tests and analysis that were performed by Dr. Matti Kannisto. In addition, the XRD analysis was performed by Leo Hyvärinen M.Sc. The author analyzed the results and wrote the paper except for the parts covering the antibacterial activity of the surfaces, which were written by Dr. Matti Kannisto.

IV. The author planned and executed the experimental work including synthesis of ZnO films and characterization except for photocatalytic activity tests that were performed by Dr. Juha-Pekka Nikkanen and the XRD analysis that was performed by Leo Hyvärinen M.Sc. The author analyzed the results and wrote the paper considering the viewpoints of the co-authors.

V. The author planned and executed the experimental work including synthesis of doped ZnO films and characterization except for XRD analysis that was

performed by Leo Hyvärinen M.Sc. The band gap measurements were executed with the assistance of Dr. Juha-Pekka Nikkanen and Dr. Kimmo Kaunisto. The author analyzed the results and wrote the paper considering the viewpoints of the co-authors.

VI. The author planned and executed the experimental work including synthesis of ZnO films and characterization except for XRD analysis that was performed by Leo Hyvärinen M.Sc. The author analyzed the results and wrote the paper considering the viewpoints of the co-authors.

Additional contribution

Supplementary band gap measurements were conducted and the results were analyzed by the author with the assistance of Dr. Juha-Pekka Nikkanen and Dr. Kimmo Kaunisto.

1 1 INTRODUCTION TO FUNCTIONAL SURFACES AND THIS THESIS

In this chapter, the concept of functional surfaces is introduced. The motivation and aims, as well as the structure of the work are also described.

1.1 Functional surfaces

Surfaces are present everywhere around us. The requirements of the surface depend on the purpose of the use and the environment that they have interfaces with. Surfaces can be coated for protective, decorative, or functional purposes. Compared to protective or decorative coatings, functional coatings possess an additional functionality such as anti-abrasive, anti-corrosion, antifouling, easy-to-clean, or antibacterial property. A common feature related to functional coatings is that the coating is of particular benefit for some application requirement. In addition to a specific property of functional coatings, they often need to satisfy additional requirements such as tailored surface morphology, durability, and cost effectiveness. The functionality of coatings can be generated by means of chemical, physical, mechanical, and thermal properties. Some material properties and the functional applications based on those properties are presented in Fig. 1. [1]

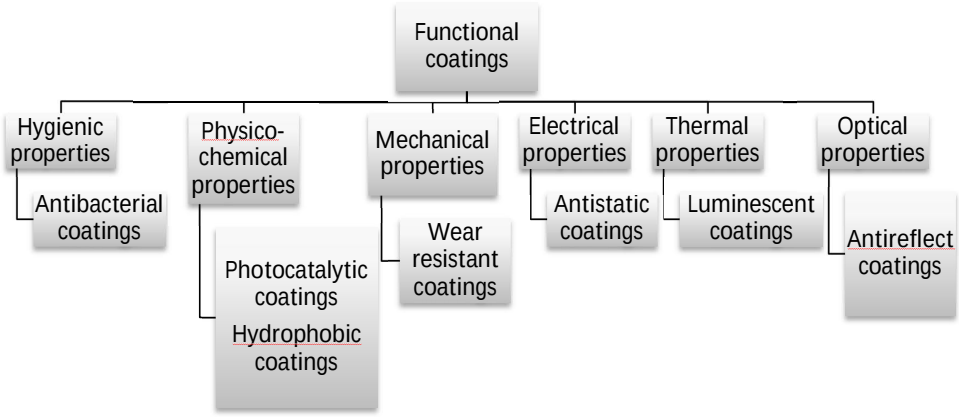

FIGURE 1 Functional coatings based on different material properties. Adapted from ref. [1]

Surface structure plays an important role in many functional coatings. Self-cleaning superhydrophobic surfaces, for instance, have a property known as the Lotus effect, which results from a combination of a certain surface structure, and physico-chemical properties of the coating. Self-cleaning properties can also result from the photocatalytic activity of a material such as TiO_2 or ZnO, when organic waste is decomposed from the surface due to radiation-catalyzed chemical reactions taking place on the surface. The photocatalytic activity of a material also enables the anti-fogging property due to the changed chemical properties of the surface catalyzed by irradiation.

Recently, nanomaterials as well as nanostructured coatings have been the center of attention due to the unique properties resulting from their small particle and structure size and high surface area to volume ratio. In coatings, nanostructured topography provides a large surface area and in many cases enhances the functional properties of the material. This is the case for instance, in antibacterial coatings with functionality based on dissolution of ions from the surface, in which case a larger surface area provides higher solubility. The durability of the coating is essential for nanostructured coatings and thin films as well as other structured coatings that have morphology-dependent functionality. Surfaces often bear both mechanical and chemical loads and without adequate durability against this exposure, the functionality of the surface is easily lost when the chemical properties and morphological characteristics of the surface are changed. Sometimes the solution to the low durability of the coating is to reproduce the coating after it has worn off, but this kind of solution is neither an economic nor environment friendly solution.

1.2 Motivation and aims of the work

Environmental applications and microorganism inactivation offer solutions to the problems caused by pollution and infections that are spreading worldwide. Development of functional coatings enables the fighting against the serious threats that our planet is facing. Consequently, the main focus of this thesis is on the development and study of the properties of self-cleaning surfaces, represented by both superhydrophobic surfaces and photocatalytic surfaces, and the deactivation of microorganisms by using antimicrobial agents or photocatalytic surfaces.

More precisely, the focal point of the study is on synthesizing antibacterial and photocatalytic coatings and thin films and enhancing both antibacterial and photocatalytic activity by modifying the surface structure. The photocatalytic activity of the surface is of great interest because it enhances antibacterial activity under irradiation. Various mate-

rials have exhibited an antimicrobial tendency, functioning by different mechanisms. Silver, especially in the form of ions and nanoparticles, has been shown to be effective against numerous bacterial species. [2] Zinc oxide, on the other hand, has also shown high antibacterial activity and functions by different mechanisms, making it effective in varying environments. [3] Since the dissolution of ions plays an essential role in the antibacterial activity of both Ag and ZnO, it can be assumed that increasing the surface area will lead to higher antibacterial activity.

Superhydrophobicity enhances the self-cleaning and easy-to-clean ability of surfaces. In this work, the antibacterial activity of silver-containing superhydrophobic surfaces is studied. The aim of combining two functional properties, superhydrophobicity and antibacterial activity, is to create a surface that not only kill bacteria but is also easy to clean after the bacteria have been killed. Silver is introduced to the coatings as nanoparticles.

Hydrothermal synthesis provides an easy and relatively economic route for synthesizing structured thin films. The topography of thin films can be controlled by varying the synthesis parameters, including temperature, time, and precursor concentrations. This thesis investigates both the effect of the synthesis parameters on the surface topography and the effect of surface topography on antibacterial and photocatalytic activity.

The durability of coatings is of great interest when there is a possibility of applying the surfaces in applications utilized sometimes in extreme conditions. In this thesis we have also concentrated on the study of the chemical durability of the fabricated coatings.

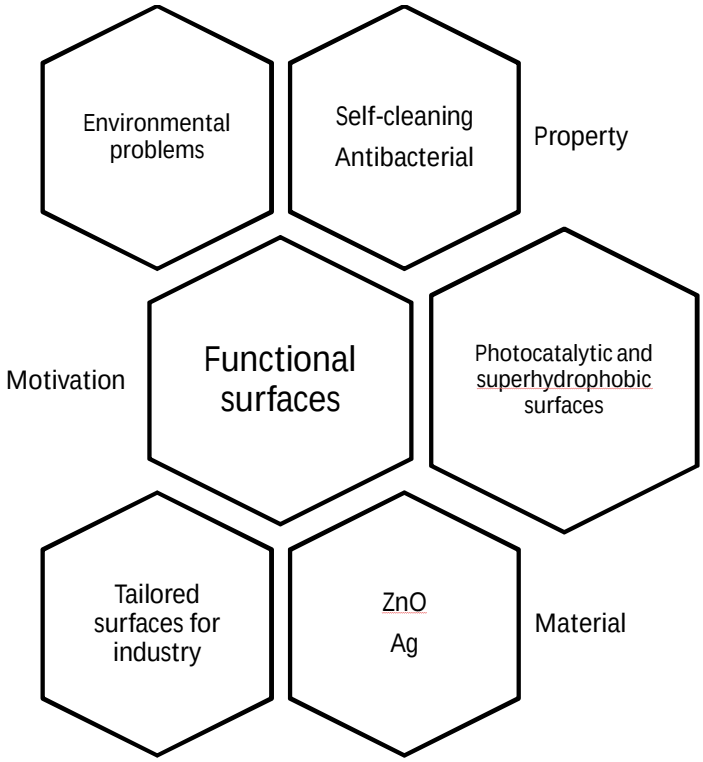

FIGURE 2 Illustration of the main themes of this study.

1.3 Structure of the thesis

This thesis consists of the introduction (Chapter 1) followed by the background on superhydrophobicity, photocatalysis and antibacterial materials. Knowledge of the above mentioned themes is provided in chapter 2. The research questions and contributions of this thesis are listed in chapter 3. Chapter 4 describes the materials and methods including the characterization methods used in this work. The results from publications I–VI are introduced in chapter 5 together with a discussion concerning the results, followed by the conclusions of the study and the future prospects in chapter 6. Publications I–VI are provided in the appendix.

2 THEORETICAL BACKGROUND ON SUPERHYDROPHOBICITY, PREPARATION AND PROPERTIES OF ZNO THIN FILMS, PHOTOCATALYSIS, AND ANTIBACTERIAL MATERIALS

This chapter describes the theoretical background of the main topics of this work including superhydrophobicity, photocatalytic activity and antibacterial silver and ZnO. An introduction to the properties and fabrication of ZnO films is also given.

2.1 Superhydrophobic surfaces

Superhydrophobic surfaces are a typical example of biomimetics, in other words the modeling of elements found in nature for use in technical solutions. Studying the superhydrophobic surfaces found in nature has provided valuable knowledge and enabled the fabrication of artificial, highly water repellent surfaces. [4] Such surfaces have huge demand and great potential for numerous applications such as self-cleaning surfaces [5]. This chapter describes superhydrophobicity as a phenomenon and illustrates the manufacturing methods and applications of superhydrophobic surfaces.

2.1.1 Superhydrophobic surfaces in nature

The leaf of the lotus flower (Nelumbo nucifera) is the most notable and commonly known plant with superhydrophobic properties. In fact, the term 'lotus effect' refers to the self-cleaning property arising from superhydrophobicity. The self-cleaning phenomenon results from water droplets rolling on the surface carrying particulates such as dirt or dust (Fig 3). [6] In the case of the lotus leaf, epicuticular wax crystalloids, which can also be termed nanostructure roughness [7], are responsible for the superhydrophobic properties. It can be said that the surface of a lotus leaf consists of micro-sized nubs covered with nano-sized hairs, i.e., nanostructure roughness (Fig. 4). This hierarchical micro/nano structure is characteristic of a superhydrophobic surface. [8]

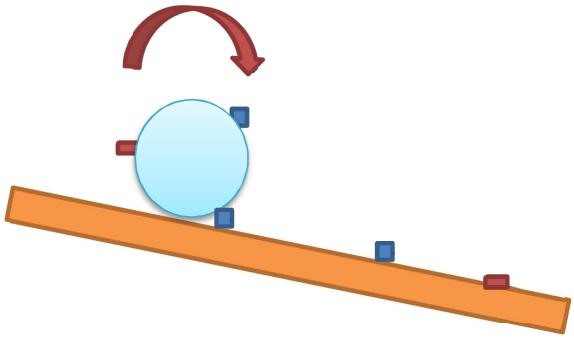

FIGURE 3 Self-cleaning effect. Water droplet rolling along the surface carrying undesired particulates. Adapted from ref. [8]

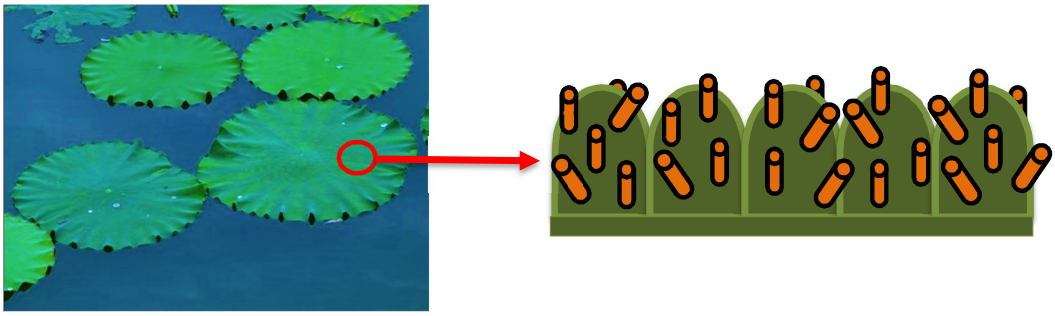

FIGURE 4 Leaf of a lotus plant and schematic picture of a hierarchical microstructure. Adapted from ref. [9]

In addition to the lotus leaf, there are also other plants and insects found in nature with similar properties. Besides the self-cleaning property, superhydrophobicity is also utilized in numerous other applications, for instance in the antireflective applications mimicking, e.g., moth eyes [10] and the wings of a butterfly [11].

2.1.2 **Superhydrophobicity**

Superhydrophobicity refers to a condition where two criteria on a surface are fulfilled: a high water contact angle (defined to be above 150º) and a low rolling angle [6,12]. Surface roughness has been found to have a profound effect on surface wetting [13]. In addition, the role of surface energy in surface wetting is significant.

In a situation where a water droplet is placed on an ideally smooth surface (Fig. 5a) under the equilibrium condition, the contact angle θ_Y between the droplet and the surface is given by the Young equation (Eq. 1) [12,14–15]:

$$cos\theta_Y = \frac{\gamma_{SV}-\gamma_{SL}}{\gamma_{LV}}, \qquad (1)$$

where γ_{SV}, γ_{SL} and γ_{LV} refer to energies on the solid-vapor, solid-liquid and liquid-vapor interfaces, respectively.

On a rough surface, the interfacial area involved is larger compared to a smooth surface. A rough surface can be either homogeneously or heterogeneously wetted (Fig. 5). The Wenzel state describes a condition where a surface is homogenously wetted, that is to say water completely penetrates the voids of the rough surface (Fig. 5 b). The Wenzel equation (Eq. 2) [15] describes the relation between the contact angle of a smooth surface (θ_Y) compared to that of a rough surface (θ_R). In Eq. 2, r refers to the roughness parameter, which is the ratio between the actual surface area that is supposed to be wetted and the projected planar area. [16] A higher roughness parameter gives a higher water contact angle.

$$cos\theta_R = rcos\theta_Y. \qquad (2)$$

In the case of the heterogeneous wetting of a rough surface, air (or a liquid other than that which the droplet consists of) is trapped between the surface and the droplet (Fig. 5 c). Such condition is described as the Cassie-Baxter state and the apparent water contact angle θ_A is given by the Cassie-Baxter equation (Eq. 3) [15]:

$$cos\theta_A = f_1 \cos\theta_1 - f_2, \qquad (3)$$

where f_1 and f_2 are the fractions of the solid surface and air in contact with liquid, respectively, and θ_1 is the contact angle for the original smooth solid surface.

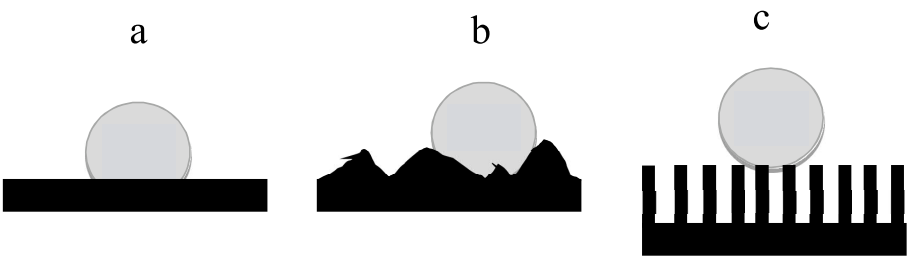

FIGURE 5 Surface models for contact angle calculations; a) smooth surface, b) rough surface, and c) rough surface with air trapped between the liquid and the solid. Adapted from ref. [17]

Both the Wenzel and Cassie-Baxter states can be suitable for superhydrophobic surfaces. There are, however, factors that are not taken into account in these models such as defects and fine structures caused by the manufacturing process. [18]

In addition to the contact angle, the contact angle hysteresis for its part also defines the stable superhydrophobic state. The contact angle hysteresis can be explained as the angle of the measured surface at which the liquid droplet slides off of the surface. Both advancing and receding contact angles can be measured. Another way to describe hysteresis is as follows: When a liquid droplet evaporates or is withdrawn carefully with a syringe from the surface, the size of the droplet decreases but the contact area between the droplet and the surface stays the same as at the beginning and thus the water contact angle decreases. At one point, the water begins to recede. On the other hand, when the water condenses on the surface, the water contact angle increases until the water droplet starts to advance. The advancing and receding angles can be measured from the moving droplet (Fig. 6). The contact angle hysteresis is the difference between those two angles. The receding and advancing angles are characteristic of the surface topography and chemistry. [19]

FIGURE 6 Receding (a) and advancing (b) angles of a moving droplet as the liquid evaporates or condenses on the surface. Adapted from ref. [19]

It must be noted that the chemical and structural properties of the surface are inhomogeneous which can cause the hysteresis and pinning of the water droplets. The concept of hysteresis and the validity of different wetting theories are complex and disputed. Nevertheless, it is evident that surface structure and roughness play essential roles where superhydrophobic surfaces are considered. [15,19]

2.1.3 Preparation, properties and applications of artificial superhydrophobic surfaces

Based on the Young, Wenzel, and Cassie-Baxter equations, it can be noticed that the water contact angle is influenced by surface roughness and surface energy. Thus, when

superhydrophobic surfaces are artificially manufactured, the aim is often to control these parameters. [15] Surface roughness can be tailored using different approaches, for instance laser patterning [20], sol–gel processing [21] or hydrothermal synthesis [22]. Surface energy, on the other hand, can be modified by choosing a substrate material with low surface energy or by adding a low surface energy layer onto the surface. Low surface energy can be achieved for instance by depositing a self-assembled monolayer of alkanethiols, fatty acids, or organic silanes on the surface. [8]

Since the preparation of superhydrophobic surfaces often requires a tailored hierarchical micro/nano multilayer surface structure, it is challenging to prepare a superhydrophobic surface for demanding conditions, e.g., with a severe mechanical or chemical load. Studying the durability of the superhydrophobic coatings is of great importance when considering them for use in a real-life environment.

Superhydrophobic surfaces have been prepared using various different methods [23] including nanoimprint and nanosphere lithography [16–18], chemical etching [24], self-assembly [25], laser patterning, [16] and the wet-chemical route [26]. Superhydrophobic surfaces can be used in a wide range of applications, e.g., self-cleaning surfaces, anti-icing surfaces such as solar cells and wind turbines, transparent and antireflective coatings, antibiofouling surfaces for ships for instance, microfluidic devices to reduce pressure loss, and in tubes or channels for drag reduction. [8,27] Several materials can be used as substrate material for superhydrophobic coatings. [15] The most convenient manufacturing method depends on the requirements of the target application.

Superhydrophobic surfaces have been shown to prevent bacteria from adhering to the surface. However, this kind of behavior has been detected only with certain bacterial species, e.g., E. *coli* [28–29], S. *aureus* [29–31] and P. *aeruginosa* [31–32]. It must be noted that bacteria prefer rough surfaces compared to smooth surfaces. However, when roughness increases over a certain level, there is no notable difference in the adhesion of the bacteria on a rough or smooth surface. There are also numerous other factors influencing bacterial adhesion such as the chemical composition of the material, associated flow conditions and temperature. [33]

2.2 ZnO thin films

The substrate material plays an important role in the fabrication of ZnO thin films. Besides the use of ZnO itself as the substrate, the most commonly used heterosubstrate is sapphire. Numerous coating methods, one of the most promising being hydrothermal

growth, can be applied when manufacturing ZnO thin films. The advantage of hydrothermal growth is the relatively low-cost and simple process. [34] The functional properties of a film can be enhanced by maximizing the surface area, by creating micro- or nanostructures on the surface. [35]

2.2.1 General properties of ZnO

Zinc oxide (ZnO) is a semiconductive compound with high thermal stability and relatively high bond polarity. ZnO most commonly crystallizes in the hexagonal wurtzite structure (Fig. 7 a). The more rarely occurring crystal structures are zinc blende (Fig. 7 b) and rock salt (Fig. 7 c). In wurtzite lattice, tetrahedrally bonded Zn and O ions form ZnO_4 groups. However, the bonds of the tetrahedra are not equal in length. The bond in the direction of the c-axis is 1.992 Å and the basal bond length is 1.973 Å, which results in a dipole moment. Since the atomic structures of different orientations vary, the properties, including electrical properties of different planes also vary, which causes phenomena like piezoelectricity. The difference in bond lengths is also important for the growth direction of the nanorods, since the polar plane attracts ions from the surrounding solution, leading to growth of the crystal in a certain direction. In the case of ZnO, nanorod arrays have a tendency to grow along the polar c-axis. [36–37] ZnO crystals are almost always n-type, meaning that electrons are responsible for carrying the charge, due to intrinsic defects such as oxygen vacancies and zinc interstitials in the lattice. There have been multiple attempts to obtain p-type conductivity, meaning that the holes are responsible for charge carrying, by doping. Moreover, there have been some reports of p-type ZnO obtained by nitrogen doping, for example. In contrast, Cu, Ag and Au are deep acceptors and cannot contribute to p-type conductivity. [38]

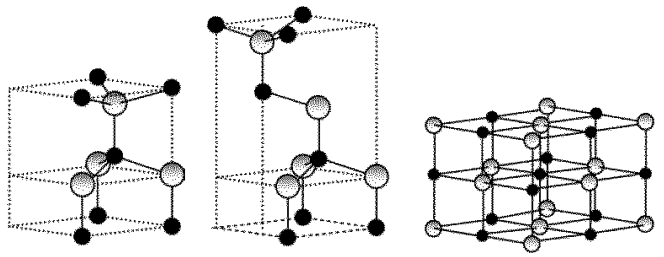

FIGURE 7 Lattice structure of a) wurtzite, b) zinc blende, and c) rock salt structured ZnO. Gray spheres denote Zn and black spheres oxygen. Adapted from ref. [39]

ZnO is attracting attention due to the large variety of applications in both scientific and industrial areas. It is used for instance as an additive in concrete and rubber, as a white pigment in paints, and also in food additives, pharmaceutics, cosmetics, and catalysts. [34]

In semiconductor device applications, ZnO is a very promising material for several reasons including the following: ZnO is available in large single crystals; it has relatively wide band gap, which allows its use in optoelectronic applications in blue/UV region; it has high thermal conductivity, which allows its use as an additive in tyres etc.; and it is a good choice as a substrate for epitaxial growth. [38]

2.2.2 **Preparation of structured ZnO thin films by hydrothermal synthesis**

Hydrothermal synthesis, i.e., an inorganic synthesis that can be used to grow single crystals in an aqueous solution at high temperature and pressure, is a commonly used method and its advantage compared to solid-state methods is sometimes higher reactivity in aqueous media which allows the use of lower temperatures. [40–41] In hydrothermal synthesis, the reactions occur in the solution. In the reactions, water acts as a catalyst and sometimes also as a component of a forming solid phase. [42] Although hydrothermal synthesis is sometimes regarded as occurring at temperatures and pressure above 100 °C and 1 bar, the concept of hydrothermal synthesis can be seen to cover the whole temperature region above room temperature and the pressure region above 1 bar. In fact, there are numerous publications describing studies performed under mild hydrothermal conditions. [43] One advantage of hydrothermal synthesis is the relatively simple experimental set-up. When elevated temperature and pressure are applied, an autoclave is normally used. In the case of synthesis with elevated temperature but ambient pressure, as in this work, the set-up is even more simple. [40–41] Hydrothermal synthesis can be used to synthesize a wide range of materials and compounds such as fluorides, sulfides, zeolites, or oxides including quartz and ZnO. Among the different methods to produce ZnO crystals, hydrothermal synthesis provides a method to obtain crystals of good quality. Another major advantage of hydrothermal method is the controllability of the synthesis. [43]

The ZnO film nanostructure is affected by numerous factors related to hydrothermal synthesis conditions, e.g., precursor solution composition. [44] Depending on the seed layer grain size, the nucleation mechanism can occur either by surface nucleation or grain-boundary nucleation. With a larger grain size (and thus higher surface roughness and lower grain boundary surface area), surface nucleation is more dominant, leading to a less dense structure with thicker and longer nanorods. [45] The grain boundaries are more thermodynamically favorable sites for nucleation, [46] possibly due to the structure

of the grain boundaries, which is less organized and contains more defects. The larger diameter and length of the nanorods on the surfaces with a larger substrate grain size (and less dense nanorod structure) can be explained by the higher amount of ions around the nucleation centers during synthesis compared to the amount of ions that surround a single nanorod in a denser structure. [45] Moreover, the precursor concentration mainly determines the diameter of the nanorods, whereas the seed layer structure plays a dominant role in the nanorod array density and orientation. [47]

Substrate pre-treatments also influence the growth of nanostructures. [48] Annealing has been shown to lead to the growth of the substrate grain size and in addition, exposure to a certain environment before the annealing also has an impact on the epitaxial growth. [45] This could be caused by the changes (i.e., defects) on the surface due to the adsorption of gas molecules from the surrounding phase. In hydrothermal synthesis, the growth of ZnO nanostructures is influenced by various factors such as the type and amount of precursors, synthesis time, temperature, and the pH of the growth solution. The process often involves the formation of $Zn(NH_4)_2^+$ and $Zn(OH)_4^{2-}$ species followed by the reactions that are presented in equations 4 and 5. [49–50]

$$Zn(NH_3)_4^{2+} + 2OH^- \rightarrow ZnO + 4NH_3 + H_2O \quad (4)$$

$$Zn(OH)_4^{2-} \rightarrow ZnO + H_2O + 2OH^- \quad (5)$$

In the hydrothermal synthesis of ZnO films, one of the precursors is often a soluble zinc salt such as zinc nitrate. OH^- ions are required for the formation of $Zn(OH)_4^{2-}$ ions and the ZnO forming reaction (Eq.4), and thus the higher pH of the growth media promotes the synthesis. [49] The Pourbaix diagram of ZnO (Fig. 8) shows that, at pH values of approximately between 5.5 and 14, ZnO is stable in aqueous solution at room temperature. The formation of crystals is affected by additives in the growth media. Additives such as hexamethylenetetramine (HMTA) and ethylene glycol are often used as templates leading to the formation of smaller crystals. [51–52] HMTA decomposes into formaldehyde and ammonia, which increases the pH of the solution and promotes the precipitation of zinc oxide and hydroxide. HMTA forms hydrogen-bonded 3D complexes with many transition metals and water. These complexes might contribute to the crystallization of the ZnO nanorod structure. However, the role of HMTA in the process is not yet fully understood. [53]

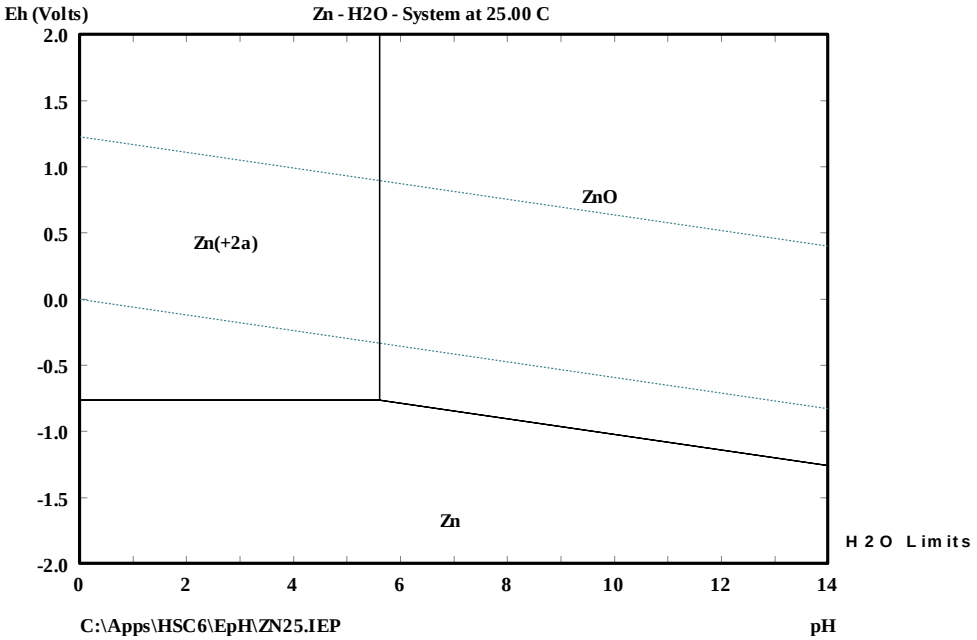

FIGURE 8 Pourbaix diagram of Zn-H_2O system at 25 ºC drawn with HSC Chemistry 6.

2.3 Photocatalysis

Photocatalysis, a phenomenon involving redox reactions on a material surface in the presence of light, enables various applications in the field of environmental protection, water purification, reduction of hazardous components [54] and micro-organism inactivation. [55] Some metal oxides with the desired band gap energy, including TiO_2 and ZnO, have demonstrated photocatalytic activity that can be utilized for the above-mentioned purposes. [56] This chapter introduces the basic mechanism of photocatalysis and concentrates on the photocatalytic activity of ZnO and the effect of metal doping on it.

2.3.1 Mechanism of photocatalysis

Photocatalysis has been defined as “acceleration of a photoreaction by the presence of a catalyst” [57]. Photoreactions occur at the surface of a catalyst in heterogeneous pho-

tocatalysis. In the process, called sensitized photoreaction, the initial photoexcitation occurs in the catalyst substrate, which then interacts with the ground state adsorbate molecule. Equation 6 summarizes the semiconductor-sensitized photoreaction:

$$A + D \xrightarrow[light \geq E_{bandgap}]{} A^- + D^+ \qquad (6)$$

As shown in equation 6, the energy of the absorbed light must be equal to or higher than the band gap of the material for a photocatalytic reaction to occur, which results in the excitation of an electron e^- from the valence band to the conduction band. Simultaneously, a photogenerated hole h^+ is created in the valence band leading to interfacial processes that involve electrons and holes, as shown in Fig. 9. [57] In these processes, redox reactions occur with gas or liquid phase adsorbed reactants. Reduction (Eq. 7) and oxidation (Eq. 8) proceed as follows [58]:

$$e_{CB}^- + A \rightarrow A^{\cdot -} \qquad (7)$$

$$h_{VB}^+ + D \rightarrow D^{\cdot +} \qquad (8)$$

For instance, the oxidation of water by holes leads to the generation of hydroxyl radicals, which are highly oxidative. [58]

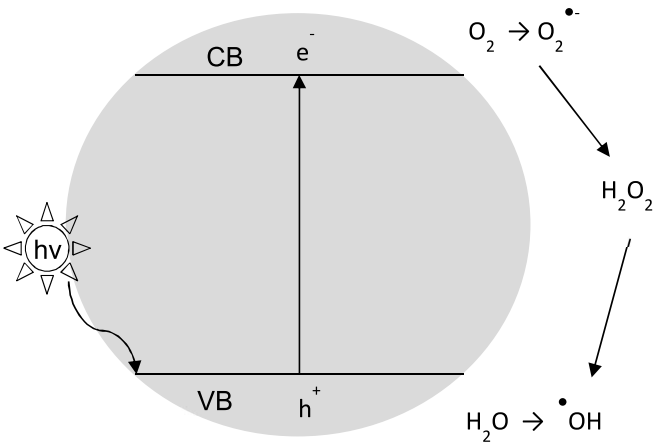

FIGURE 9 Schematic diagram of photocatalysis. Adapted from ref. [56]

2.3.2 **ZnO photocatalysis**

Intensive studying of photocatalysis has been ongoing since Fujishima et al. [59] used a TiO_2 photoelectrode for water splitting. [55] Besides TiO_2, ZnO has attracted increasing attention as a photocatalyst material, as mentioned earlier. [60–61] ZnO is a semiconductor with a direct band gap of 3.37 eV. [34] Fabrication of ZnO nanoparticles costs considerably less than the fabrication of, e.g., TiO_2 or Al_2O_3 nanoparticles. In addition, ZnO has been shown to exhibit higher absorption efficiency compared to TiO_2. [62] ZnO, however, has a tendency to photocorrosion [63] and a high recombination rate of photogenerated electron-hole pairs. In the photocorrosion, the photogenerated holes attack the Zn-O bond leading to dissolution of Zn^{2+} ion to the solution following equations 9–10. [63] The photocorrosion leads to, besides degradation of the surface, to reduced photocatalytic activity. Contradictory results have been reported when comparing the photocatalytic performances of TiO_2 and ZnO. [62,64] Clearly, it is essential to inhibit recombination and photocorrosion in order to improve the photocatalytic performance of ZnO.

$$ZnO_{(s)} + hv \rightarrow ZnO_{(s)} + h^+ + e^- \quad (9)$$

$$ZnO_{(s)} + 2h^+ \rightarrow Zn^{2+}_{(aq)} + \frac{1}{2}O_2 \quad (10)$$

In ZnO, the photogenerated electrons and holes can produce both superoxide anion radicals (Eq. 11) and hydroxyl radicals (Eq. 12). [65]:

$$e_{CB}^- + O_2 \rightarrow O_2^{\cdot -} \quad (11)$$

$$h_{VB}^+ + H_2O \rightarrow \cdot OH + H^+ \quad (12)$$

In addition, superoxide radicals can react with protons producing HO_2^- anions, which can further react with protons to form H_2O_2. Oxygen vacancies can act as electron acceptors and trap electrons, leading to a decreased recombination rate. Moreover, oxygen interstitials can trap photogenerated holes, which promotes the production of hydroxyl radicals. [66]

It has been demonstrated that different ZnO particle shapes affect the recombination kinetic parameters. [67] Doping of ZnO with metals or non-metals has been shown to enhance photocatalytic performance partly by inhibiting the recombination of photogenerated electrons and holes. Doping can also be used to modify the band gap energy. [68–69] Reducing the band gap energy is of great interest to enable the utilization of ZnO in visible light photocatalytic applications.

The most typical heterojunction system used to enhance the photocatalytic performance of ZnO is an ordinary type-II heterojunction, which is usually formed by combining two semiconductors that have adequate band location in such a way that electron-hole pair transfer occurs as demonstrated in Fig 10. Coupling ZnO with a narrow band gap semiconductor, e.g., CuO, may improve charge separation and shift the band gap of the system, enabling visible-light photocatalysis. [70–72]

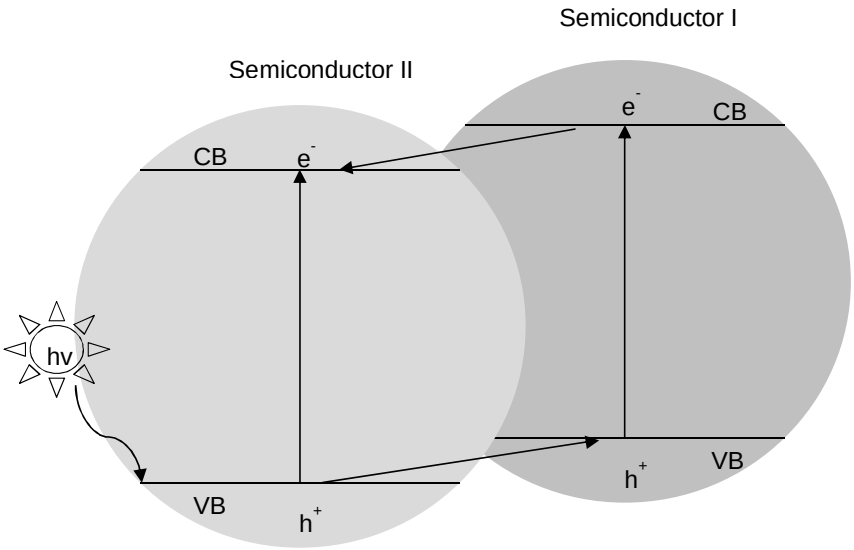

FIGURE 10 Conventional type-II heterojunction. Adapted from ref. [70]

Formation of a p-n junction is another way to separate the charge carriers by building an electric field into the photocatalytic system. In a p-n junction, the electrons in the n-type semiconductor migrate to the p-type semiconductor and holes migrate from the p-type semiconductor to the n-type semiconductor and thus an internal electric field builds up. Such a system can be achieved, e.g., by an n-type TiO_2—p-type ZnO system. Under irradiation, both materials will be excited. The generated charge carrier pairs are separated by the internal electric field. The band locations need to be appropriate in order to fulfill the thermodynamic requirements. [70–71]

Yet another heterojunction photocatalytic system is the Z-scheme heterojunction (Fig 11). In this system, photogenerated electrons of the semiconductor with higher oxidation potential migrate to the other semiconductor with higher reduction potential. Photogenerated holes are located in the semiconductor with higher oxidation potential, leading to the increased redox ability of the system. [70–71]

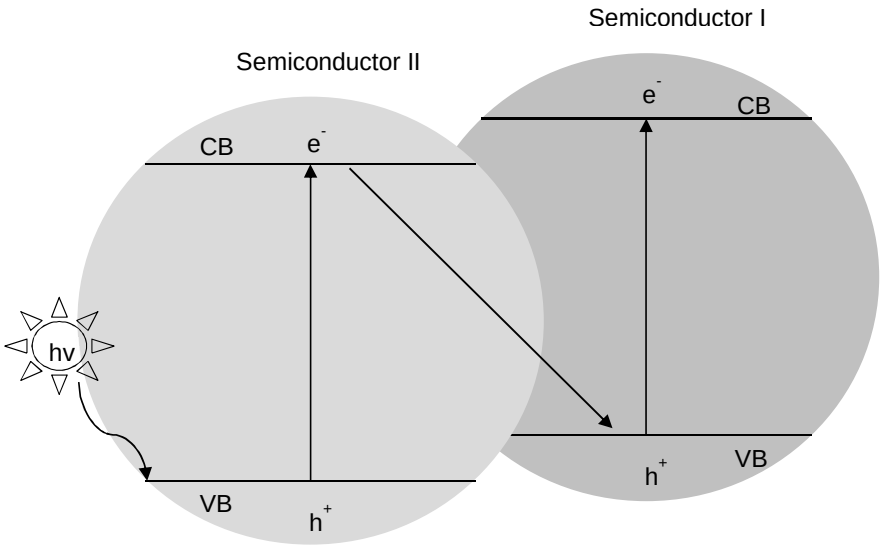

FIGURE 11 Z-scheme heterojunction for ZnO-based photocatalyst. Adapted from ref. [70]

Transition metals like Fe, Ni, Mn, and Cu can relatively easily be doped into ZnO. In the case of a metal atom creating an energy state below the conduction band of ZnO, the photogenerated electrons are trapped, which inhibits recombination. [71,73–76] Mn doping has indeed been shown to enhance the photocatalytic performance of ZnO due to the increased production of hydroxyl radicals. [77] Addition of Fe to the ZnO lattice induces electron traps near the conduction band of ZnO, which prevents recombination. [68]

Alkali metal, e.g., Na, Li, or Mg, doping can cause ZnO band gap widening and create electron traps, which also enhances photocatalytic activity by inhibiting the recombination reactions of photogenerated electrons and holes. Mg^{2+} doping can also enhance the electron trapping of oxygen vacancies. [71,78] It was found that Mg ion substitution at Zn sites enhanced photocatalytic activity by shifting the conduction band to a higher energy level whereas Mg ion substitution at the interstitial sites lowered the photocatalytic activity by producing impurity levels below the conduction band. [79] The doping of the ZnO lattice with ions such as Li changes the electrical properties of the material. The Li^{+} cation has a smaller ionic radius compared to the Zn^{2+} cation and thus Li ions are displaced from the Zn positions in the lattice, resulting in locally increased dipole moments. [37] In addition, other properties can be controlled by doping: for example, the band gap of ZnO can be modulated by addition of Mg. [80]

Noble metals such as Ag and Au in the ZnO lattice can also capture photogenerated electrons. They also enhance light absorption via surface plasmon resonance, which facilitates redox reactions. [71,81] The Fermi levels (i.e., the chemical potential of electrons) of copper and silver are below the Fermi level of ZnO. Since ZnO is typically an n-type semiconductor, the presence of electrons as charge carriers leads to the Fermi level of ZnO being near the conduction band. During excitation, electrons are transferred due to the downward band bending in the silver-ZnO system and electrons are available at the ZnO conduction band, facilitating the formation of superoxide radicals. In contrast, in copper, charges are transferred from ZnO to Cu, which inhibits recombination. [68,82] There are, however, results showing a decrease in the photocatalytic activity of Cu-doped ZnO compared to non-doped ZnO. This could be explained by increased light scattering in the presence of Cu or CuO. It is also assumed that holes in the CuO valence band are less reactive compared to holes in the ZnO valence band. [82] Moreover, the Cu concentration has been shown to play an important role. Up to a certain level, Cu doping decreases recombination but at increased Cu dopant levels, Cu starts acting as a recombination center, decreasing photocatalytic activity. [84]

Doping with non-metals like N, S, or C can generate intermediate band gap levels that enhance visible light photocatalytic performance.[84] Doping with N narrows the band gap through the hybridization of O 2p and N 2p states.[85–86] N-doped ZnO has in fact shown better photocatalytic efficiency in daylight compared to non-doped ZnO. [71,85]

Doping of ZnO can reduce the band gap energy by changing the coordination environment of Zn atoms, leading to the addition of localized electronic energy levels, as demonstrated in Fig 12. Photogenerated charge carriers are trapped on the dopant energy level that is below the conduction band. This can lead to enhanced photocatalytic activity. [71, 88–90]

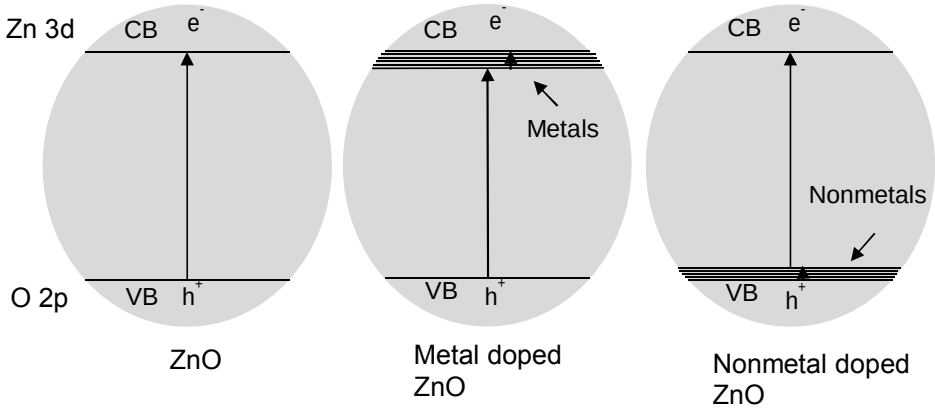

FIGURE 12 Band structures of ZnO, metal-doped ZnO, and non-metal doped ZnO. Adapted from ref. [71]

Besides doping, the structure of ZnO particles or thin films influences the photocatalytic performance of ZnO [61]. Indeed, it has been shown that ZnO nanorods on a substrate have higher photocatalytic efficiency compared to a smoother ALD grown ZnO surface. [35] In addition, the specific surface area has been shown to correlate with photocatalytic activity. [60] A smaller particle size increases the specific surface area of the powder, which obviously enables more effective creation of reactive oxygen species (ROS). The facets of the nanostructures or nanoparticles could also have an important role in photocatalytic activity since the generation of hydroxyl radicals and H_2O_2 is greater in polar facets compared to non-polar facets, due to their greater tendency to adsorb oxygen molecules and hydroxyl ions. [91–92] Moreover, it has been shown that the more polar planes there are, the more oxygen vacancies there are, and the higher the photocatalytic activity. [93]

2.4 Antibacterial metals and ZnO

In our globalizing world with people travelling around the globe, bacterial plasmids are transported between countries. Due to the antibiotic-resistant bacterial species that have been detected, [94–96] there is a growing demand for development of new, effective antibacterial materials. Numerous studies have shown that some metals, silver being perhaps the most commonly known, have the ability to inhibit bacterial growth. [2,97–113] Indeed, silver is widely used in several antibacterial applications such as in the

treatment of burn wounds, in food preservation, and in water treatment to mention a few. [108] In addition to metals, some other compounds such as CuO and NiO have proven to possess antibacterial properties. [114–115] In addition, as a very promising candidate due to its non-toxic nature, ZnO has become the central focus of antibacterial activity studies. [58,60,97–148]

2.4.1 Silver and other metal-based antibacterial agents

Bacteria as well as other living organisms need certain macronutrients and micronutrients to live. These elements start acting like toxins, if the concentration of essential elements exceed a certain level. Zn is one of these elements. Besides Zn, there are various other metals that have been shown to be toxic against different bacterial species including Ag, Au, Cu, Pb, Mo, Ni, and Co. [97,149] Three essential determinants can be highlighted when considering the antibacterial activity of metals. Firstly, donor atom selectivity, which refers to the interactions of donor ligands such as O, S, or N with metal ions, plays an important role. [150–151] These interactions are often selective and may lead to toxic metal species binding to proteins or other essential parts of the cell, leading to the rupture of the cell. According to the hard-soft acid base theory, transition metals can be ordered according to the preference for specific organic ligands, for example Cu(I), Cu(II), Ag(I), and Zn(II) have a tendency to associate tightly to sulfhydryl (R-SH) and other soft bases. [152–153] Secondly, the reduction potential of a metal describes how metal species tend to become reduced by acquiring electrons from a donor. [154] Indeed, a correlation between the toxicity of some redox-active metals and standard electron potential has been found. [155] Thirdly, speciation, which refers to the chemical form in which the metal species are present in the cell. Factors such as pH, temperature, and ionic strength determine the chemical form of the metal species. [156]

Silver is widely studied and used in antibacterial applications due to its high antibacterial efficiency and because it presents very little systemic toxicity for humans. Silver has been used as a disinfectant for several millennia [157] but extensive research on the antibacterial activity of nanosized silver especially has been ongoing for the last decade. [110] The mechanism of the action of silver-based antibacterial systems depends on several factors, including the environment of interest and physical and chemical factors, such as dissolution, aggregation, adsorption and desorption of ions, release of adsorbed species, present molecular species, and interaction with surfaces or other nanoparticles. The temperature of the system, amount of oxidizer present, composition of the medium, and presence of light also have an impact on the antibacterial action of the system. [110]

Ag^+ cations have a prevalent role in antibacterial activity of silver. The ions can be released from different systems such as salts, ionomers, or zeolites. [158–160] The Ag

ions can also be released from metallic silver via oxidative dissolution that requires presence of an oxidizer, for instance atmospheric O_2 dissolved into water. Silver ions have a high affinity for thiols as well as phosphates and organic amines. Silver forms a quasi-covalent (Ag-S) bond with thiols. [161] Silver can also form chains between thiols by acting as a bridging agent leading to the aggregation of thiol-bearing molecules. [162] In this way Ag^+ can cause the inactivation of biological systems. Some organic molecules such as DNA and peptides can be the targets of monovalent silver. However, Ag^+ cannot act selectively in the cell but will be adsorbed by any system to which it has high affinity and thus it has several pathways leading to cell death. Of such pathways, some are more sensitive to silver cations and are thus more likely to be the main cause of cell death. The large variety of pathways leading to cellular death is one reason explaining antibacterial efficiency against a large variety of bacterial species. [110]

Besides ionic silver, Ag nanoparticles have also been shown to demonstrate anti-bacterial activity by accumulating at the bacterial membrane and forming aggregates. This seems to lead to the diminution of bacterial membrane integrity, which then results in cell death. [110,163] Smaller particles have shown higher antibacterial efficiency compared to bigger silver nanoparticles. [102] However, particles within a large particle size range, from 1 nm to several hundreds of nm, have exhibited antibacterial activity. Due to the notable size difference, it seems evident that the action mechanism results, at least to some extent, from secondary species. [110] It has in fact been shown that a high level of reactive oxygen species (ROS) is observed in cells that have been treated with silver nanoparticles. [164] In these cases, it can be postulated that silver nanoparticles play a catalytic role in the formation of ROS. Another explanation for the ROS in the cells is the disruption of the scavenging pathways that have an important role in the lowering the concentration of ROS in the cell to prevent oxidation stress. [110]

Since the mode of action of antimicrobial silver is much based on monovalent silver, the conditions of the environment are in essential role in the antimicrobial efficiency. In some cases, e.g. when antibacterial activity is required on dry surfaces, some other materials may possess better functionality. For instance, copper acts antimicrobially not only through ionic interaction but also by a contact killing mechanisms which enables functioning as antimicrobial agent also in dry conditions. [165–166]

To conclude, there are several mechanisms proposed for antibacterial action of silver (Fig. 13) starting from electrostatic interactions between the cell and silver nanoparticles/cations and leading to changes in permeability, productions of ROS and leakage of the content inside the cell, interaction of silver cations with SH-groups and inhibition of protein synthesis as well as interaction with DNA molecules leading to cell death. [2]

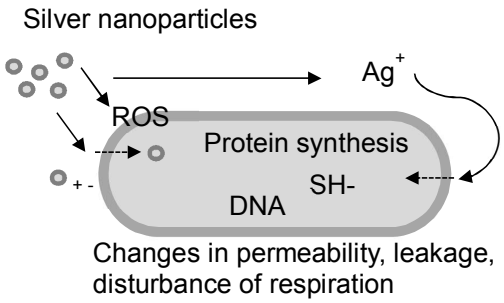

FIGURE 13 Antibacterial mechanisms of silver. Adapted from ref. [2]

2.4.2 **Antibacterial ZnO**

During recent years, ZnO has been extensively studied due to its antibacterial properties. Despite numerous studies [3,71,91,116–148], the antibacterial mechanism of ZnO is still not yet fully understood. However, it has been shown that several mechanisms contribute to the antibacterial activity of ZnO [125,147]. Such mechanisms are the release of Zn^{2+} ions [3,167], generation of reactive oxygen species (ROS), [168] and membrane dysfunction [166] caused by contact between ZnO and bacterial cells. ZnO nanoparticles may also penetrate the cell, leading to cell death. [71,170]

Toxicity related to the release of Zn^{2+} ions is explained by the interaction of zinc cations with functional groups, e.g., hydroxyl or amino groups, inside the bacterial cell. [171] Since there are several mechanisms involved in the antibacterial action, and the environment in which the antibacterial activity is studied is rather complex with numerous variables, e.g., pH and ionic strength, it is challenging to clarify comprehensively the influence of any certain mechanism. It has been shown, however, that there is no clear correlation between the Zn^{2+} concentration and antibacterial activity. [71,172] This could in fact be due to the changing media as well as variation in sensitivity of different organisms to Zn^{2+} cations. However, the contribution of Zn^{2+} ions to the antibacterial activity of ZnO is evident. [3,71]

Reactive oxygen species contribute to antibacterial activity by damaging essential cell constituents such as proteins, lipids, or DNA. [173] When ZnO is photoexcited, the antibacterial activity of ZnO is attributed mainly to the generation of ROS. [71,174] Hydroxyl radicals can react with biomolecules including DNA, amino acids, nucleic acids, lipids, and carbohydrates. [175] Hydrogen peroxide also reacts with bacterial cells contributing predominantly to the antibacterial activity of ZnO. [71,176] Since ROS have a notable

role in the antibacterial activity of ZnO, the latter can be improved by enhancing photocatalytic activity by means of metal or non-metal doping, and in the case of ZnO films, by structuring the ZnO film. Superoxide radicals can also be generated without UV irradiation via single-electron reduction. [177]

The contact-killing mechanism is based on the charges of the ZnO surface and the bacterial cells. Positively charged ZnO attracts negatively charged bacterial cells [178] and the charge balance of the cell may be disturbed, resulting in the deformation and death of the cell. [71] In fact, cell damage has been observed with different ZnO nanoparticle morphologies. [179] In addition to electrostatic forces, some weak interactions like hydrophobic interactions are involved. [131] In addition, once the cell membrane has been disturbed by the interaction between the ZnO surface and the bacterial cell, nanoparticles may penetrate the cell, leading to disruption of the bacteria. [71,180]

ZnO has exhibited antibacterial activity against several bacterial species, including both gram-positive and gram-negative bacteria. Gram-positive *S. aureus* and gram-negative *E. coli* are commonly used in antibacterial investigations. [71,147] The antibacterial efficiency of photoactivated ZnO has been shown to be higher for gram-negative bacteria, probably due to the cell wall structure, which consists of a thinner peptidoglycan layer containing proteins, phospholipids, and lipopolysaccharides, compared to the thicker peptidoglycan layer with teichoic and lipoteichoic acids of gram-positive bacteria. [91]

In the case of nanoparticles, the size of the nanoparticles has been shown to affect the antibacterial efficiency of ZnO. [181] Some studies have excluded Zn^{2+} ions from the system and nevertheless found the nanoparticle size to be related to antibacterial efficiency. [182] Thus, it can be concluded that penetration of nanoparticles into the cells and formation of ROS are most likely responsible for cell death when Zn^{2+} is not available. [71] The morphology of the nanoparticles has also been shown to influence the antibacterial efficiency of a powder. [91] The shape of the particle could affect the ability of the particles to penetrate the cells, which could explain the differences in antibacterial efficiency of different shaped particles. The facets in particles of different shape also vary. Polar facets are more active in creating ROS and they could attract bacteria due to the charge, which could lead to enhanced antibacterial activity. [93] Although the concentration of Zn^{2+} ions has not shown any clear correlation to the antibacterial activity of ZnO, the concentration of ZnO nanoparticles is correlated to the antibacterial efficiency of ZnO. [71,183]

3 RESEARCH QUESTIONS AND CONTRIBUTION OF THIS THESIS

In this thesis, the focus was on developing functional surfaces for antibacterial and self-cleaning purposes, concentrating on ceramic-based structured thin films. The testing of the chemical resistance of these films was also included as the main focus area of this work in order to evaluate their suitability for industrial use. Based on the objectives, the following research questions were asked:

I) Can superhydrophobic silver-containing coatings and structured ZnO films effectively prevent bacterial growth on surfaces?

II) How do superhydrophobic and ZnO surfaces withstand aqueous conditions?

III) How do the synthesis parameters influence the structure of hydrothermally grown ZnO film?

IV) How does the structuring of ZnO surfaces affect their functional properties?

V) How to lower the band gap energy of ZnO films in order to increase the visible-light photoactivity of films?

The contribution of this thesis is novel information on the effect of hydrothermal synthesis parameters on the morphology of a prepared ZnO film. New, more detailed knowledge on the influence of the ZnO thin film structure on antibacterial and photocatalytic activity is also presented. Ways to decrease the band gap of ZnO films are discussed. In addition, new scientific knowledge on the dissolution behavior of ZnO films in varying conditions is introduced and, based on the results obtained, their suitability for use in practical applications is evaluated. Moreover, information on the antibacterial properties and chemical stability of superhydrophobic silver-containing films is given and their use in harsh environments is considered and discussed. The combination of superhydrophobicity and antibacterial silver is aimed at the production of easy-to-clean anti-bacterial surfaces.

4 MATERIALS AND METHODS

In chapter 4, the materials used in the synthesis and experiments conducted in this thesis are listed. The preparation methods of the samples in each publication are also described. Moreover, there is a description of the characterization methods used in this work.

4.1 Materials

The following precursors were used to synthesize flake-structured aluminum oxide coatings: aluminum tri-sec-butoxide ($C_{12}H_{27}AlO_3$ > 97 %, VWR), isopropyl alcohol (C_3H_7OH > 99%, VWR), and ethyl acetoacetate ($C_6H_{10}O_3$ > 98%, VWR). Silver nanoparticles were produced on the surface using silver nitrate ($AgNO_3$, VWR), sodium hydroxide (NaOH, 65%, Prolabo), ammonia (NH_3, 34%, VWR), and glucose ($C_6H_{12}O_6$, VWR). Lower surface energy was obtained using (heptadecafluoro-1,1,2,2-tetrahydrodecyl) trimethoxysilane ($CF_3(CF_2)_7CH_2CH_2Si(OCH_3)_3$, denoted as FAS (ABCR GmbH & Co. KG, Karlsruhe, Germany). A mixture of 1 ml FAS and 50 ml ethanol (C_2H_5OH, 99.5 %, Altia Oyj Finland) was used for the low surface energy coating. Zinc oxide thin films were produced with the following precursors: 2-methoxyethanol ($CH_3OCH_2CH_2OH$, Sigma-Aldrich), ethanolamine ($NH_2CH_2CH_2OH$, Sigma-Aldrich), zinc acetate dehydrate (Sigma-Aldrich, $C_4H_6O_4Zn{\cdot}2H_2O$), hexamethylenetetramine (HMTA, $C_6H_{12}N$, Sigma-Aldrich), and zinc nitrate hexahydrate ($Zn(NO_3)_2{\cdot}6H_2O$, Sigma-Aldrich). For the copper doping of ZnO thin films, copper nitrate trihydrate ($Cu(NO_3)_2{\cdot}3H_2O$, Sigma-Aldrich) was used.

4.2 Preparation of the samples

The sample preparation processes carried out in publications I–VI are described in this chapter. The synthesis routes and chemicals used in each step are noted in detail.

4.2.1 Fabrication of superhydrophobic silver-containing and superhydrophobic surfaces (Publication I and II)

Superhydrophobic surfaces were prepared using the following procedures. 3 g aluminum tri-sec-butoxide was mixed with 30 ml isopropyl alcohol and stirred at ambient conditions for 1 h. After that, 2 ml ethyl acetoacetate was added into the solution and it was stirred

for 1 h. Then a mixture of 5 ml isopropyl alcohol and 1 ml de-ionized water was added for hydrolysis. Next, the solution was stirred for 2 h and then the AISI 304 type austenitic stainless steel plates were coated. Before coating, the substrates were rinsed with acetone and ultrasonicated in both ethanol and water. Finally the substrates were wiped with isopropyl alcohol. After cleaning the substrate, spin coating was carried out at 1500 rpm for 20 s. After 10 minutes drying in air, the specimens were heat treated at 400 ºC for 15 min. Next, the specimens were immersed in boiling water for 10 min and then dried in air. Finally, a heat treatment at 600 °C for 30 min to obtain a γ -alumina phase structure was performed.

Silver particles were reduced onto the surface using the Tollens process. First, 1% silver nitrate solution was prepared. Then, 1 ml sodium hydroxide was added so that silver oxide precipitation occurred. Then ammonia was added to form diammonium silver complex ions until the precipitate dissolved and the solution became clear. After that, 1 g glucose was dissolved into 10 ml de-ionized water and the solution was added to reduce the diammonium silver complex ions to metallic silver. The solution was then spin-coated on the previously prepared γ -alumina surface and finally a heat treatment was performed at 80 ºC for 15 min to ensure the silver reduction.

To obtain low surface energy, a layer of FAS was added on the surface. 1 ml FAS and 50 ml ethanol were mixed and stirred for 1 h at room temperature. Then the samples were immersed in the prepared solution for 1 h after which they were heat-treated at 180 ºC for another 1 h to ensure the condensation reaction between the surface and the FAS molecules.

4.2.2 Fabrication of ZnO films for antibacterial and photocatalytic studies (Publication III)

Zinc oxide thin films were prepared by a two-step hydrothermal method in order to study the antibacterial and photocatalytic properties of the films. The samples were prepared by changing the synthesis parameters in order to obtain thin films with varying morphology. The synthesis parameters that were altered were the precursor concentration and temperature. At first, the concentration of zinc nitrate hexahydrate and HMTA was 0.029 M and the temperature was 90 ºC. Then, the samples were prepared at zinc nitrate hexahydrate and HMTA concentrations of 0.058 M and a temperature of 80 ºC. Finally, a set of samples was prepared at zinc nitrate hexahydrate and HMTA concentrations of 0.16 M and a temperature of 90 ºC. The substrates were cleaned by wiping with isopropanol and rinsing with ethanol and before the hydrothermal growth of ZnO structures, a seed layer was formed on an AISI 304 stainless steel substrate (75mm x 25 mm). A solution for the seed layer was prepared by mixing 2-methoxyethanol ($CH_3OCH_2CH_2OH$)

and ethanolamine ($NH_2CH_2CH_2OH$) (96:4). Then 0.23 M zinc acetate dehydrate ($C_4H_6O_4Zn \cdot 2H_2O$) was dissolved into the mixture which was then stirred at 60 ºC for 2 h. The solution was cooled down and then spin-coated on the substrates. The samples were then heat-treated at 350 ºC for 20 min. The solution for the growth of a ZnO layer with nanotopography was prepared by mixing hexamethylenetetramine ($C_6H_{12}N$) and zinc nitrate ($Zn(NO_3)_2$) with a volume ratio of 1:1. The plates were placed in the solution with the seed layer side upside down and the growth was allowed to continue for 2 hours. After being removed from the solution, the samples were rinsed with de-ionized water and then dried in air. Finally, the samples were heattreated at 300 ºC for 30 min.

4.2.3 Fabrication of ZnO films for the study of the effect of temperature and concentration of precursors on morphology and photocatalytic activity of zinc oxide thin films (Publication IV)

The ZnO films were produced for publication IV using a similar method as in publication III. At first, a seed layer was formed on a stainless steel substrate followed by the growth of ZnO nanorods as described in section 4.2.2. In the hydrothermal growth of ZnO films, the concentrations of the mixtures of zinc nitrate hexahydrate and HMTA were 0.029 M, 0.058 M, and 0.16 M. Coatings were fabricated at three different temperatures: 70 ºC, 80 ºC, and 90 ºC. The hydrothermal growth was performed following the steps described in section 4.2.2.

4.2.4 Fabrication of ZnO films to study the effect of copper nitrate addition to precursor solution on topography, band gap energy, and photocatalytic activity (Publication V)

The samples were prepared for publication V using a similar two-step hydrothermal method to that used in publication III. In publication V, the zinc nitrate hexahydrate and HMTA concentrations were 0.05 M and the synthesis temperature was 90 ºC. A seed layer was formed on a steel substrate following the procedure described in section 4.2.2. Before the process, the substrates were cleaned by wiping with iso-propanol and rinsing with ethanol. A solution for the seed layer was prepared as described in section 4.2.2. Copper nitrate trihydrate ($Cu(NO_3)_2) \cdot 3H_2O$ was added to the growth solution in addition to HMTA and zinc nitrate hexahydrate. Two syntheses with varying copper concentrations were conducted: in the first synthesis, the Cu/Zn molar ratio in the solution was 0.005 and, in the second synthesis, the Cu/Zn molar ratio was 0.05. The hydrothermal growth procedure and final heat treatment were conducted as described in section 4.2.2.

4.2.5 Fabrication of ZnO films for investigation of long-term chemical stability of structured ZnO films in aqueous solutions of varying conditions (Publication VI)

For publication VI, the samples were prepared using the same method as in publication III. In publication VI, the zinc nitrate hexahydrate and HMTA concentrations were 0.058 M and the synthesis temperature was 80 ºC. Again, a seed layer was formed on cleaned stainless steel substrates followed by the growth of ZnO nanorods as described in the section 4.2.2. A solution for the seed layer was prepared, spin-coating was conducted and heat treatment was performed as described in section 4.2.2.

4.3 Characterization methods

In this section, the characterization methods used in this thesis are presented. These characterization methods include Field Emission Scanning Electron Microscopy (FESEM), water contact angle measurement, electrochemical impedance spectroscopy, atomic absorption spectrophotometry, UV-vis spectrophotometry, X-ray diffraction, and methods used in the determination of antibacterial activity.

4.3.1 Field Emission Scanning Electron Microscopy (FESEM) and energy-dispersive X-ray spectroscopy

The morphology of the synthesized thin films and coatings were analyzed using a field emission scanning electron microscope (FESEM Zeiss Ultraplus) at an acceleration voltage of 15 kV. Energy dispersive X-ray spectroscopy (EDS Inca Energy 350) was used to investigate the composition of the thin films and coatings.

4.3.2 Water contact angle measurements

To investigate the superhydrophobic nature of the films and to study the chemical changes on both the superhydrophobic coatings and ZnO thin films, water contact angles were measured using a KSV CAM 200 Optical tensiometer. A droplet of 10 µl was injected onto the surface, imaged, and measured with the tensiometer.

4.3.3 Electrochemical studies

The photoelectrochemical properties of the coatings were characterized using alternating-current electrochemical impedance spectroscopy (EIS). The open circuit potential (OPC) was recorded for 1 h before the EIS measurement. A classical three-electrode

cell was used with the measured specimen as a working electrode, an Ag/AgCl (3.0 M KCl) reference electrode, and a Pt counter electrode. A potentiostat (Gamry Instruments G750) was also used. An alternating voltage of 10 mV at a frequency range of 5–100 MHz was applied and the recorded data was analyzed with Gamry Echem Analyst 5.5 software.

4.3.4 Atomic Absorption Spectrophotometry

An atomic absorption spectrophotometer (AAS Philips PU 9200X) was used to investigate the dissolution of silver from silver-containing superhydrophobic surfaces as well as the dissolution of zinc from ZnO thin films. In the experiments, an air-acetylene flame was used to atomize the samples.

4.3.5 UV-vis spectrophotometry

Photocatalytic activity and band gap measurements were conducted using a UV-vis spectrophotometer. The photocatalytic activities of the prepared samples were measured in an aqueous solution of methylene blue. The samples were placed in a methylene blue solution in an open beaker and kept in the dark for one hour in order to reach the adsorption equilibrium. After that, an ultraviolet (UV) lamp (Ledia NIS330U-M UV-gun, peak maximum at 365±5 nm) located 10 cm above the MB solution was switched on. During the photocatalytic reaction, the absorbance of MB in the solution was measured at hourly intervals using a Shimazu UV-3600 UV/Vis/NIR spectrophotometer in a wavelength range of 300–800 nm. Band gaps were determined from the reflectance spectra obtained with CARY 300 UV-VIS Varian equipment by plotting $(Abs \times E)^{1/2}$ versus E (eV) and determining the band gap energy from the tangent.

4.3.6 X-Ray Diffraction (XRD) measurements

The XRD analyses were performed to analyze the crystal structure of the ZnO films. A Panalytical Empyrean Multipurpose Diffractometer was used at 2θ from 20° to 80° using CuKα radiation. The obtained data was analyzed using HighScore plus software.

4.3.7 Determination of antibacterial activity of the surfaces

In publications I and II, the antibacterial activity of the films was determined using the plate count method. The cleaned specimens were mounted on Petri dishes and immersed in a broth (Difco malt extract 0.6 g l^{-1}, Bacto yeast extract 0.02 g l^{-1}, saccharose 0.6 g l^{-1}) that was seeded with three bacterial strains: *pseudomonas rhodesiae*, *serratia marcescens,* and *lactobacillus paracasei*. The specimens were then covered by a lid and incubated under shaking for 18 h at 25 ºC. To remove the non-adhered bacteria, the

specimens were rinsed with sterile municipal tap water and the non-coated side of the specimens was rinsed with 70% ethanol. After that, the specimens were put in tubes (50 ml) with 45 ml of Ringer's solution. Ultrasonication (Bransonic 2210E-DTH, 47 kHz, 70 W) for 10 min and vortexing for 1 min were used to detach the adhered bacteria. Cultivation in Wallerstein Laboratory medium was performed during three days at 30 ºC for the first two days aerobically and one day anaerobically. The results are given in colony-forming units (CFU cm^{-2}).

In publication III, the antibacterial activity of the ZnO films was determined using *S. aureus* 8325-4 containing plasmid pAT19-lux-hlaP-frp and *E. coli* K-12 MG1655 (DSM 18039) containing plasmid pCGLS1 as constitutively bioluminescent biosensor cells. An IVIS® Lumina imaging station (Caliper Life Sciences, USA) was used for measuring the bioluminescence of the specimens. Exposure times were 2 min and 10 min for *E. coli* and *S. aureus*, respectively. To analyze the bioluminescent results, the counts per area of the sample disc and the background surrounding area were calculated and the sample disc counts were divided by the background surrounding area counts to obtain the relative antibacterial activities of the specimens.

5 RESULTS AND DISCUSSION

The main results introduced in publications I–VI are presented in this chapter. The aim of the work was to develop easy-to-clean materials that inhibit bacterial growth, which could be exploited for instance in industrial environments to minimize the use of chemicals and time-consuming washing processes. At first, we prepared aluminum oxide based superhydrophobic silver-containing coatings using sol–gel processing and investigated the antibacterial property of the coating. The chemical durability of the coating was also studied [I]. The chemical stability of the coatings was then further investigated with more rigorous tests. [II] After that, we expanded the study by examining the photocatalytic properties of structured zinc oxide films in order to investigate the possibility of improving the durability of self-cleaning surfaces compared to that of superhydrophobic coatings. The impact of the surface structure on photocatalytic activity was also investigated. [III,IV] The antibacterial activity of the structured zinc oxide films was studied in publication III using both gram-positive and gram-negative bacterial species [III]. In the fifth publication, the effect of copper doping on photocatalytic activity and the band gap energy of zinc oxide films was studied. [V] Subsequently, we studied the chemical durability of zinc oxide thin films in varying conditions. [VI]

5.1 Superhydrophobic surfaces

In publication I we studied the antibacterial activity of silver-containing superhydrophobic coatings. The dissolution of silver from the coating was studied in different environments with varying pH values (1–13) in order to investigate the role of silver dissolution in antibacterial performance. The water contact angle values of specimens immersed in different solutions were measured after eight weeks of exposure to the solution to monitor the durability of the coating in an aqueous environment. In publication II we continued the study with superhydrophobic silver-containing surfaces. The antibacterial property was studied for a superhydrophobic surface without silver also in order to determine the role of the superhydrophobic coating in the antibacterial action of the coatings. The durability of the superhydrophobic and superhydrophobic silver-containing coating was also investigated more comprehensively using SEM imaging, water contact angle measurements, and EIS measurements.

5.1.1 Morphology analysis of superhydrophobic silver-containing surfaces

The aluminum oxide based superhydrophobic surfaces were prepared by the sol–gel method, using spin coating as the coating method. As described above, superhydrophobicity was induced by the addition of an FAS layer onto the surface and the Tollens process was used to reduce the silver particles on the surface. The silver particles formed were spherical with a diameter in the range of 50–200 nm. The structure of the prepared surfaces, superhydrophobic without silver and superhydrophobic with silver, are presented in Figures 14 a and b, respectively. The arrows in Fig. 14 c indicate the silver particles on the surface.

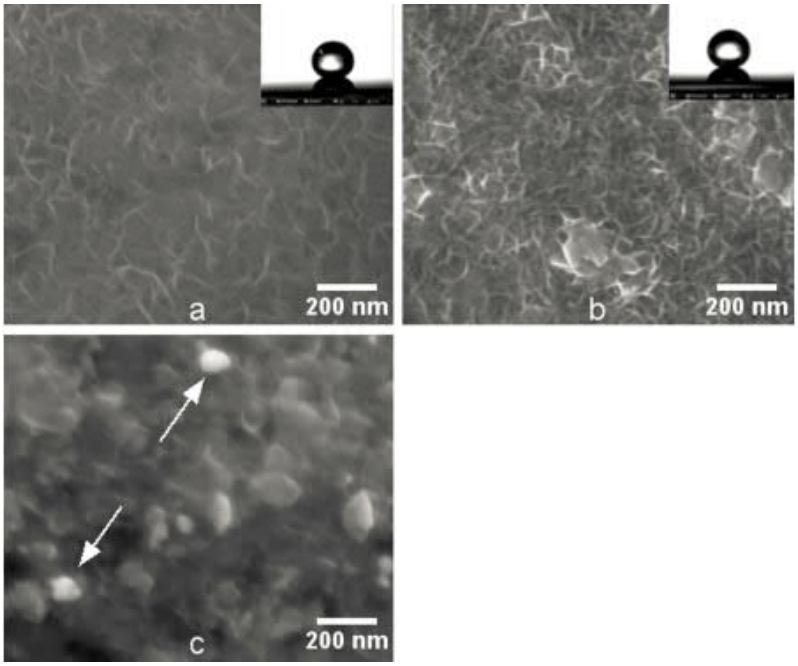

FIGURE 14 Superhydrophobic surface without (a) and with (b and c) silver particles. The water contact angles of the surfaces were measured from the water droplet shown in the upper right corner. (Publication II)

5.1.2 Antibacterial activity and silver dissolution from superhydrophobic silver-containing surfaces

Antibacterial activity was studied for a stainless steel substrate (reference), a superhydrophobic coating, and a superhydrophobic silver-containing coating. The number of viable cells on the superhydrophobic silver-containing surface was notably lower compared to the stainless steel (the superhydrophobic silver-containing coating reduced the number of viable bacteria by 88% compared to the stainless steel specimen, see Fig. 15). The superhydrophobic surface without silver, however, did not reduce the number of viable bacteria adhered on the surface in comparison with the stainless steel surface. This indicates that the antibacterial action of the superhydrophobic silver-containing surface is attributed to silver and the superhydrophobic nature of the film does not play a role in the decrease in the number of viable bacteria on the surface.

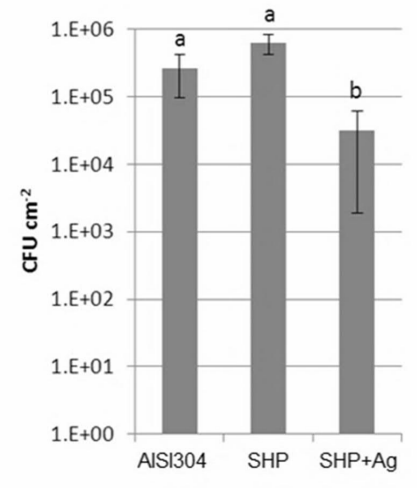

FIGURE 15 Antibacterial activity test results for stainless steels (AISI304), superhydrophobic (SHP) and superhydrophobic silver-containing (SHP+Ag) surfaces. (Publication II)

Silver cations play a predominant role in the antibacterial activity of silver and thus it was of particular interest to investigate the solubility of silver from the coatings. Seven pH values ranging from 1 to 13 were selected to investigate silver solubility in different environments. The dissolution test showed that within eight weeks, varying amounts of silver

dissolved from the superhydrophobic silver-containing coatings in the investigated solutions. Dissolution was highest at pH 1 (0.48 mg/l at 8 weeks) and second highest at pH 3 (0.23 mg/l at 8 weeks). At pH 13 the amount of dissolved silver was slightly less than at pH 3 (0.19 mg/l at 8 weeks). At pH 5 the amount of dissolved silver was 0.11 mg/l at eight weeks. The amounts of dissolved silver at pH 7, 9, and 11 were 0.02, 0.04, and 0.01 mg/l, respectively (Fig. 16).

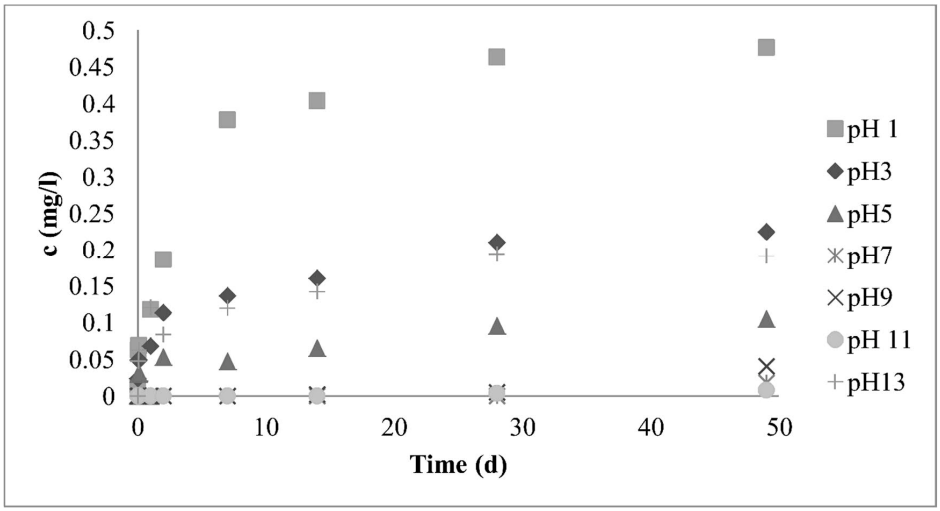

FIGURE 16 Concentration of dissolved silver in solutions with pH varying in the range of 1–13. (Publication II)

It can be concluded that superhydrophobic silver-containing surfaces possessed notable antibacterial activity compared to that of the reference stainless steel surface. The antibacterial activity can be attributed mainly to the silver particles. The amount of dissolved silver is highest at low pH (pH 1) and decreases as the pH increases. At a high pH level (pH 13), silver dissolution is comparable to that of pH 5 but at pH values in the range of 7–11 the amount of dissolved silver is significantly lower compared to that of pH < 7 and pH 13. However, silver was dissolved at least slightly in all the tested conditions (pH 1–13). Although the superhydrophobic property itself did not induce antibacterial activity, it can be beneficial in the removal of killed bacteria from the surface.

5.1.3 Chemical resistance of superhydrophobic surfaces

The chemical resistance of superhydrophobic surfaces was investigated by monitoring the water contact angles and by SEM imaging. The water contact angles of the prepared superhydrophobic and superhydrophobic silver-containing coatings were measured as

157 and 154 degrees, respectively. It was shown that the water contact angle decreases slightly even after a relatively short exposure to an aqueous solution (24 h). After one week of exposure to all the solutions used (pH 1–13), the surface was still notably hydrophobic. After five weeks of exposure, however, the water contact angle had significantly decreased at pH 1. At all the other pH values, the water contact angle was relatively high and the surface remained hydrophobic. After eight weeks of exposure, the water contact angles of the superhydrophobic silver-containing surface immersed in solutions with pH 1, 3, 5, 7, 9, 11, and 13 were 106 º, 123 º, 131 º, 142 º, 143 º, 145 º, and 98 º, respectively. This shows that the superhydrophobic nature of the surface had been preserved the most at pH 7, 9, and 11 and the durability of the superhydrophobic surface was lowest at pH 13 and pH 1, where the water contact angles had significantly decreased. A notable decrease in the water contact angle also appeared at pH 3 and 5, which indicates that some chemical or structural changes had occurred on the surface. The lowest and highest measured water contact angle values are listed in table 1 (marked in parentheses) after the average water contact angle value. It can be noted that the variation is relatively high, which indicates that the structure of the coating is not completely uniform throughout the whole surface. The higher the exposure time, the higher the variation is. This also suggests that the removal rate of the coating is not even at different spots on the surface.

TABLE 1 The average water contact angle values of the superhydrophobic silver-containing surfaces after eight weeks exposure to solutions with pH values varying in the range of 1–13 (the highest and the lowest measured values are marked in parentheses). S1 and S13 refer to a superhydrophobic surface without silver at pH 1 and 13, respectively. (Publication II)

pH	0 h	24 h	1 week	5 weeks	8 weeks
S1	**157**				**101**(92,115)
1	**154**	**149**(145,152)	**147**(144,151)	**106**(96,113)	**106**(102,114)
3	**154**	**137**(132,144)	**133**(123,141)	**131**(123,141)	**123**(115,145)
5	**154**	**138**(134,143)	**136**(133,140)	**130**(125,136)	**131**(121,138)
7	**154**	**140**(139,141)	**135**(133,136)	**139**(125,145)	**142**(134,150)
9	**154**	**145**(143,147)	**147**(139,156)	**136**(133,137)	**143**(141,144)
11	**154**	**145**(140,149)	**142**(136,146)	**127**(115,133)	**145**(135,149)
S13	**157**				**102**(95,113)
13	**154**	**145**(143,146)	**136**(133,140)	**130**(124,139)	**98**(74,112)

In addition to monitoring the water contact angle, SEM imaging was conducted to inspect changes on the surfaces during the exposure to the solutions. Fig. 17 shows the superhydrophobic silver-containing coating exposed to nitric acid solution of pH 1. It can be noted that, after 24 hours, the coating has been preserved relatively well. After one week of exposure, the coating was still covering the surface. The water contact angle measurements supported the finding that the coating had not undergone any distinct changes during the first week of exposure since the water contact angle was significantly high after one week. After five weeks' exposure, the coating had been removed and only some small particles remained on the stainless steel surface. After eight weeks of exposure, no visible changes could be seen compared to the sample imaged after five weeks' exposure. The particles that were detected after five weeks still existed on the surface.

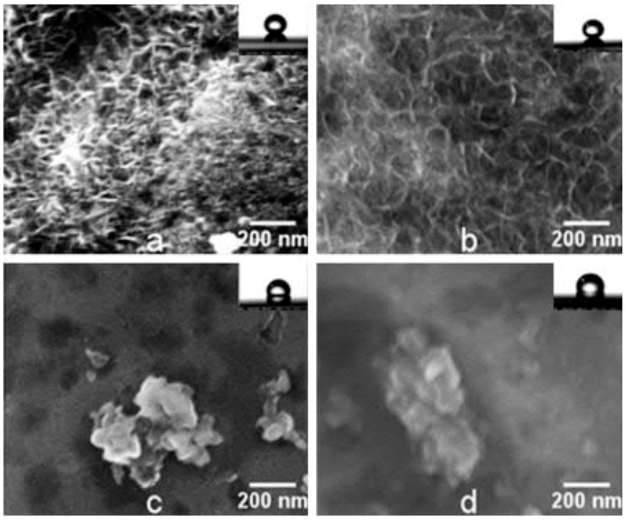

FIGURE 17 Superhydrophobic silver-containing surfaces exposed to nitric acid solution of pH 1 for a) 24 h, b) 1 week, c) 5 weeks, and d) 8 weeks. (Publication II)

At pH 7, no clear changes on the surface could be seen by SEM imaging during the first five weeks of exposure to the solution. After eight weeks' exposure, however, the structure had clearly partly dissolved and signs of corrosion could be detected under the thin coating layer (Fig. 18). Similar behavior was detected with the sample immersed in a solution of pH 13 after only one week of exposure. Although it was evident that changes had occurred on the surface at pH 13, a relatively homogeneous layer of the coating still remained on the surface after eight weeks, as shown in Fig. 19. Fig. 20 presents FESEM images of the samples exposed to pH 1, 3, 5, 7, 9, 11, and 13 after eight weeks of exposure. As can be seen, a flaky structure remained on the surface at all other pH

values except pH 1. At pH 13, the water contact angle was 98 º after eight weeks of exposure; that is to say, the water contact angle was close to that of the stainless steel specimen. It is obvious that the FAS layer had been removed in the solution of pH 13 during the eight-week period. At pH 3 and 5, no clear changes in the surface were visible after eight weeks' exposure (Fig. 20 b and c). In contrast, the water contact angle was relatively high after eight weeks' exposure at pH 7, 9, and 11. In addition, at these pH values (7, 9, and 11), the surface had not undergone any visible changes during the eight-week exposure (Fig. 20 e and f). However, at pH 3 and 5, the water contact angles had clearly decreased to 123 º and 131 º, respectively. It can be postulated that the FAS layer was not damaged on the surface in neutral and slightly basic conditions. In slightly acidic conditions, the FAS layer was partly removed or modified leading to a decrease in the water contact angle. It is also worth noting that the FAS layer is not strongly bound on top of the silver particles, enabling dissolution of silver from the particles. Once the silver has completely dissolved, the holes on the sites previously occupied by silver particles allow penetration of water into the structure. This might lead to the decomposition of the coating.

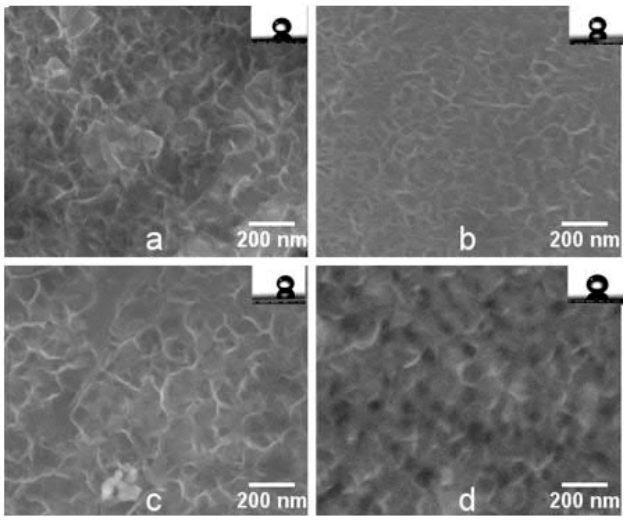

FIGURE 18 Superhydrophobic silver-containing surfaces exposed to a solution of pH 7 for a) 24 h, b) 1 week, c) 5 weeks, and d) 8 weeks. (Publication II)

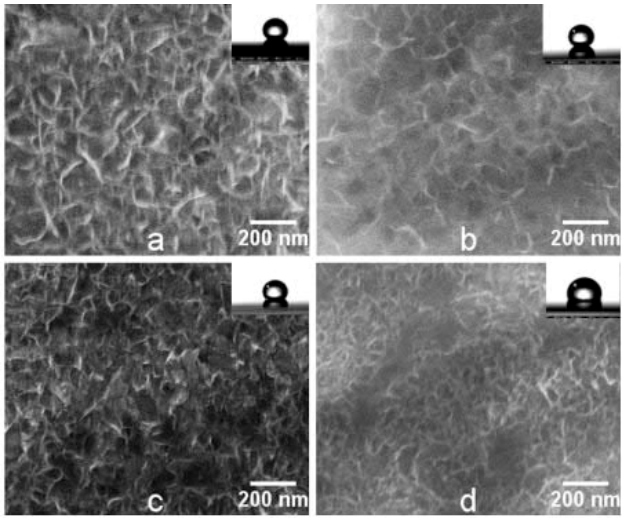

FIGURE 19 Superhydrophobic silver-containing surfaces exposed to an ammonia solution of pH 13 for a) 24 h, b) 1 week, c) 5 weeks, and d) 8 weeks. (Publication II)

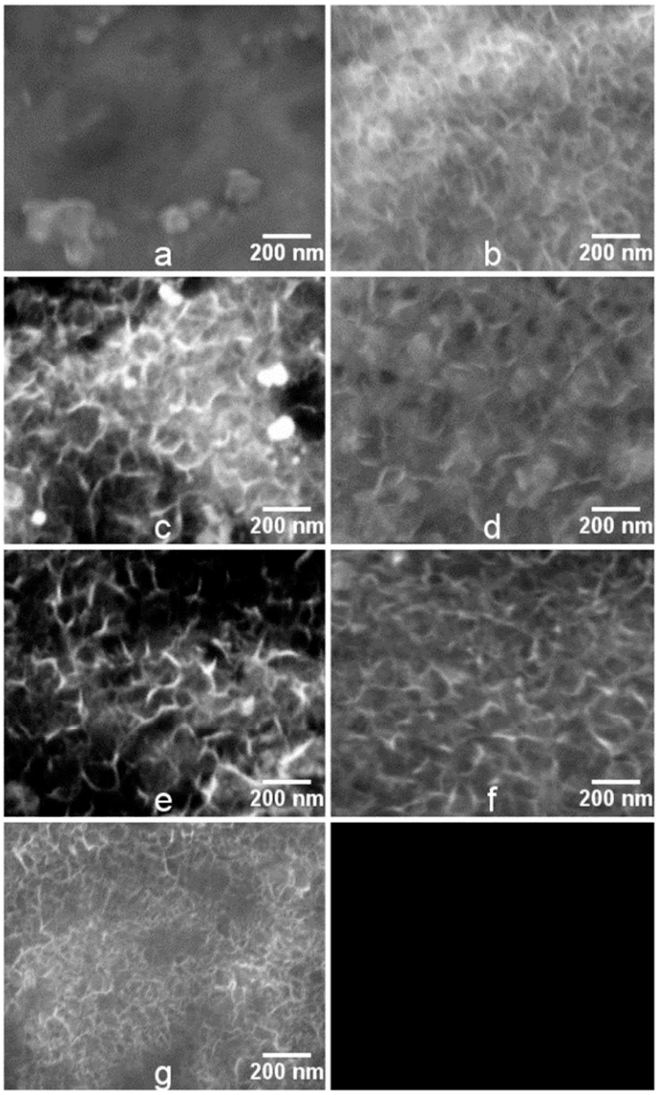

FIGURE 20 FESEM images of superhydrophobic silver-containing coatings after eight weeks of exposure to solutions of pH a) 1, b) 3, c) 5, d) 7, e) 9, f) 11, and g) 13. (Publication II)

As another means to study the chemical resistance of the coatings, the possibility of EIS measurements to determine the presence of silver and different layers (alumina, FAS) on the surface was also investigated. The investigated samples were a stainless steel plate, stainless steel coated with FAS, stainless steel coated with alumina, stainless steel

coated with both alumina and FAS, stainless steel coated with alumina and silver particles, and stainless steel coated with alumina, silver particles and FAS, i.e., the superhydrophobic silver-containing coating. The spectra obtained in the EIS measurement are shown in Fig. 21. These spectra demonstrate that different coating layers imparted a different electrochemical behavior to the surface. The superhydrophobic surface without silver possessed the highest impedance values. The addition of silver onto the superhydrophobic surface decreased impedance value although the impedance value was still notably higher than with any of the other tested surfaces. Thus, it can be anticipated that dissolution of the alumina layer as well as removal of the FAS layer could be detected from the decrease in the impedance value. Moreover, the dissolution of silver could lead to an increase in the impedance. Two samples, one exposed to pH 3 for eight weeks and one exposed to pH 11 for five weeks were investigated and the EIS spectra were determined for these samples. From the obtained spectra (Fig. 22), it could be observed that the sample exposed to pH 11 for five weeks had a higher impedance value than the unexposed superhydrophobic silver-containing sample, indicating dissolution of silver from the surface. In contrast, the sample exposed to pH 11 for five weeks had lower values than the one exposed to pH 3 for eight weeks, which indicates that there is more silver present on the surface in the sample exposed to pH 11. This is fully consistent with the AAS measurement results shown on page 34.

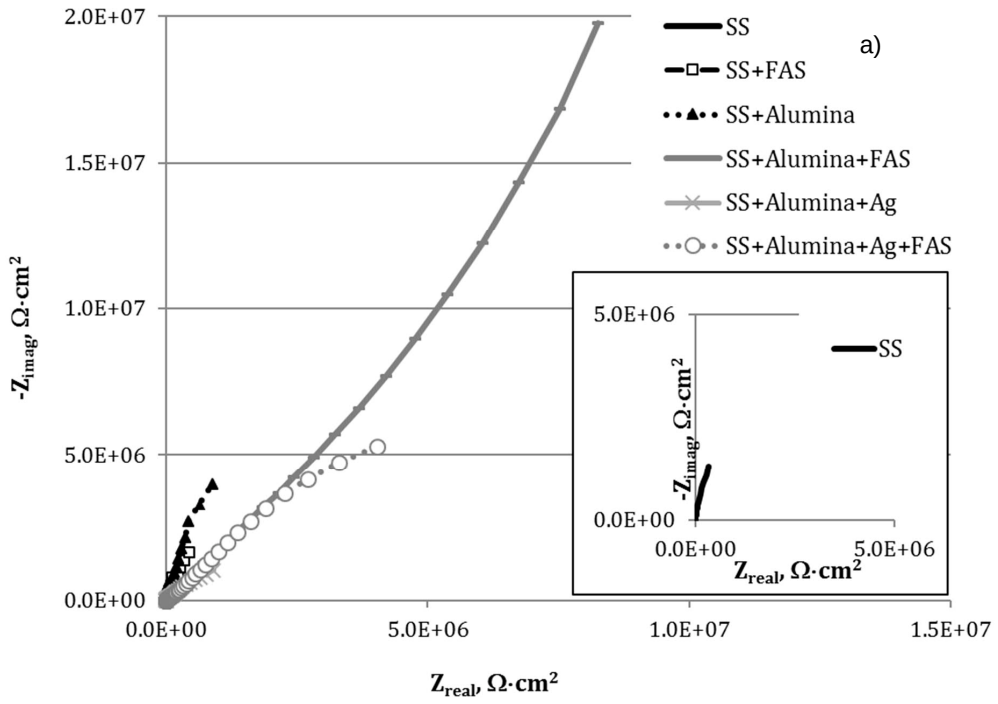

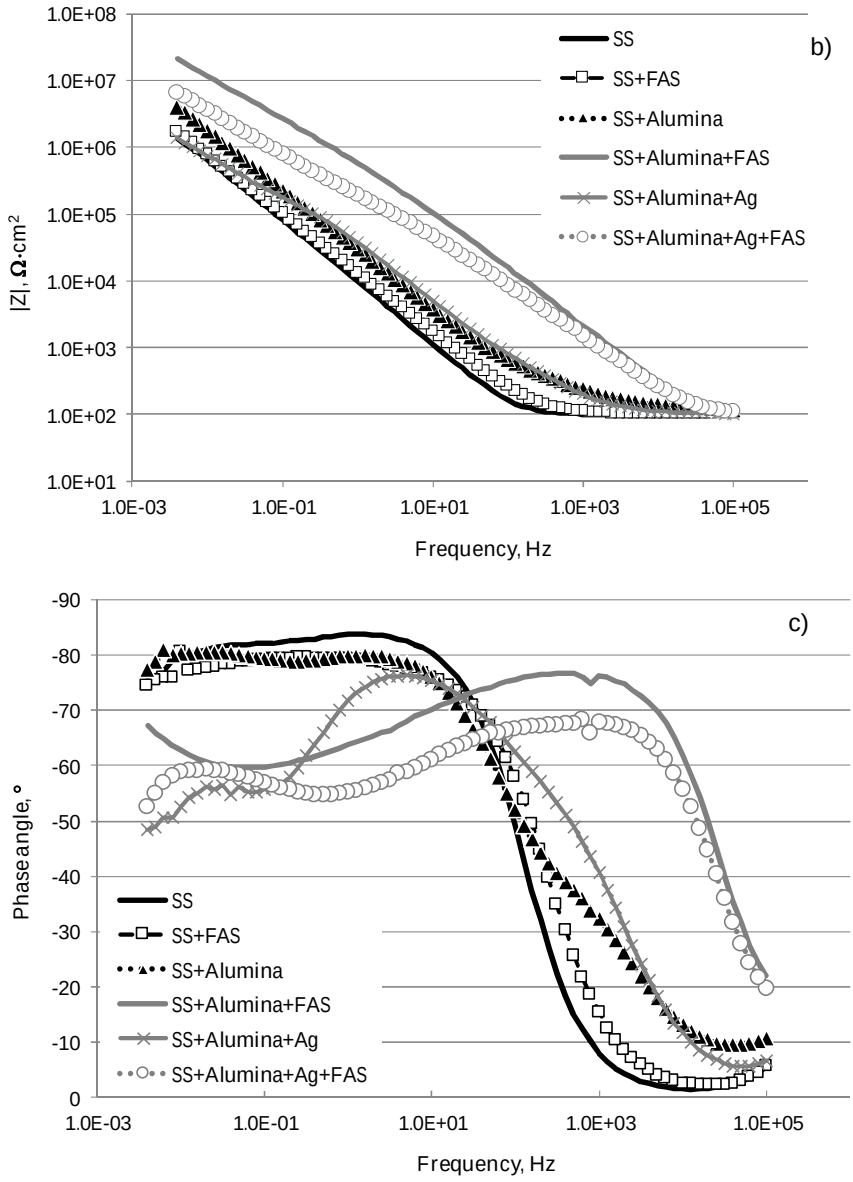

FIGURE 21 EIS spectra a) Nyquist plot, b) bode magnitude plot, and c) bode phase angle plot for stainless steel (SS), stainless steel coated with FAS (SS+FAS), stainless steel coated with alumina (SS+Alumina), stainless steel coated with alumina and silver (SS+Alumina+Ag), and superhydrophobic coating with and without silver (SS+Alumina+Ag+FAS and SS+Alumina+FAS, respectively). (Publication II)

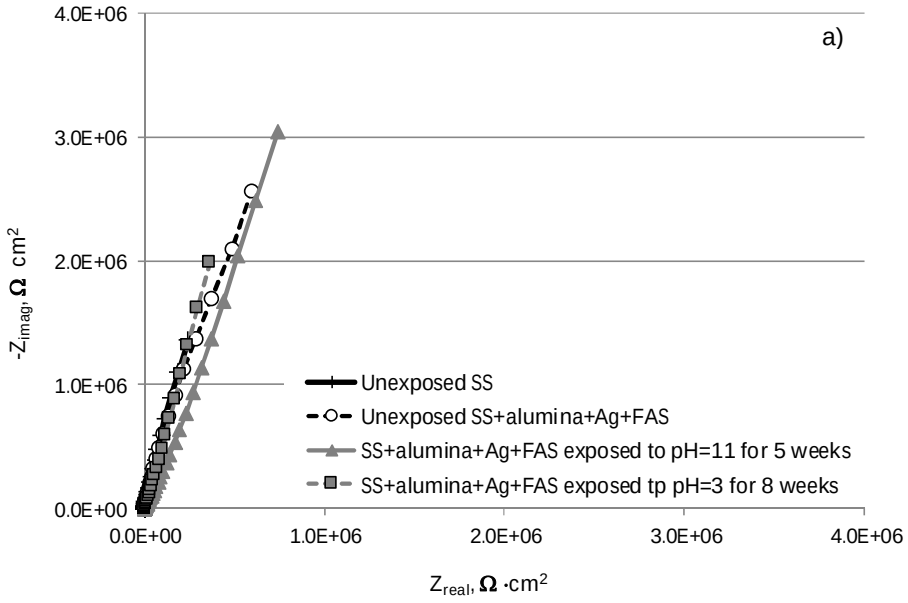
a)
4.0E+06
3.0E+06
2.0E+06
1.0E+06
0.0E+00
-Zimag, Ω cm2
0.0E+00
1.0E+06
2.0E+06
3.0E+06
4.0E+06
Zreal, Ω ·cm2
Unexposed SS
Unexposed SS+alumina+Ag+FAS
SS+alumina+Ag+FAS exposed to pH=11 for 5 weeks
SS+alumina+Ag+FAS exposed tp pH=3 for 8 weeks

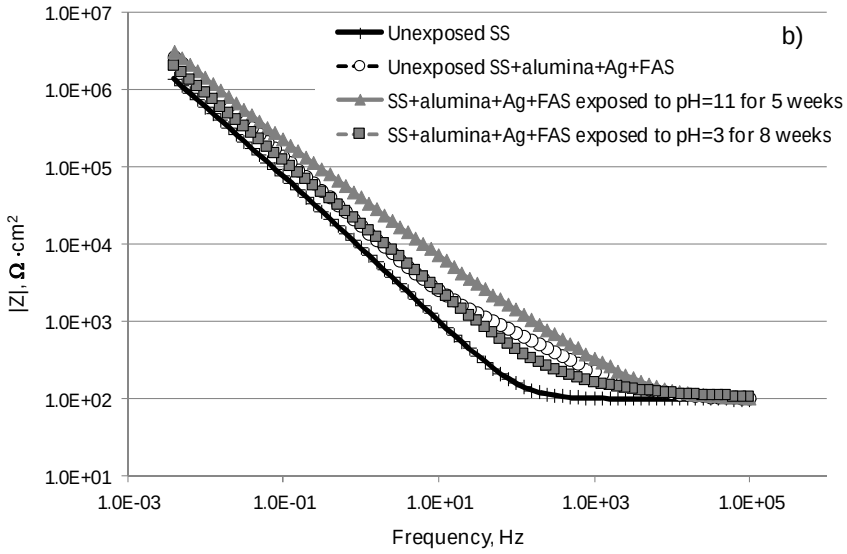
b)
1.0E+07
1.0E+06
1.0E+05
1.0E+04
1.0E+03
1.0E+02
1.0E+01
|Z|, Ω ·cm2
1.0E-03
1.0E-01
1.0E+01
1.0E+03
1.0E+05
Frequency, Hz
Unexposed SS
Unexposed SS+alumina+Ag+FAS
SS+alumina+Ag+FAS exposed to pH=11 for 5 weeks
SS+alumina+Ag+FAS exposed to pH=3 for 8 weeks

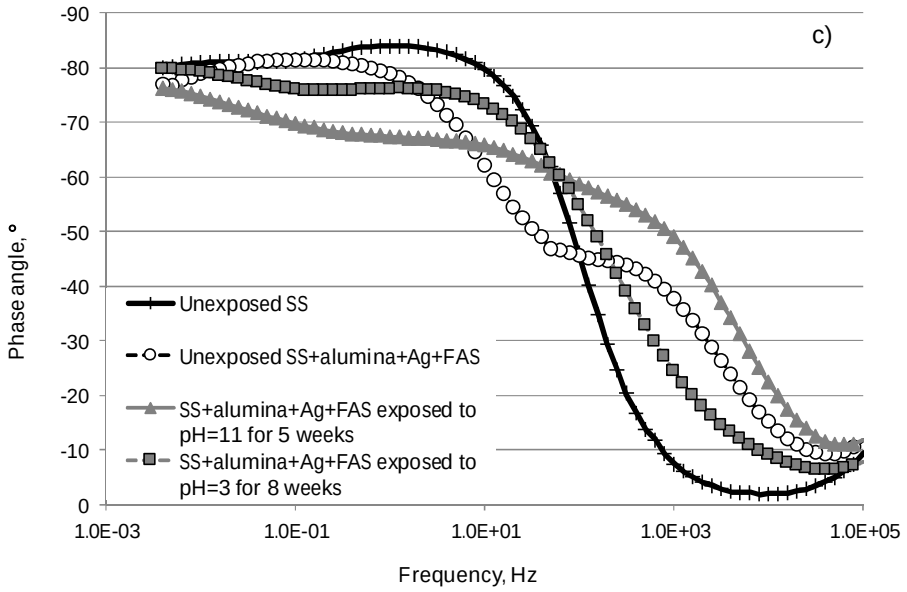

FIGURE 22 EIS spectra a) Nyquist plot, b) bode magnitude plot, and c) bode phase angle plot for superhydrophobic silver-containing coating, stainless steel surface, and superhydrophobic silver-containing samples exposed to pH 3 for eight weeks and pH 11 for five weeks. (Publication II)

In summary, the superhydrophobic silver-containing surfaces were successfully prepared and were found to exhibit notable antibacterial activity against the tested bacterial species. The combination of superhydrophobic and antibacterial properties was demonstrated to be a feasible option for antibacterial easy-to clean surfaces. The durability of the surfaces in aqueous solutions was investigated and it was found that while the surfaces did not last long in severe conditions, they preserved their properties relatively well in milder conditions.

5.2 ZnO films

In publication III, we produced ZnO thin films with different surface morphologies in order to study the effect of morphology on photocatalytic and antibacterial activity. The synthesis temperature and precursor concentration were altered, with the aim of producing surfaces with different surface structures. In publication IV, the photocatalytic properties of zinc oxide films with different morphologies were studied more thoroughly. In addition,

the effect of the concentration of the precursors on the morphology was investigated. In publication V, we continued studying ZnO films and tested the effect of copper addition on the topography, band gap energy, and photocatalytic activity of the films. In publication VI, we studied the long-term chemical stability of structured ZnO films in aqueous solution with varying pH values (3–11).

5.2.1 Investigation of influence of synthesis parameters on morphology of ZnO films

ZnO films were prepared using the hydrothermal method, varying the process temperature (70–90ºC) and precursor concentrations. The films prepared with three different precursor concentrations, 0.029 M, 0.058 M, and 0.16 M, denoted as C1, C2, and C3, respectively, at three different temperatures (70, 80, and 90 ºC), are shown in Figs. 23–25. It was found that the precursor concentration had a significant impact on the morphology of the ZnO film. At the lowest precursor concentration and lowest temperature (C1, 70 ºC), the substrate was partly covered with plain thin circular ZnO structures. It can be assumed that the temperature was not high enough for the nucleation to occur thoroughly on the surfaces and to induce the growth of longer ZnO needles as occurred at the same concentration at 80 ºC, where the whole substrate was covered relatively homogenously by thin ZnO needles. As the temperature further increased to 90 ºC with the concentration remaining the same, the size of the needles increased, and the orientation of the needles became less aligned. In addition, some significantly larger rods appeared on the surfaces. However, the amount of the larger rods was not high enough to have a notable impact on the surface area of the film. At the second highest concentration, C2, however, the growth of flaky hexagonal ZnO structures was detected. As the temperature increased to 80 ºC at concentration C2, the structure consisted of hexagonal rods, which indicates that (as at the lower precursor concentration), the lowest temperature was not high enough to induce the growth of longer rods. However, in contrast to the lowest concentration, at concentration C2 at 70 ºC, the substrate was completely covered by a thin layer of hexagonally shaped ZnO flakes. At the same concentration (C2) at 90 ºC, hexagonal rods were also detected. However, the rods were clearly less aligned compared to those synthesized at 80 ºC. At the highest concentration, C3, when the temperature was 70 ºC, the surface was covered by randomly grown ZnO structures that resembled the edges of hexagonal flakes. At C3 at 80 ºC, the ZnO structures that covered the surface were slightly smaller compared to those grown at the lower temperature. With the highest concentration (C3) at 90 ºC, the structures on the surface were clearly more flake-like compared to those grown at lower temperatures. As can be noted, in addition to the precursor concentration, the synthesis temperature also played an important role in the ZnO film growth. At the low precursor concentration, the temperature

needed to be higher for nucleation to occur and for the structures to grow along the c-axis. As the temperature further increased, the structures grew less aligned compared to the rather well aligned structures obtained at lower temperatures.

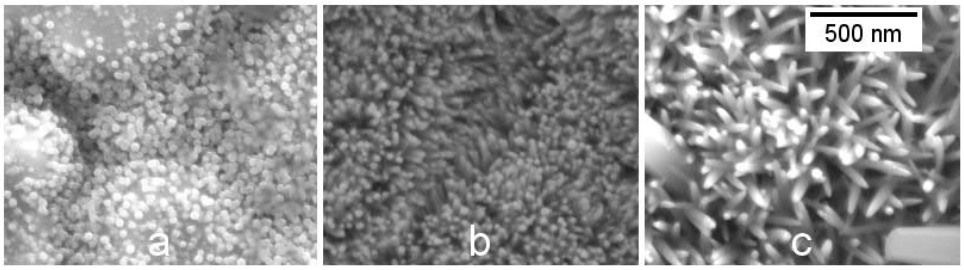

FIGURE 23 ZnO films synthesized at the lowest precursor concentration at a) 70 ºC, b) 80 ºC, and c) 90 ºC. (Publication IV)

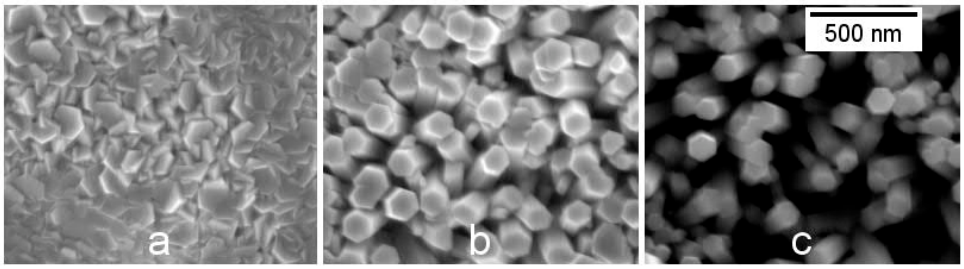

FIGURE 24 ZnO films synthesized at the second highest precursor concentration at a) 70 ºC, b) 80 ºC, and c) 90 ºC. (Publication IV)

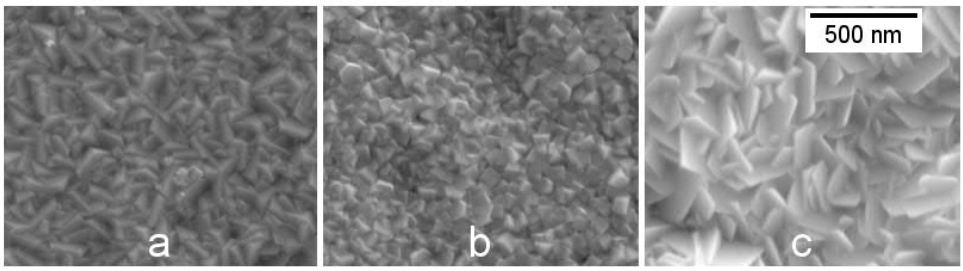

FIGURE 25 ZnO films synthesized at the highest precursor concentration at a) 70 ºC, b) 80 ºC, and c) 90 ºC. (Publication IV)

In addition to temperature and precursor concentration, the influence of the addition of copper nitrate to the precursor solution on the morphology, photocatalytic activity, and

band gap energy was investigated. It was found that the addition of copper nitrate resulted in a more aligned structure of ZnO needles (Fig 26). The diameter of the needles was also reduced slightly due to the addition of copper nitrate . However, the copper nitrate concentration was not found to play a significant role in the film morphology. Presumably, copper is reduced on the substrate. The properties of the substrate influence the nucleation process and the orientation of the needles growing on the substrate, as explained earlier on pages 11–12.

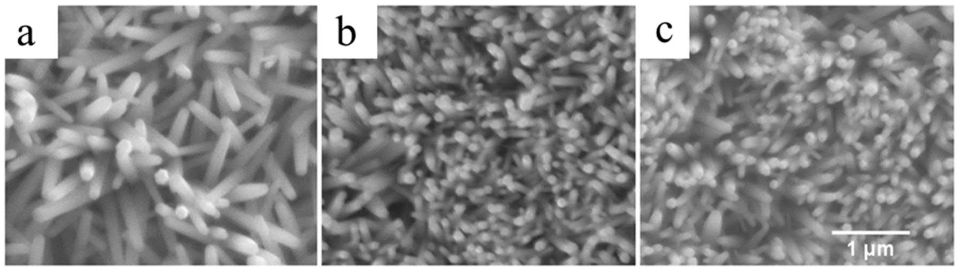

FIGURE 26 ZnO films synthesized a) without copper nitrate addition b) with 0.5% copper nitrate addition, and c) with 5 % copper nitrate addition to the precursor solution. (Publication V)

To conclude, the synthesis parameters, including temperature as well as precursor concentration and content, had a significant role in the formation of the ZnO surface structure. The lowest precursor concentration resulted in a needle-like structure. As the precursor concentration increased, thicker ZnO rods started forming on the surface. With a further increase in concentration, the surface structure was formed of thin flakes on the surface. The temperature was required to be at a certain level (>70ºC) in order for the above-described structures to grow. The addition of copper nitrate to the precursor solution promoted a more aligned, denser structure with thinner ZnO pillars.

5.2.2 **Photocatalytic activity of ZnO films**

The photocatalytic activity of the different ZnO films was measured in order to analyze the influence of the surface morphology on photocatalytic efficiency. The results are shown in Fig. 27. It was found that at the lowest and second lowest precursor concentration (C1 and C2, respectively), the films grown at the highest temperature (90 ºC) possessed the highest photocatalytic activity, followed by the films synthesized at 80 ºC. In contrast, at the highest precursor concentration (C3), the ZnO film synthesized at the lowest temperature showed the highest photocatalytic activity and those synthesized at the highest temperature (90 ºC) showed the lowest photocatalytic activity. Of all the

tested ZnO films, those synthesized with C2 at 90 ºC were the most active. The percentages of discolored methylene blue (MB) for the three most effective samples, the one synthesized with C2 at 90 ºC, the one synthesized with C1 at 90 ºC, and the one synthesized with C3 at 70 ºC were 91%, 82%, and 81.5%, respectively. Despite the differences between the samples, all the tested ZnO films showed relatively high photocatalytic activity. The differences observed between the samples resulted most probably from the differences in surface area. Moreover, the structures with less-aligned and less dense needle and rod structures exhibited greater photocatalytic activity compared to the denser, well-aligned structures. This could be due to the more effective penetration of water between the needles and rods and the fact that the radiation had access to the larger surface areas when the needles and rods were partly transverse in relation to the radiation.

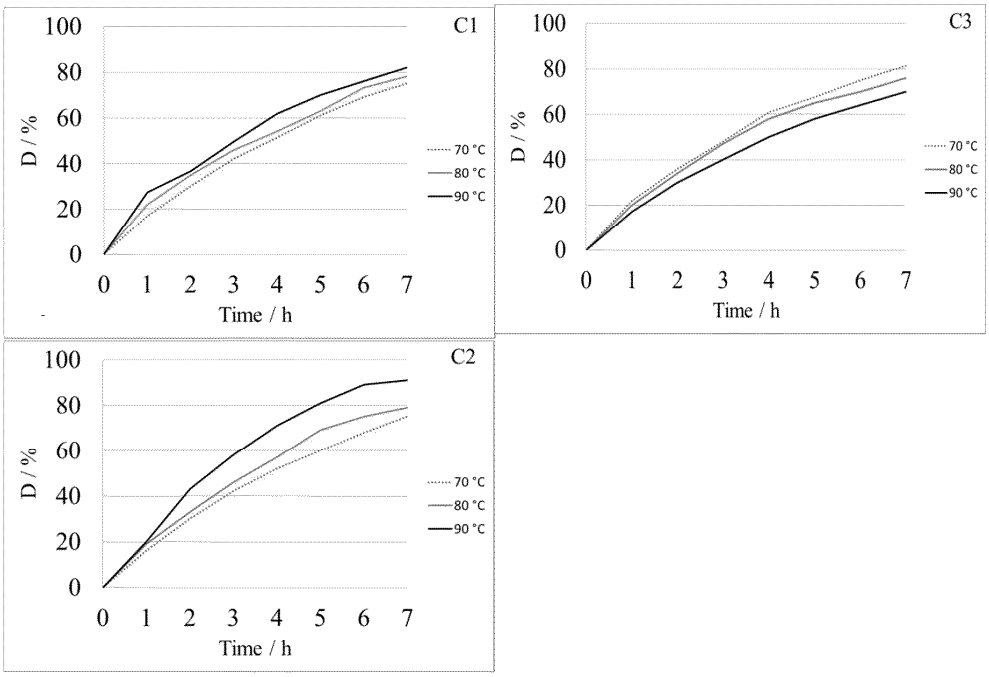

FIGURE 27 Photocatalytic activities of the nine ZnO films synthesized for the photocatalytic test (the lowest concentration C1 at 70, 80 and 90 ºC, second highest concentration C2 at 70, 80 and 90 ºC and the highest concentration C3 at 70, 80 and 90 ºC). (Publication IV)

In addition to the MB discoloration test, the photocatalytic activity of the films was also tested by measuring the water contact angles of the films under illumination. The results were in line with the MB discoloration test. The water contact angle decreased on all the

samples during the 30-minute period. Samples C1 and C2 at 90 ºC, and C3 at 70 ºC showed the highest decrease rate (0 º, 0 º, and 8 º after only 20 min of irradiation, respectively) in the water contact angle, which indicated that these surfaces possessed the highest photocatalytic activity.

The photocatalytic activity of the ZnO films grown in the solution containing copper nitrate was also studied. MB discoloration was used to evaluate the photocatalytic efficiency of the films. It was found that the addition of copper nitrate to the precursor solution resulted in the slightly reduced photocatalytic activity of the ZnO film (Fig. 28). An increase in the copper nitrate concentration in the precursor solution further decreased the photocatalytic activity. The decrease in photocatalytic activity could be explained by the change in the morphology of the ZnO film, inducing changes in the surface area of the film. Introducing copper to the lattice may also have decreased the photocatalytic activity due to the transfer of electrons and holes into the CuO phase, leading to recombination reactions in the CuO. [184]

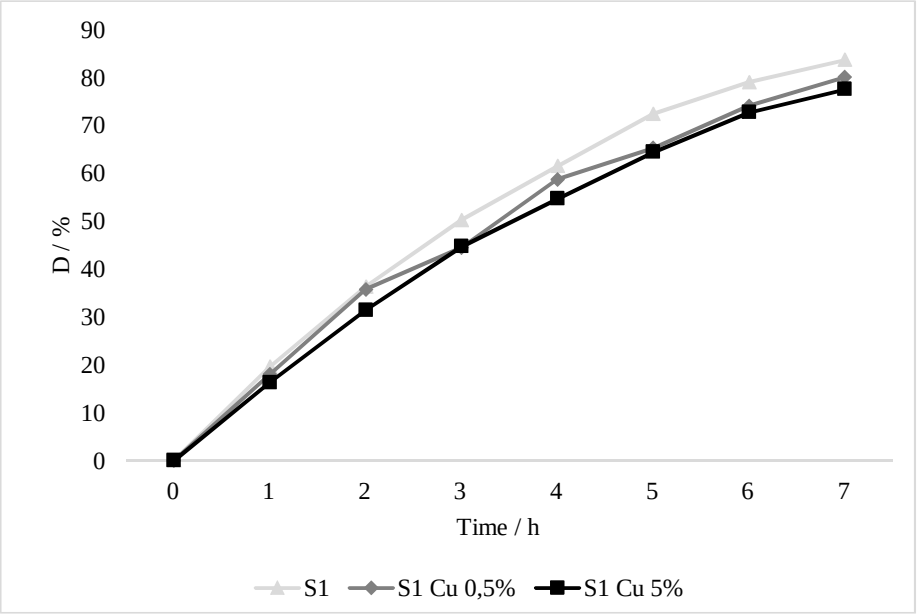

FIGURE 28 Photocatalytic activity of ZnO films synthesized without copper nitrate addition, with 0.5% copper nitrate addition, and with 5 % copper nitrate addition to the precursor solution. (Publication V)

In summary, the structure of the ZnO film was found to influence the photocatalytic activity of the surface. The less dense rod structure possessed the highest photocatalytic

activity. However, all the tested surfaces showed relatively high photocatalytic activity. The addition of copper nitrate to the precursor solution was found to decrease photocatalytic activity.

5.2.3 **Antibacterial activity of ZnO films**

The synthesis temperature and precursor concentration were altered with the aim of producing surfaces with notably different surface structures; needle-like structures (C1, 90º), hexagonal rods (C2, 80º), and a flaky structure (C3, 90º), as shown in Fig. 29. These films were used to investigate the influence of morphology on the antibacterial activity of the films. Dissolution of zinc from the surfaces was also studied since it is known that zinc ions contribute to the antibacterial activity of ZnO.

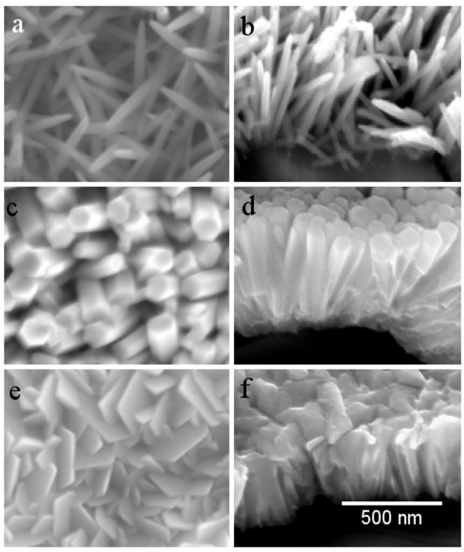

FIGURE 29 Top view (a,c,e) and cross-section (b,d,f) of ZnO films prepared using different synthesis parameters. The needle-like sample is denoted as C190º (a,b), hexagonal rods are denoted as C280º (c,d), and the flaky structure is denoted as C390º (e,f). (Publication III)

The AAS measurements showed that zinc had dissolved from all three coatings; the amount of dissolved silver being the highest from the needle-like surface. The lowest amount of dissolved zinc was detected from the flaky structured surface (Fig. 30). The amount of dissolved silver after seven hours of immersion in de-ionized water was 6.3 % higher for the needle-like surface (C190º) compared to the hexagonal rods (C280º) and 21.4 % higher compared to the flaky structure (C390º). Moreover, the dissolution from

C280º was equal to the dissolution from C390º during the first three hours, after which dissolution from C390º slowed down and from C280º increased. The differences in the amounts of dissolved zinc originate from the different surface areas of the coatings. The rod structure (C280º) is much denser compared to the needle-like structure, as can be seen from the cross-sectional images in Fig 29. It is obvious that water can penetrate deeper between the needles, which enables a higher zinc dissolution rate compared to the rod-like structure. The rod-like structure has a higher surface area compared to the flake-like sample and, once the water had penetrated between the rods (as a result of rod dissolution leading to a less dense structure), the dissolution rate of the rod-structured sample increased and the amount of dissolved zinc approached that of the needle-structured sample. The dissolution rate from the flake-like sample was relatively constant throughout the seven-hour test period.

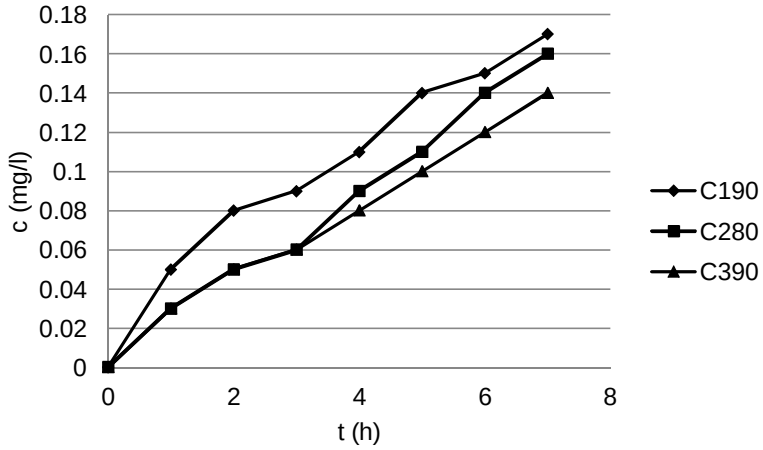

FIGURE 30 Concentration of dissolved zinc from the needle-like (C190º), rod-like (C280º), and flaky (C390º) samples in de-ionized water.

After the seven-hour immersion of the ZnO films in de-ionized water, they were imaged with FESEM in order to detect possible changes that might have occurred in the morphology during the dissolution test (Fig 31). Although no drastic changes in the morphology could be detected after exposure to the de-ionized water, the structure of the films was observed to be slightly less dense, especially in the case of the rod-structured film.

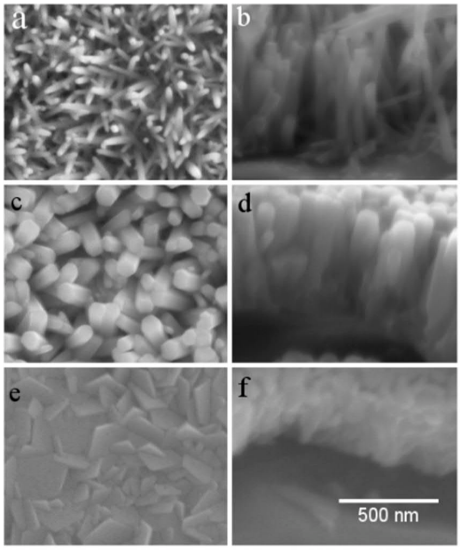

FIGURE 31 Top view (a,c,e) and cross-section (b,d,f) of ZnO films after seven hours' immersion in de-ionized water. Needle-like samples are denoted as C190º (a,b), hexagonal rods are denoted as C280º (c,d), and the flaky structure is denoted as C390º (e,f). The non-exposed surfaces are shown in Fig. 29. (Publication III)

In the antibacterial activity test, *E. coli* and *S. aureus* were used as bacterial strains to investigate and compare the antibacterial efficiency of ZnO films with different morphologies. Although it was shown that the dissolution of Zn from ZnO films was morphology-dependent, no changes in the antibacterial action could be detected with either of the bacterial strains. The results showed, however, that the antibacterial activity of the ZnO films was higher against *E. coli* than against *S. aureus* (Fig 32). Although it has been shown that the morphology of ZnO nanoparticles plays a role in their antibacterial efficiency, based on our results it can be stated that the antibacterial activity of ZnO does not have any clear correlation with the morphology of the structured film. Moreover, the antibacterial activity of the synthesized ZnO films was at the same level despite the morphology, even though it was shown that the dissolution of zinc was related to morphology changes. In the case of nanoparticles, the shape of the particle might affect the ability of the nanoparticle to penetrate a cell. In the case of the ZnO films, ZnO is bound to the surface and the antibacterial action is based solely on the contact between ZnO and the bacteria, the dissolution of Zn^{2+} cations, and the creation of ROS. Although surface structuring increases the surface area of the film, the size of the bacteria is not small enough that they could fit between the structures and thus the contact area between the bacteria and the surface is at the same level as on a smooth surface. A higher surface area can,

however, increase the amount of generated ROS.

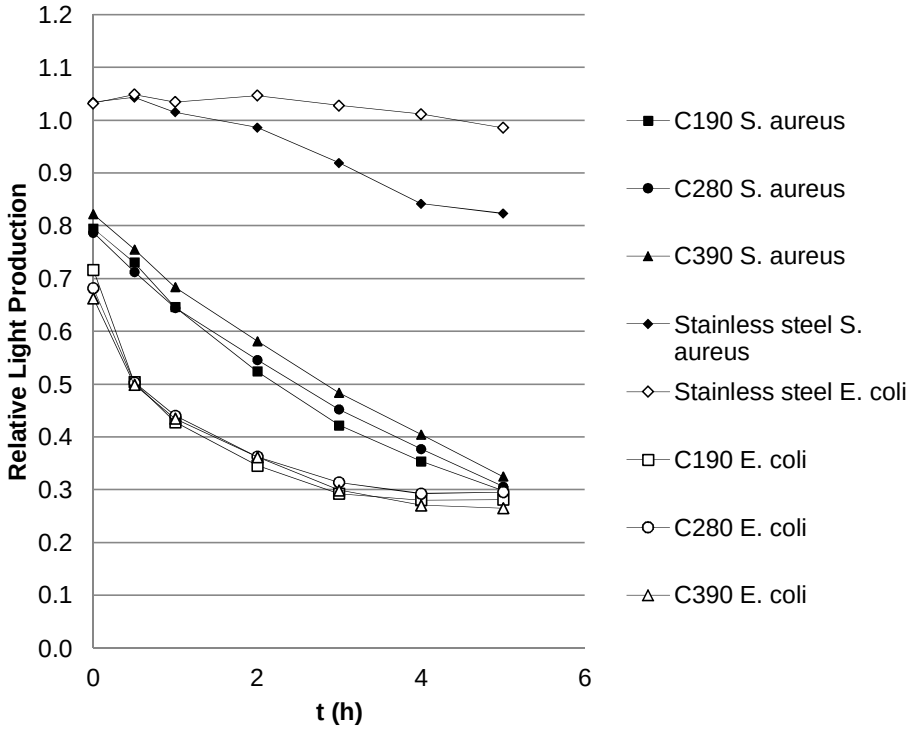

FIGURE 32 Relative light production of biosensor strain of *E. coli* (open symbols) and *S. aureus* (solid symbols) in the presence of AISI 304 stainless steel (diamonds) or ZnO samples C190º (squares), C280º (spheres), or C390º (triangles). The values were calculated by dividing the light production per area of the sample by the light production per area of cell suspension surrounding the sample. The results shown are averages from triplicate plates with error bars showing standard deviations.

To study the dissolution behavior of ZnO films in agar, the films were imaged with FESEM after 30 days of immersion in agar. Signs of corrosion could be seen clearly on all the specimens (C190º, C280º, and C390º, see Fig. 33). Despite the clear changes on the surfaces, the characteristic features of the morphologies could still be observed for all the specimens.

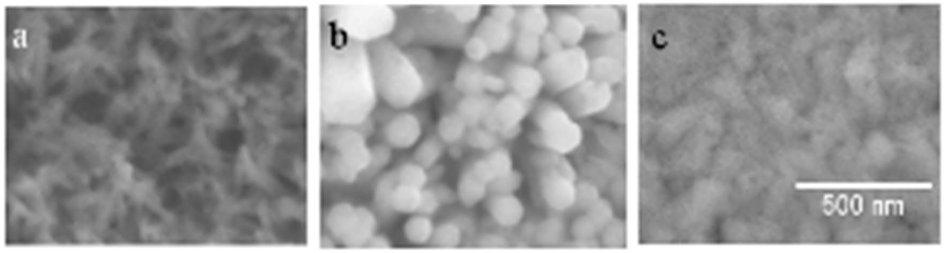

FIGURE 33 a) The needle-like (C190º), b) rod-like (C280º), and c) flake-like (C390º) ZnO films after 30 days immersion in agar. The non-exposed surfaces are shown in Fig. 29. (Publication III)

To sum up, the structured ZnO films exhibited relatively high antibacterial activity against *E. coli* and *S. aureus*. However, the morphology of the film was not found to affect the antibacterial activity of the surface. Zinc was found to dissolve from the surface and can be assumed to have contributed to the antibacterial activity of the film. The films were not visibly affected by the seven-hour immersion in water during the dissolution test but the 30-day immersion in agar clearly affected the surface.

5.2.4 **Effect of morphology and copper addition on band gap energy**

The band gap energies of the ZnO films with different morphologies were determined from the reflectance spectra measured with a UV-vis spectrophotometer. Band gap energies were determined for samples C190º, C280º, and C390º, shown in Fig. 29, and in addition, for the film that was found to be the most active in the photocatalytic measurement of all the prepared samples (concentration C2 synthesized at 90 º, denoted as C290º, Fig 24c). The needle-structured film (C190º) had a band gap energy of 3.145 eV, and the two rod-like structures (C280º and C290º) had band gap energies of 3.212 and 3.204 eV, respectively. The flaky ZnO film (C390º) had a band gap energy of 3.212 eV (Table 2). It is noteworthy that the structure with thin needles had the lowest band gap energy whereas the densest flake-like structure had the highest band gap value. Moreover, the less aligned rod structured specimen had a slightly lower band gap energy compared to the better-aligned rod structure.

The band gap energies for the ZnO films that were synthesized with an addition of copper nitrate hexahydrate to the precursor solution were also determined (Fig 26 b and c). The film that was synthesized in identical conditions except for the copper nitrate addition (Fig 25 a) had a band gap energy of 3.204 eV. The addition of 0.5% copper nitrate to the solution reduced the band gap energy of the film to 3.171 eV. When 5% of copper nitrate was added, the band gap energy further decreased to 3.163 eV (Table 2). It is notable

that the addition of copper nitrate to the precursor solution decreased the band gap energy of the synthesized ZnO film. The decrease in band gap energy can be attributed to a change in the morphology, arising possibly from morphology-induced native surface defects [185], but also from the copper atoms in the lattice, as earlier mentioned on page 18.

TABLE 2 Band gap energies for needle-like (C190º), rod-like (C280º and C290º), and flake-like (C390º) samples, and the literature value for the ZnO band gap energy.

Sample	*Band gap (eV)*
C190º	3.145
C280º	3.212
C290º	3.204
C390º	3.212
C290º+0.5%Cu	3.171
C290º+5%Cu	3.163
Literature value	3.37

As a conclusion, it can be noted that all the measured films had a lower band gap than that given in the literature. It is also significant that the thinner structures (needle-like structure of sample C190º and the samples with copper addition) had a lower band gap energy than the rod and flake-like structures.

5.2.5 Chemical resistance of ZnO films

The behavior of ZnO films in aqueous solutions with different pH values was investigated in order to evaluate the long-term usability of the films in different conditions. Nitric acid and ammonia were used to adjust the pH of the solutions. The films were prepared using two-step hydrothermal synthesis identically for all the ZnO films in this thesis. The synthesis temperature was 80 ºC and the concentration of the precursor solution was 0.058 M (denoted as C2). The structure imaged with FESEM at different magnifications from top view and cross-section is shown in Fig. 34. The film consisted of densely grown hexagonal rods. The height of the rods was approximately 1100 nm and the diameter of the rods was approximately 200 nm.

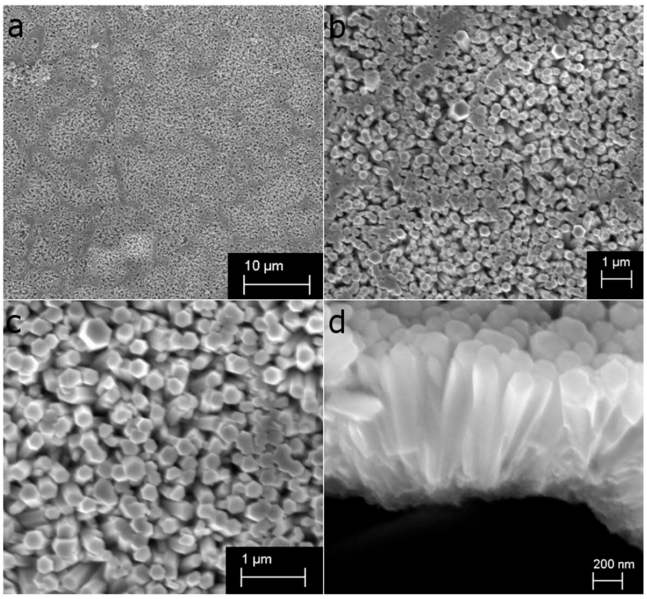

FIGURE 34 FESEM images at different magnifications of the ZnO film used in the chemical stability investigation. (Publication VI)

The dissolution of zinc from the surface was monitored using an atomic absorption spectrophotometer. The results show that the lower the pH value of the solution, the higher the amount of dissolved zinc (Fig 35). The highest zinc concentration was detected at pH 3, as can be predicted based on the Pourbaix diagram for the ZnO-H_2O system. It is notable that during the first six hours of immersion in the solutions, the differences in the amount of dissolved zinc at different pH values were already clear and, at pH 11, no zinc could be detected from the solution during that time period.

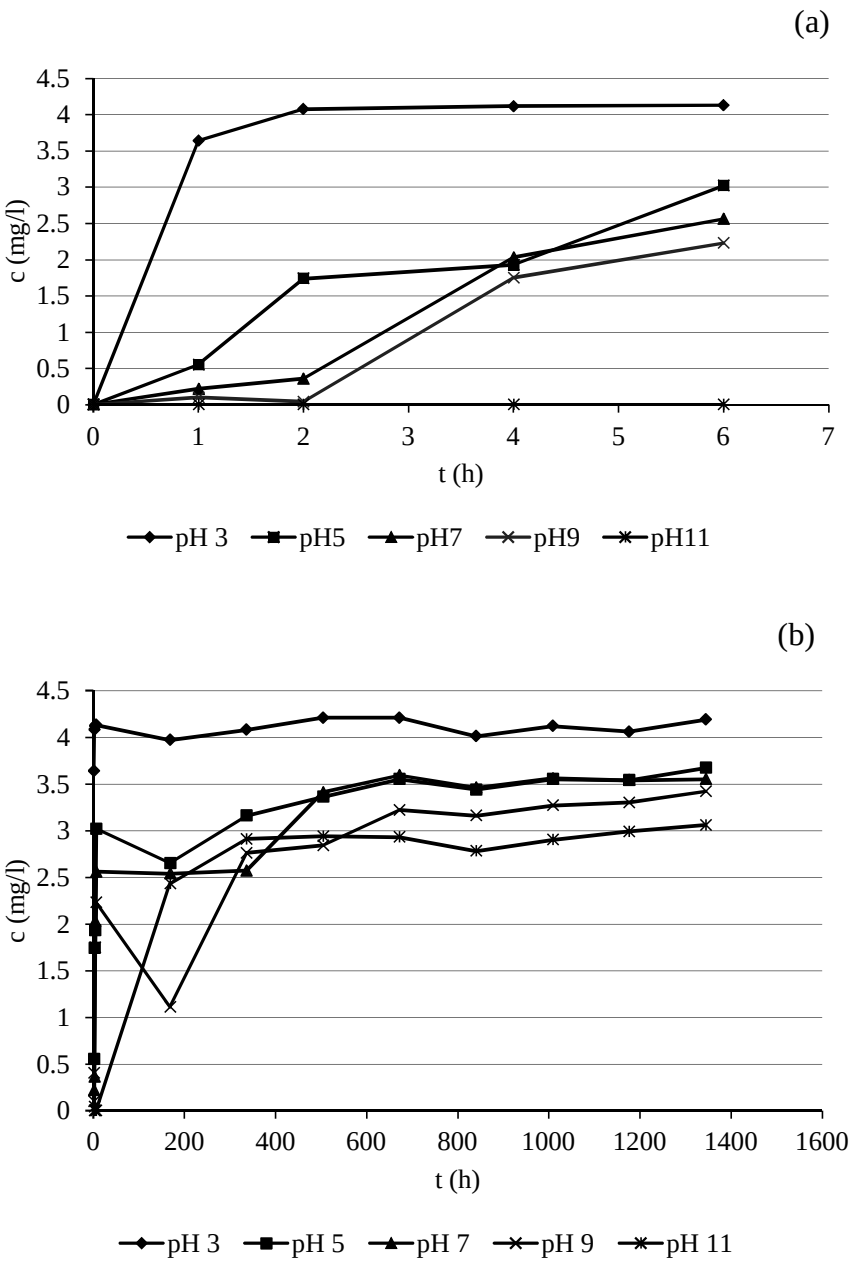

FIGURE 35 Concentration of dissolved zinc from the ZnO film in solutions with different pH values a) during a 6 h period and b) during a 1344 h period. (Publication VI)

In addition to the AAS measurements, the surfaces were imaged using FESEM at time points of 1, 2, 4, and 8 weeks to detect any changes on the surfaces during the immersion in aqueous solutions. At pH 3, the ZnO film had completely dissolved after only one week according to the FESEM image (Fig. 36 a). At pH 5, no clear change in surface topography could be detected by FESEM during the eight weeks of immersion (Fig 37 b). At pH 7, in contrast, flake-like structures could be detected on the surface after eight weeks' immersion (Fig. 38). The rod-like structure, however, did not show any clear changes during the eight weeks at pH 7, as can be seen in Fig. 39 b. At pH 9, the change in topography was not very clear during the eight weeks of immersion (Fig. 40 b). At pH 11, no change could be observed in the FESEM images during the eight weeks of immersion (Fig 41 b).

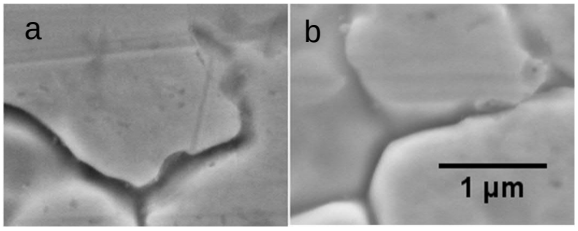

FIGURE 36 ZnO film exposed to nitric acid solution with pH 3 for a) 1 week and b) 8 weeks.

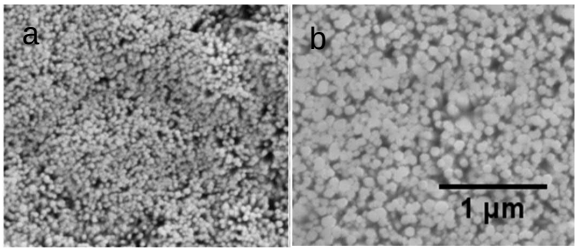

FIGURE 37 ZnO film exposed to nitric acid solution with pH 5 for a) 1 week and b) 8 weeks.

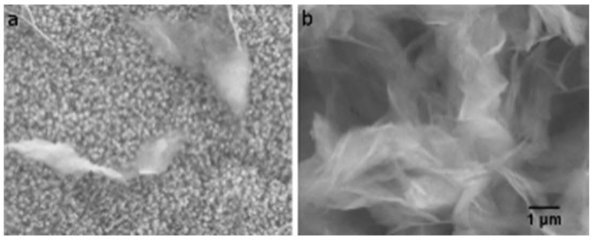

FIGURE 38 ZnO film exposed to ammonia solution with pH 7 for 8 weeks imaged at two different spots (a and b).

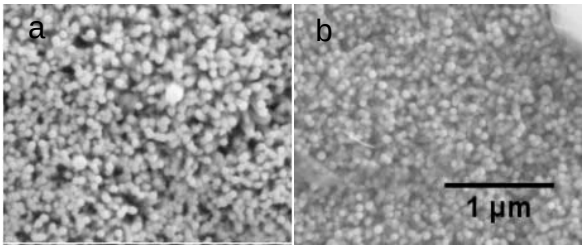

FIGURE 39 ZnO film exposed to ammonia solution with pH 7 for a) 1 week and b) 8 weeks.

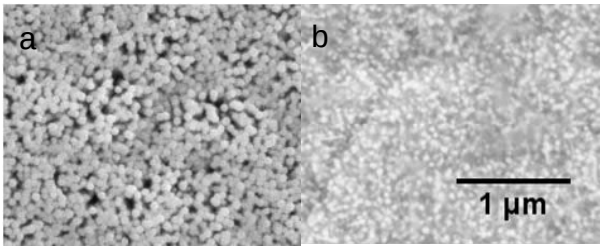

FIGURE 40 ZnO film exposed to ammonia solution with pH 9 for a) 1 week and b) 8 weeks.

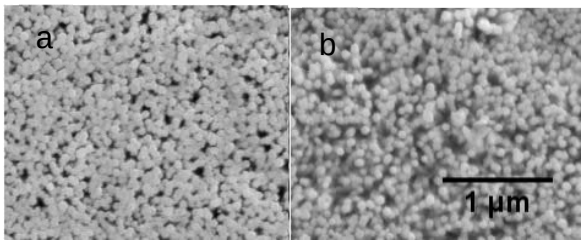

FIGURE 41 ZnO film exposed to ammonia solution with pH 11 for a) 1 week and b) 8 weeks.

EDS analysis was used to investigate the composition of the films during exposure to the solutions. EDS analyses were performed at time points of 1, 2, 4, and 8 weeks, corresponding to the SEM imaging. In the investigation, it was found that the chemical composition of the films did not alter notably during the first four weeks of immersion, except at pH 3, where the film had completely dissolved after only one week. In contrast, after eight weeks, notable changes in the zinc/oxygen ratio could be detected at pH 7 and pH 9 (Fig 42). The decrease in the Zn content observed for all the samples between the time points of 4 and 8 weeks can be explained by the dissolution of the film, which led to a thinner ZnO layer and thus lower Zn content and higher Fe content in the substrate. At pH 7, the initial Zn/O atomic ratio was 0.94. After eight weeks, the Zn/O atomic ratio for the sample at pH 7 had increased to approximately 1.1. In contrast, the Zn/O atomic ratio at pH 9 decreased from 0.93 to 0.52 during the eight-week period. This indicates that the rod structure at pH 9 after eight weeks was mainly hydroxide. At pH 7, zinc hydroxide flakes could be detected on top of the film. At pH 7, it was assumed that the dissolved zinc would form zinc hydroxide flakes while the rods that remained on the surface would still be mainly zinc oxide. This is supported by the fact that the atomic ratio of Zn/O was approximately 0.5 when the areas covered by flakes were analyzed, which indicated that the flake structure consisted of $Zn(OH)_2$. The Zn/O atomic ratios for the ZnO films before exposure and after eight weeks' exposure to the solutions with pH 3, 5, 7, 9, and 11 are shown in Table 3.

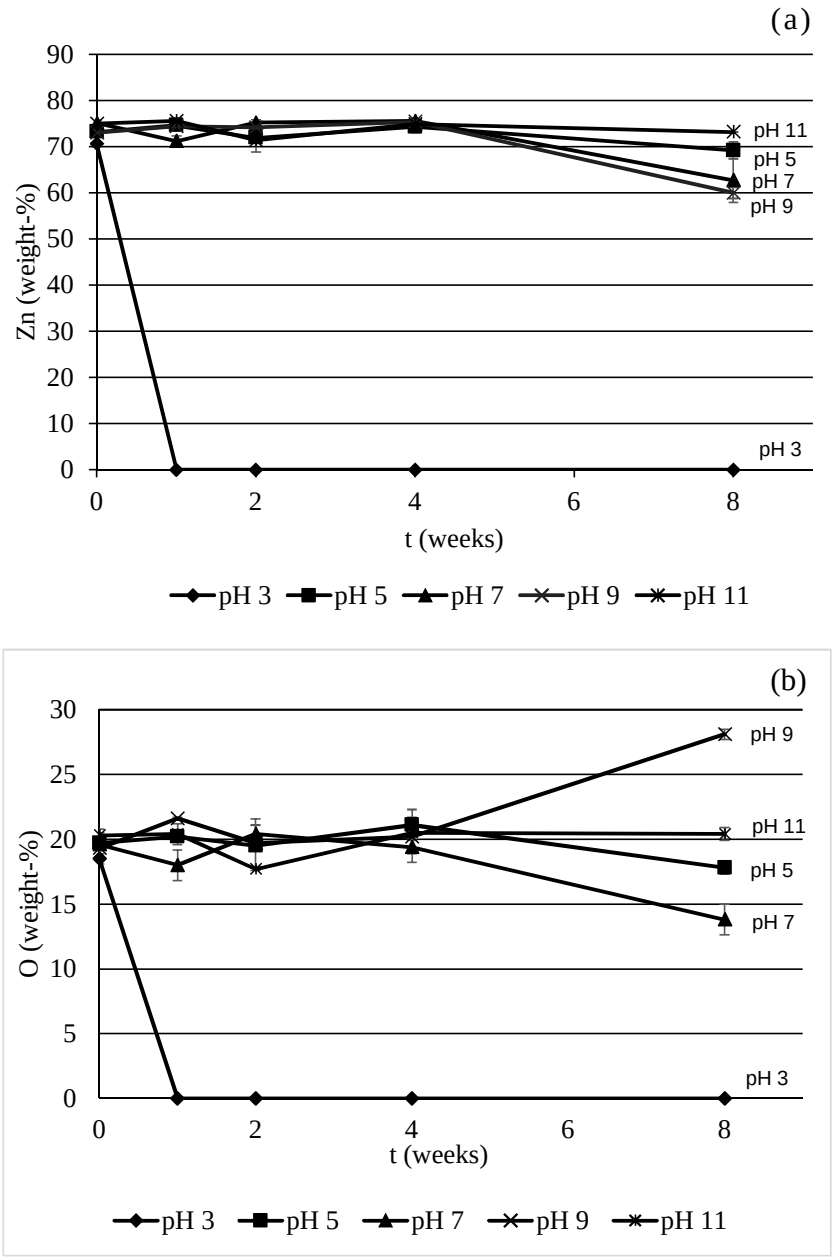

FIGURE 42 Weight percentages of a) Zn and b) O detected from the ZnO films in EDS analysis as a function of immersion time in solutions of different pH values. (Publication VI)

TABLE 3. Zn/O atomic ratios before exposure and after 8 weeks' exposure to solutions of pH 3, 5, 7, 9, and 11.

	0 h	*8 weeks*
pH 3	0.94	0
pH 5	0.91	0.95
pH 7	0.94	1.11
pH 9	0.93	0.52
pH 11	0.9	0.89

The pH of the solutions was monitored during the dissolution test. The pH was measured at 1, 2, 4, and 8 weeks of immersion. Interestingly, the pH of the solution with an initial pH of 5 increased during the test and stabilized slightly above pH 7. Similar behavior was detected for the solution with an initial pH of 9. The pH of the solution also decreased and stabilized at a pH value of slightly above 7. In contrast, the pH of solutions with initial pH values of 3 and 11 remained at the same level throughout the eight-week test period, as shown in Fig 43. It has been reported that the pH of a ZnO nanoparticle aqueous suspension is unstable in the regions of 4.4 < pH < 6.4 and 8.3 < pH < 10.5 [186]. This also appeared to be the case for the solutions in which the ZnO film was immersed.

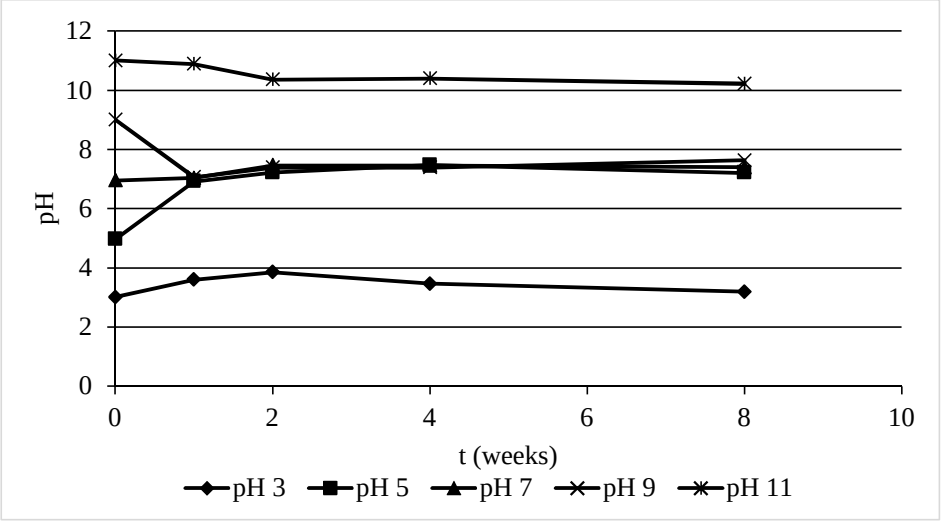

FIGURE 43 pH of the solutions in which the ZnO samples were immersed during the eight-week immersion test. (Publication VI)

The water contact angles of the ZnO films were also monitored during the immersion test to investigate chemical changes on the surface. Water contact angles were measured

after 1, 2, 4, and 8 weeks of immersion in the solutions and the results are shown in Fig. 44. The initial water contact angle of the film was 80º. In all the solutions, the water contact angles decreased notably after one week of exposure to the solutions. The water contact angle continued decreasing until two weeks of immersion, after which it slightly increased. Similar behavior was detected for all the films in different solutions except for the one in pH 3, where the ZnO film had completely dissolved after one week of immersion according to the FESEM images. The decrease in the water contact angle indicates a change in the chemical composition of the surface. The formation of a thin hydroxide layer can be assumed in the aqueous solution at all the pH values, which would explain the change from 80 º to approximately 20 degrees for all the samples.

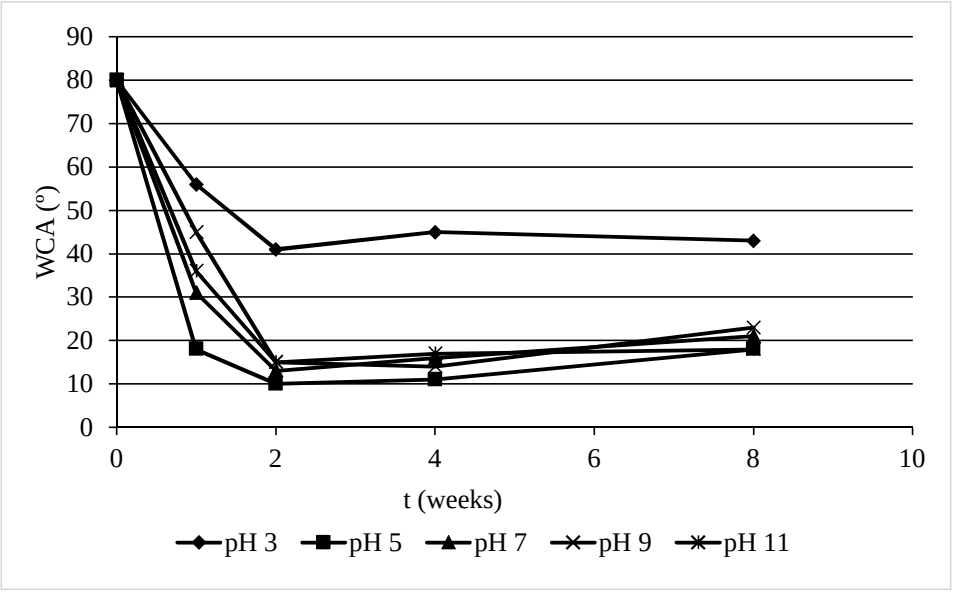

FIGURE 44 Water contact angles of the ZnO films during eight-week immersion in solutions with different pH values. (Publication VI)

As a conclusion, it was found that the ZnO films are most durable at pH 11. At pH 3, in contrast, the film was rapidly removed from the surface. At pH 5, the film did not undergo any clearly visible changes but the dissolution of zinc from the film was higher than that measured at pH 11. At pH 7, areas covered by flakes composing of zinc hydroxide could be detected. At pH 9, formation of zinc hydroxide on the surface was clear, according to the EDS analysis results. This would explain the decrease in the pH value as the hydroxide ions decreased in the solution as a result of the formation of zinc hydroxide.

6 CONCLUDING REMARKS AND SUGGESTIONS FOR FUTURE WORK

Functional surfaces offer a solution for materials requiring antibacterial activity. Such surfaces could be suitable/applicable in hospitals for instance or in industrial plants where cleaning surfaces incurs high costs. In this thesis, multifunctional antibacterial surfaces have been produced using two different approaches and their properties linked to antibacterial activity and self-cleaning ability investigated. Firstly, alumina-based silver-containing superhydrophobic surfaces were produced. Another approach selected in this thesis to produce an antibacterial surface was the manufacture of structured ZnO films. In addition to antibacterial activity, ZnO films were shown to possess remarkable photocatalytic activity. Investigation of the chemical resistance of the surfaces in varying conditions was also one focus of this study.

It was found that the superhydrophobic silver-containing surfaces exhibited high antibacterial activity compared to a pure stainless steel surface. Notable antibacterial efficiency was also detected for ZnO films. The chemical resistance of the specimens was investigated by exposing the surfaces to aqueous solutions with varying pH values. During the eight-week test period, both superhydrophobic and ZnO surfaces were clearly affected by the aqueous environment. It was shown that in the solution with low pH, both of the studied surfaces, ZnO and the superhydrophobic silver-containing surface, were severely damaged. The structure and the chemical composition of the ZnO films was best preserved at the highest tested pH value of 11. The film structure and chemical composition were also relatively well preserved at pH 5 during the eight-week investigation. In contrast, at pH 3, the ZnO film was rapidly moved from the surface. Moreover, at pH 9, the chemical composition of the ZnO film was found to change during the eight-week exposure as it was determined that the film was composed mainly of zinc hydroxide after eight weeks' immersion in the aqueous ammonia solution at pH 9. When considering the long-term usability of ZnO films in wet conditions for photocatalytic purposes, it must be noted that the formation of a thick zinc hydroxide layer on the surface deteriorates or prevents the photocatalytic action of the surface. The structure and composition of the ZnO films seemed to be best preserved at pH 11 in addition to pH 5, at which the film would have the longest usability based on these investigations.

In the case of the superhydrophobic silver-containing surface, the surface was completely removed at pH 1. Although the coating was preserved on the surface at high pH values (pH 13), the superhydrophobic property was lost. However, in milder conditions,

i.e., with a pH closer to 7, the surfaces preserved their properties relatively well during the eight-week investigation.

The influence of synthesis parameters in the formation of ZnO films was also investigated. The morphology can be controlled by changing synthesis parameters such as temperature as well as precursor concentration and composition. In addition to antibacterial activity, ZnO films exhibit relatively high photocatalytic activity, which is also dependent on the surface morphology. Photocatalytic activity promotes antibacterial property and is one means to obtain a self-cleaning surface. A photocatalyst requires radiation with high enough energy to excite electrons over the band gap. ZnO has a relatively wide band gap (3.37 in the literature) and thus it cannot be effectively used in sunlight as a photocatalyst. Decreasing the band gap energy would increase the photocatalytic efficiency of the photocatalyst in the visible light region. In this thesis, we studied the effect of morphology and precursor solution composition on band gap energy. The addition of copper nitrate to the precursor solution was found to decrease the band gap energy. Band gap energy was also found to be dependent on morphological changes. One explanation for the morphological dependence of the band gap is native surface defects (e.g., a higher surface to volume ratio and higher surface area of polar planes promotes formation of oxygen vacancies), which could lead to defect-induced band gap narrowing. [184]

To conclude, both superhydrophobic and ZnO surfaces offer a feasible solution when selecting a material for applications requiring a clean, bacteria-free surface. In this thesis, the surfaces were coated and grown on a stainless steel substrate, which enables their use in versatile environments and applications. The combination of superhydrophobic and antibacterial properties on the surface was proven to work effectively and has significant potential for self-cleaning antibacterial applications. Moreover, zinc oxide thin films have great potential as coating materials in antibacterial applications since, in addition to good antibacterial activity in the dark, they exhibit remarkable photocatalytic activity, which indicates significant light-induced antibacterial activity.

When the research questions introduced in the chapter 3 are considered, the following conclusions can be drawn: I) Superhydrophobic silver-containing coatings and structured ZnO films can effectively prevent bacterial growth on the surfaces. II) Superhydrophobic and ZnO surfaces withstand aqueous conditions relatively well at pH values close to 7. The ZnO films also endure well in basic conditions contrary to the superhydrophobic films. Both, superhydrophobic and ZnO films withstand badly strong acidic environment. III) The structure of hydrothermally grown ZnO films can effectively be altered by changing synthesis condition. Both, synthesis temperature and precursor concentration, contribute to the formation of the ZnO film structure. IV) The structure of the ZnO film was

found to influence the photocatalytic activity of the film. Instead, antibacterial activity was not found to be influenced by the surface structure. V) Addition of copper nitrate in the precursor solution decreased the band gap energy of the films. The higher the concentration of copper nitrate, the greater the decrease in the band gap energy.

The main focus for future work should be on developing the durability of superhydrophobic coatings as well as on a more intense study of the photocatalytic activity of ZnO films. The effect of doping with several metals and non-metals on photocatalytic activity will be the focus of the study and the visible light photocatalysis of the ZnO films will be investigated. The study of the antibacterial activity of ZnO will also be continued and the focus in that area is on determining the metabolism of the bacteria in order to detect the reason behind the cell death caused by ZnO surfaces.

Superhydrophobic films are currently utilized for example in clothing and packaging to prevent penetration of moisture into the material. Addition of silver onto the superhydrophobic surface extends the potential to applications that require easy-to-clean and antibacterial properties. Such applications could be found for example in food industry production lines or hospital environments. Zinc oxide thin films could be used in some applications to replace silver due to its non-toxic nature and less expensive costs compared to silver nanoparticles. Such applications could be for example in food packaging. Structured ZnO coatings with high surface area could also be utilized for instance, in air purification due to its photocatalytic activity. Utilization of ZnO in photocatalytic applications requires often the use of UV-light source, which must be taken into account when potential applications for ZnO are considered.

References

[1] S. K. Ghosh. Functional Coatings. WILEY-VCH Verlag GmbH & Co. KGaA, 2006.

[2] N. Durán, M. Durán, M. B. De Jesus, A. B. Seabra, W. J. Fávaro, G. Nakazato. Silver nanoparticles : A new view on mechanistic aspects on antimicrobial activity. Nanomedicine: Nanotechnology, Biology and Medicine 12 (2016) 3, pp. 789–799.

[3] J. Pasquet, Y. Chevalier, J. Pelletier, E. Couval, D. Bouvier, M. Bolzinger. The contribution of zinc ions to the antimicrobial activity of zinc oxide. Colloids and Surfaces A : Physicochemical and Engineering Aspects 457 (2014), pp. 263–274.

[4] Z. Guo, W. Liu, B. Su. Superhydrophobic surfaces: From natural to biomimetic to functional. Journal of Colloid and Interface Science 353 (2011), pp. 335–355.

[5] R. Fürstner, W. Barthlott. Wetting and Self-Cleaning Properties of Artificial Superhydrophobic Surfaces. Langmuir 21 (2005), pp. 956–961.

[6] A. Marmur. The lotus effect: Superhydrophobicity and metastability. Langmuir 20 (2004) 9, pp. 3517–3519.

[7] M. A. Samaha, H. V. Tafreshi, M. Gad-El-Hak. Superhydrophobic surfaces : From the lotus leaf to the submarine. Comptes Rendus Mecanique 340 (2012), pp. 18–34.

[8] X. Zhang, F. Shi, J. Niu, Y. Jiang, Z. Wang. Superhydrophobic surfaces : from structural control to functional application. Journal of Materials Chemistry 18 (2008), pp. 621–633.

[9] S. Dai, X. Han, Z. Du. Biomimetic fabrication and tunable wetting properties of three-dimensional hierarchical ZnO structures by combining soft lithography templated with lotus leaf and hydrothermal treatments. Crystal Engineering Communications 15 (2013), pp. 5417–5424.

[10] U. Mehmood, F. A. Al-sulaiman, B. S. Yilbas, B. Salhi, S. H. A. Ahmed, M. K. Hossain Solar Energy Materials & Solar Cells Superhydrophobic surfaces with antireflection properties for solar applications : A critical review. Solar Energy Materials & Solar Cells 157 (2016), pp. 604–623.

[11] Z. W. Han, Z. Wang, X. M. Feng, B. Li, Z. Z. Mu, J. Q. Zhang, S. C. Niu, L. Q. Ren. Antireflective surface inspired from biology : A review. Biosurface and Biotribology 2 (2016) 5988, pp. 137–150.

[12] V. Mortazavi, M. M. Khonsari. On the degradation of superhydrophobic surfaces: A review. Wear 372–373 (2017), pp. 145–157.

[13] R. J. Crawford, E. P. Ivanova. Superhydrophobic surfaces 1st Edition. Elsevier Inc., 2015.

[14] T. Young. An Essay on the Cohesion of Fluids. Philosophical Transactions of the Royal Society of London. 95 (1805), pp. 65–87.

[15] Y. Y. Yan, N. Gao, W. Barthlott. Mimicking natural superhydrophobic surfaces and grasping the wetting process : A review on recent progress in preparing superhydrophobic surfaces. Advances in Colloid and Interface Science 169 (2011), pp. 80–105.

[16] S. Giljean, M. Bigerelle, K. Anselme, H. Haidara. New insights on contact angle / roughness dependence on high surface energy materials. Applied Surface Science 257 (2011) 22, pp. 9631–9638.

[17] P. Roach, N. J. Shirtcliffe, M. I. Newton. Progess in superhydrophobic surface development. Soft Matter 4 (2008) 2, pp. 224–240.

[18] J. Shiu, C. Kuo, P. Chen, C. – Y. Mou. Fabrication of Tunable Superhydrophobic Surfaces by Nanosphere Litography 16 (2004) 4, pp. 561–564.

[19] L. Gao, T. J. Mccarthy. Contact Angle Hysteresis Explained. Langmuir 22 (2006), pp. 6234–6237.

[20] B. Wu, M. Zhou, J. Li, X. Ye, G. Li, L. Cai. Superhydrophobic surfaces fabricated by microstructuring of stainless steel using a femtosecond laser. Applied Surface Science 256 (2009), pp. 61–66.

[21] S. Heinonen, E. Huttunen-Saarivirta, J.-P. Nikkanen, M. Raulio, O. Priha, J. Laakso, E. Storgårds, E. Levänen. Antibacterial properties and chemical stability of superhydrophobic silver-containing surface produced by sol-gel route. Colloids and Surfaces A: Physicochemical and Engineering Aspects 453 (2014), pp. 149–161.

[22] Z. Kang, J. Zhang, L. Niu. A one-step hydrothermal process to fabricate superhydrophobic hydroxyapatite coatings and determination of their properties. Surface & Coatings Technology 334 (2017), pp. 84–89.

[23] A. Pozzato, S. Dal Zilio, G. Fois, D. Vendramin, G. Mistura, M. Belotti, Y. Chen, M. Natali. Superhydrophobic surfaces fabricated by nanoimprint lithography. Microelectronic Engineering 83 (2006), pp. 884–888.

[24] B. Qian, Z. Shen. Fabrication of Superhydrophobic Surfaces by Dislocation-Selective Chemical Etching on Aluminum, Copper, and Zinc Substrates. Langmuir 21 (2005), pp. 9007–9009.

[25] X. Song, J. Zhai, Y. Wang, L. Jiang. Fabrication of Superhydrophobic Surfaces by Self-Assembly and Their Water-Adhesion Properties. The Journal of Physical Chemistry B 109 (2005), pp. 4048–4052.

[26] X. Wu, L. Zheng, D. Wu. Fabrication of Superhydrophobic Surfaces from Microstructured ZnO-Based Surfaces via a Wet-Chemical Route. Langmuir 21 (2005), pp. 2665–2667.

[27] P. Zhang, F. Y. Lv. A review of the recent advances in superhydrophobic surfaces and the emerging energy-related applications. Energy 82 (2015), pp. 1068–1087.

[28] Z. Wang, Y. Su, Q. Li, Y. Liu, Z. She, F. Chen, L. Li, X. Zhang, P. Zhang. Researching a highly anti-corrosion superhydrophobic film fabricated on AZ91D magnesium alloy and its anti-bacteria adhesion effect. Materials Characterization 99 (2015), pp. 200–209.

[29] C. R. Crick, S. Ismail, J. Pratten, I. P. Parkin. An investigation into bacterial attachment to an elastomeric superhydrophobic surface prepared via aerosol assisted deposition. Thin Solid Films 519 (2011), pp. 3722–3727.

[30] P. Tang, W. Zhang, Y. Wang, B. Zhang, H. Wang, C. Lin, L. Zhang. Effect of Superhydrophobic Surface of Titanium on Staphylococcus aureus Adhesion. Journal of Nanomaterials 2011 (2011), pp. 2–10.

[31] B. J. Privett, J. Youn, S. A. Hong, J. Lee, J. Han, J. H. Shin, M. H. Schoenfisch. Antibacterial Fluorinated Silica Colloid Superhydrophobic Surfaces. Langmuir 27 (2011), pp. 9597–9601.

[32] C. – Y. Loo, P. M. Young, W. – H. Lee, R. Cavaliere, C. B. Whitchurch, R. Rohanizadeh. Superhydrophobic, nanotextured polyvinyl chloride films for delaying Pseudomonas aeruginosa attachment to intubation tubes and medical plastics. Acta Biomaterialia 8 (2012), pp. 1881–1890.

[33] M. Katsikogianni, Y. F. Missirlis. Concise Review of Mechanism of Bacterial Adhesion to Biomaterials and of Techniques used in estimating Bacteria and Material Interactions. European Cells and Materials 8 (2004), pp. 37–57.

[34] C. F. Klingshirn, B. K. Meyer, A. Waag, A. Hoffmann, J. Geurts. Zinc Oxide - From Fundamental Properties Towards Novel Applications. Springer, 2010 pp. 307–323.

[35] A. Di Mauro, M. E. Fragalà, V. Privitera, G. Impellizzeri. ZnO for application in photocatalysis : From thin films to nanostructures. Materials Science in Semiconductor Processing 69 (2017), pp. 44–51.

[36] J. Wang, R. Chen, L. Xiang, S. Komarneni. Synthesis , properties and applications of ZnO nanomaterials with oxygen vacancies: A review. Ceramics International 44 (2018), pp. 7357–7377.

[37] P. By. Advances in Ferroelectricity. Intech Open, A. Pelaiz-Barranco. 2012, pp. 231–255.

[38] A. Janotti, C. G. Van De Walle. Fundamentals of zinc oxide as a semiconductor. Reports on Progress in Physics 72 (2009), pp.126501.

[39] H. Morkoc, Ü. Özgür. Zinc Oxide Fundamentals, Materials and Device Technology. WILEY-VCH Verlag GmbH & Co. KGaA, 2009, pp. 1–477.

[40] S. – H. Feng, G. – H. Li. Modern Inorganic Synthetic Chemistry, Hydrothermal and Solvothermal Syntheses. Elsevier B.V., 2017, pp. 73–104.

[41] A. Rabenau. The Role of Hydrothermal Synthesis in Preparative Chemistry. Angewandte Chemie International Edition in English 24 (1985), pp. 1026–1040.

[42] A. D. Li, W. C. Liu. Optical properties of ferroelectric nanocrystal/polymer composites. Physical Properties and Applications of Polymer Nanocomposites, A volume in Woodhead Publishing Series in Composites Science and Engineering, Chapter 4, 2010, pp. 108–158.

[43] K. Byrappa, M. Yoshimura. Handbook of Hydrothermal Technology, Hydrothermal TechnologyHydrothermal Technology—Principles and Applications. Elsevier Inc. 2013, pp. 1–49.

[44] J. Yu, B. Huang, X. Qin, X. Zhang, Z. Wang, H. Liu. Hydrothermal Synthesis and Characterization of ZnO films with different Nanostructures. Applied surface Science 257 (2011), pp. 5563–5565.

[45] S. – W. Chen, J. – M. Wu. Nucleation mechanisms and their influences on characteristics of ZnO nanorod arrays prepared by a hydrothermal method. Acta Materialia 59 (2011), pp. 841–847.

[46] T. Dedova, I. O. Acik, M. Krunks, V. Mikli, O. Volobujeva, A. Mere. Effect of substrate morphology on the nucleation and growth of ZnO nanorods prepared by spray pyrolysis. Thin Solid Films 520 (2012), pp. 4650–4653.

[47] H. Saarenpää, E. Sariola-Leikas, A. Pyymäki Perros, J. M. Kontio, A. Efimov, H. Hayashi, H. Lipsanen, H. Imahori, H. Lemmetyinen, N. V. Tkachenko. Self-Assembled Porphyrins on Modified Zinc Oxide Nanorods: Development of Model Systems for Inorganic − Organic Semiconductor Interface Studies. The Journal of Physical Chemistry C 116 (2012), pp. 2336–2343.

[48] H. – G. Chen, Z. – W. Li, H. – D. Lian. Control of epitaxial growth orientation in ZnO nanorods on c -plane sapphire substrates. Thin Solid Films 518 (2010), pp. 5520–5524.

[49] Y. Zhou, C. Liu, X. Zhong, H. Wu, M. Li, L. Wang. Simple hydrothermal preparation of new type of sea urchin-like hierarchical ZnO micro / nanostructures and their formation mechanism. Ceramics International 40 (2014), pp. 10415–10421.

[50] M. A. Abbasi, Y. Khan, S. Hussain, O. Nur, M. Willander. Anions effect on the low temperature growth of ZnO nanostructures. Vacuum 86 (2012), pp. 1998–2001.

[51] D. Chen, X. Jiao, G. Cheng. Hydrothermal synthesis of zinc oxide powders with different morphologies. Solid State Communications 113 (2000), pp. 363–366.

[52] C. – H. Lu, C. – H. Yeh. Influence of hydrothermal conditions on the morphology and particle size of zinc oxide powder. Ceramics Internationla 26 (2000), pp. 351–357.

[53] R. Savu, R. Parra, E. Joanni, B. Jancar, S. A: Eliziario, R. de Camargo, P. R. Bueno, J. A. Varela, E. Longo, M. A. Zaghete. The effect of cooling rate during hydrothermal synthesis of ZnO nanorods. Journal of Crystal Growth 311 (2009), pp. 4102–4108.

[54] L. B. Khalil, W. E. Mourad, M. W. Rophael. Photocatalytic reduction of environmental pollutant Cr (VI) over some semiconductors under UV / visible light illumination. Applied Catalysis B: Environmental 17 (1998), pp. 267–273.

[55] P. Magalh, L. Andrade, O. C. Nunes, A. Mendes, Titanium dioxide photocatalysis: Fundamentals and applications on photoactivation. Reviews on advanced mate-rials science 51 (2017), pp. 91–129.

[56] K. M. Lee, C. W. Lai, K. S. Ngai, J. C. Juan. Recent developments of zinc oxide based photocatalyst in water treatment technology : A review. Water Research 88 (2016), pp. 428–448.

[57] A. Mills, S. Le Hunte. An overview of semiconductor photocatalysis. Journal of Photochemistry and Photobiology A: Chemistry 108 (1997) pp. 1–35.

[58] S. Lacombe, N. Keller. Photocatalysis : fundamentals and applications in JEP 2011. Environmental Science and Pollution Research 19 (2012), pp. 3651–3654.

[59] A. Fujishima, K. Honda. Electrochemical Photolysis of Water at a Semiconductor Electrode. Nature 238 (1972), pp. 37–38.

[60] C. B. Ong, L. Y. Ng, A. W. Mohammad. A review of ZnO nanoparticles as solar photocatalysts : Synthesis , mechanisms and applications. Renewable and Sustainable Energy Reviews 81 (2018), pp. 536–551.

[61] A. M. Ali, E. A. C. Emanuelsson, D. A. Patterson. Photocatalysis with nanostructured zinc oxide thin films : The relationship between morphology and photocatalytic activity under oxygen limited and oxygen rich conditions and evidence for a

Mars Van Krevelen mechanism. Applied Catalysis B : Environmental 97 (2010), pp. 168–181.

[62] S. Sakthivel, B. Neppolian, M. V Shankar, B. Arabindoo, M. Palanichamy, V. Murugesan. Solar photocatalytic degradation of azo dye : comparison of photocatalytic efficiency of ZnO and TiO2. Solar Energy Materials & Solar Cells 77 (2003), pp. 65–82.

[63] J. Han, W. Qiu, W. Gao. Potential dissolution and photo-dissolution of ZnO thin films. Journal of Hazardous materials 178 (2010), pp. 115–122.

[64] Y. Liao, C. Xie, Y. Liu, H. Chen, H. Li, J. Wu. Comparison on photocatalytic degradation of gaseous formaldehyde by TiO2 , ZnO and their composite. Ceramic International 38 (2012), pp. 4437–4444.

[65] M. Samadi, M. Zirak, A. Naseri, E. Khorashadizade, A. Z. Moshfegh. Recent progress on doped ZnO nanostructures for visible-light photocatalysis. Thin Solid Films 605 (2016), pp. 2–19.

[66] M. T. Man, J. – H. Kim, M. S. Jeong, A. – T. T. Do, H. S. Lee. Oriented ZnO nanostructures and their application in photocatalysis. Journal of Luminescence 185 (2017), pp. 17–22.

[67] M. Hosni, Y. Kusumawati, S. Farhat, N. Jouini, T. Pauporte. Effects of Oxide Nanoparticle Size and Shape on Electronic Structure, Charge Transport, and Recombination in Dye-Sensitized Solar Cell Photoelectrodes. The Journal of Physical Chemistry C 118 (2014), pp. 16791–16798.

[68] R. Gupta, N. K. Eswar, J. M. Modak, G. Madras. Ag and CuO impregnated on Fe doped ZnO for bacterial inactivation under visible light. Catalysis Today 300 (2018), pp. 71–80.

[69] S. – M. Lam, J. – A. Quek, J. – C. Sin. Mechanistic investigation of visible light responsive Ag / ZnO micro / nano fl owers for enhanced photocatalytic performance and antibacterial activity. Journal of Photochemistry and Photobiology A : Chemistry 353 (2018), pp. 171–184.

[70] J. Low, B. Cheng, J. Yu. Surface modification and enhanced photocatalytic CO2 reduction performance of TiO2 : a review. Applied Surface Science 392 (2017), pp. 658–686.

[71] K. Qi, B. Cheng, J. Yu, W. Ho. Review on the improvement of the photocatalytic and antibacterial activities of ZnO. Journal of Alloys and Compounds 727 (2017), pp. 792–820.

[72] S. Jung, K. Yong. Fabrication of CuO – ZnO nanowires on a stainless steel mesh for highly efficient photocatalytic applications. Chemical Communications 47 (2011), pp. 2643–2645.

[73] Q. Zhang, J. – K. Liu, J. – D. Wang, H. – X. Luo, Y. Lu, X. – H. Yang. Atmospheric Self-induction Synthesis and Enhanced Visible Light Photocatalytic Performance of Fe3+ Doped Ag-ZnO Mesocrystals. Industrial & Engineering Chemistry Research 53 (2014), pp. 13236–13246.

[74] Q. Yin, R. Qiao, Z. Li, X. L. Zhang, L. Zhu. Hierarchical nanostructures of nickel-doped zinc oxide : Morphology controlled synthesis and enhanced visible-light photocatalytic activity. Journal of Alloys and Compounds 618 (2015), pp. 318–325.

[75] R. Ullah, J. Dutta. Photocatalytic degradation of organic dyes with manganese-doped ZnO nanoparticles. Journal of Hazardous Materials 156 (2008), pp. 194–200.

[76] M. Fu, Y. Li, S. Wu, P. Lu, J. Liu, F. Dong. Sol – gel preparation and enhanced photocatalytic performance of Cu-doped ZnO nanoparticles. Applied Surface Science 258 (2011), pp. 1587–1591.

[77] F. Achouri, S. Corbel, L. Balan, K. Mozet, E. Girot, G. Medjahdi, M. B. Said, A. Ghrabi, R. Schneider. Porous Mn-doped ZnO nanoparticles for enhanced solar and visible light photocatalysis. Materials and Design 101 (2016), pp. 309–316.

[78] A. Tabib, W. Bouslama, B. Sieber, A. Addad, H. Elhouichet, M. Ferid, R. Boukherroub. Structural and optical properties of Na doped ZnO nanocrystals : Application to solar photocatalysis. Applied Surface Science 396 (2017), pp. 1528–1538.

[79] X. Qiu, L. Li, J. Zheng, J. Liu, X. Sun, G. Li. Origin of the Enhanced Photocatalytic Activities of Semiconductors : A Case Study of ZnO Doped with Mg2+. The Journal of Physical Chemistry C 112 (2008), pp. 12242–12248.

[80] J. C. Fan, K. M. Sreekanth, Z. Xie, S. L. Chang, K. V Rao. p-Type ZnO materials : Theory , growth , properties and devices. Progress in Materials Science 58 (2013), pp. 874–985.

[81] Y. Wang, H. – B. Fang, Y. – Z. Zheng, R. Ye, X. Tao, J. – F. Chen. Controllable assembly of well-defined monodisperse Au nanoparticles on hierarchical ZnO microspheres for enhanced visible-light- driven photocatalytic and antibacterial activity. Nanoscale 7 (2015), pp. 19118–19128.

[82] C. – M. Chou, Y. – C. Chang, P. – S. Lin, F. – K. Liu. Growth of Cu-doped ZnO nanowires or ZnO-CuO nanowires on the same brass foil with high performance photocatalytic activity and stability. Material Chemistry and Physics 201 (2017), pp. 18–25.

[83] J. R. Torres-Hernández, E. Ramírez-Morales, L. Rojas-Blanco, J. Pantoja-Enriquez, G. Oskam, F. Paraguay-Delgado, B. Escobar-Morales, M. Acosta-Alejandro, L. L. Díaz-Flores, G. Perez-Hernández. Structural, optical and photocatalytic properties of ZnO nanoparticles modified with Cu. Materials Science in Semiconductor Processing 37 (2015), pp. 87–92.

[84] F. Ghahramanifard, A. Rouhollahi, O. Fazlolahzadeh. Electrodeposition of Cu-doped p-type ZnO nanorods ; effect of Cu doping on structural, optical and photoelectrocatalytic property of ZnO nanostructure. Superlattices and Microstructures 114 (2018), pp. 1–14.

[85] L. – C. Chen, Y. – J. Tu, Y. – S. Wang, R. – S. Kan, C. – M. Huang. Characterization and photoreactivity of N- , S- , and C-doped ZnO under UV and visible light illumination. Journal of Photochemistry and Photobiology A : Chemistry 199 (2008), pp. 170–178.

[86] C. Di Valentin, G. Pacchioni. Spectroscopic Properties of Doped and Defective Semiconducting Oxides from Hybrid Density Functional Calculations. Accounts of Chemical Research 47 (2014), pp. 3233–3241.

[87] Z. Li, S. Sun, X. Xu, B. Zheng, A. Meng. Photocatalytic activity and DFT calculations on electronic structure of N-doped ZnO/Ag nanocomposites. Catalysis Communications 12 (2011), pp. 890–894.

[88] S. Kuriakose, S. Mohapatra. Enhanced photocatalytic activity of Co doped ZnO nanodisks and nanorods prepared by a facile wet chemical method. Physical Chemistry Chemical Physics 16 (2014), pp. 12741–12749.

[89] L. C. – K. Liau, J. – S. Huang. Energy-level variations of Cu-doped ZnO fabricated through sol-gel processing. Journal of Alloys and Compounds 702 (2017), pp. 153–160.

[90] A. Hui, J. Ma, J. Liu, Y. Bao, J. Zhang. Morphological evolution of Fe doped sea urchin-shaped ZnO nanoparticles with enhanced photocatalytic activity. Journal of Alloys and Compounds 696 (2017), pp. 639–647.

[91] N. Talebian, S. M. Amininezhad, M. Doudi. Controllable synthesis of ZnO nanoparticles and their morphology-dependent antibacterial and optical properties. Journal of Photochemistry and Photobiology B : Biology 120 (2013), pp. 66–73.

[92] L. Zhang, L. Yin, C. Wang, N. Lun, Y. Qi. Sol - Gel Growth of Hexagonal Faceted ZnO Enhanced Photocatalytic Activity. Applied Materials & Interfaces 2 (2010), pp. 1769–1773.

[93] G. R. Li, T. Hu, G. L. Pan, T. Y. Yan, X. P. Gao, H. Y. Zhu. MorphologyFunction Relationship of ZnO: Polar Planes ,Oxygen Vacancies and Activity. The Journal of Physical Chemistry C 112 (2008), pp. 11859–11864.

[94] T. Schwartz, W. Kohnen, B. Jansen, U. Obst. Detection of antibiotic-resistant bacteria and their resistance genes in wastewater, surface water, and drinking water biofilms. FEMS Microbiology Ecology 43 (2003), pp. 325–335.

[95] K. K. Kumarasamy, M. A. Toleman, T. R. Walsh, J. Bagaria, F. Butt, R. Balakrishnan, U. Chaudhary, M. Doumith, C. G: Giske, S. Irfan, P. Krishnan, A. V. Kumar, S. Maharjan, S. Mushtaq, T. Noorie, D. L. Paterson, A. Pearson, C. Perry, R. Pike, B. Rao, U. Ray, J. B. Sarma, M. Sharma, E. Sheridan, M. A. Thirunarayan, J. Turton, S. Upadhyay, M. Warner, W. Welfare, D. M. Livermore, N. Woodford. Emergence of a new antibiotic resistance mechanism in India, Pakistan, and the UK: a molecular, biological, and epidemiological study. The Lancet Infectious Diseases 10 (2010), pp. 597–602.

[96] R. Baquero, J. – L. Martinez, R. Canton. Antibiotics and antibiotic resistance in water environments. Current Opinion on Biotechnology 19 (2008), pp. 260–265.

[97] M. Yasuyuki, K. Kunihiro, S. Kurissery, N. Kanavillil, Y. Sato, Y. Kikuchi. Antibacterial properties of nine pure metals : A laboratory study using Staphylococcus aureus and Escherichia coli. Biofouling 26 (2010), pp. 851–858.

[98] M. Vincent, P. Hartemann, M. Engels-Deutsch. Antimicrobial applications of copper. International Journal of Hygiene and Environmental Health 219 (2016), pp. 585–591.

[99] Y. T. Prabhu, K. V. Rao, V. S. Sai, T. Pavani. A facile biosynthesis of copper nanoparticles : A micro-structural and antibacterial activity investigation. Journal of Saudi Chemical Society 21 (2017), pp. 180–185.

[100] E. Mcgillicuddy, I. Murray, S. Kavanagh, L. Morrison, A. Fogarty, M. Cormican, P. Dockery, M. Prendergast, N. Rowan, D. Morris. Silver nanoparticles in the environment : Sources, detection and ecotoxicology. Science of the Total Environment 575 (2017), pp. 231–246.

[101] S. M. Dizaj, F. Lotfipour, M. Barzegar-Jalali, M. H. Zarrintan, K. Adibkia. Antimicrobial activity of the metals and metal oxide nanoparticles. Materials Science and Engineering C 44 (2014), pp. 278–284.

[102] M. Guzman, J. Dille, S. Godet. Synthesis and antibacterial activity of silver nanoparticles against gram-positive and gram-negative bacteria. Nanomedicine: Nanotechnology, Biology and Medicine 8 (2012), pp. 37–45.

[103] T. C. Dakal, A. Kumar, R. S. Majumdar, V. Yadav. Mechanistic Basis of Antimicrobial Actions of Silver Nanoparticles. Frontiers in Microbiology 7 (2016), pp. 1–17.

[104] T. Chatterjee, B. K. Chatterjee, D. Majumdar, P. Chakrabarti. Antibacterial effect of silver nanoparticles and the modeling of bacterial growth kinetics using a modified Gompertz model. Biochimica et Biophysica Acta 1850 (2015), pp. 299–306.

[105] U. Bogdanovic, V. Lazic, V. Vodnik, M. Budimir, Z. Markovic, and S. Dimitrijevic, Copper nanoparticles with high antimicrobial activity Materials Letters 128 (2014), pp. 75–78.

[106] Y. Zhou, Y. Kong, S. Kundu, J. D. Cirillo, H. Liang. Antibacterial activities of gold and silver nanoparticles against Escherichia coli and bacillus Calmette-Guerin. Journal of Nanobiotechnology 10 (2012), pp. 1–9.

[107] R. B. – K. Wakshlak, R. Pedahzur, B. Menagen, D. Avnir. An antibacterial copper composite more bioactive than metallic silver. Journal of Materials Chemistry B. 4 (2016), pp. 4322–4329.

[108] J. Ramyadevi, K. Jeyasubramanian, A. Marikani, G. Rajakumar, A. A. Rahuman. Synthesis and antimicrobial activity of copper nanoparticles. Materials Letters 71 (2012), pp. 114–116.

[109] M. Rai, A. Yadav, A. Gade. Silver nanoparticles as a new generation of antimicrobials. Biotechnology Advances 27 (2009), pp. 76–83.

[110] B. Le Ouay, F. Stellacci. Antibacterial activity of silver nanoparticles : A surface science insight. Nano Today 10 (2015), pp. 339–354.

[111] R. Guerra, E. Lima, A. Guzmán. Antimicrobial supported nanoparticles: Gold versus silver for the cases of Escherichia coli and Salmonella typhi. Microporous and Mesoporous Materials 170 (2013), pp. 62–66.

[112] J. L. Hobman, L. C. Crossman. Bacterial antimicrobial metal ion resistance. Journal of Medical Microbiology 64 (2014), pp. 471–497.

[113] J. Liu, F. Li, H. Wang, B. Ren, K. Yang, E. Zhang. Effect of Cu content on the antibacterial activity of titanium–copper sintered alloys. Materials Science & Engineering C: Materials for Biological Applications 35 (2014), pp. 392–400.

[114] Y. – W. Baek, Y. – J. An. Microbial toxicity of metal oxide nanoparticles (CuO, NiO, ZnO, and Sb2O3) to Escherichia coli, Bacillus subtilis, and Streptococcus aureus. Science of the Total Environment 409 (2011), pp. 1603–1608.

[115] V. Aruoja, H. – C. Dubourguier, K. Kasemets, A. Kahru. Toxicity of nanoparticles of CuO, ZnO and TiO2 to microalgae Pseudokirchneriella subcapitata. Science of the Total Environment 407 (2009), pp. 1461–1468.

[116] K. Ravichandran, N. Chidhambaram, S. Gobalakrishnan. Copper and Graphene activated ZnO nanopowders for enhanced photocatalytic and antibacterial activities. Journal of Physics and Chemistry of Solids 93 (2016), pp. 82–90.

[117] M. Ramani, S. Ponnusamy, C. Muthamizhchelvan, J. Cullen, S. Krishnamurthy, E. Marsili. Morphology-directed synthesis of ZnO nanostructures and their antibacterial activity. Colloids and Surfaces B : Biointerfaces 105 (2013), pp. 24–30.

[118] J. Podporska-carroll, A. Myles, B. Quilty, D. E. McCormack, R. Fagan, S. J. Hinder, D. D. Dionysiou, S. C. Pillai. Antibacterial properties of F-doped ZnO visible light photocatalyst. Journal of Hazardous Materials 324 (2017), pp. 39–47.

[119] K. Dedková, B. Janíková, K. Matejová, P. Peikertová, L. Neuwirthová, J. Holešinsky, J. Kukutschová. Preparation, characterization and antibacterial properties of ZnO/kaoline nanocomposites. Journal of Photochemistry and Photobiology B: Biology 148 (2015), pp. 113–117.

[120] K. – H. Park, G. D. Han, K. C. Neoh, T. – S. Kim, J. H. Shim, H. – D. Park. Antibacterial activity of the thin ZnO film formed by atomic layer deposition under UV-A light. Chemical Engineering Journal 328 (2017), pp. 988–996.

[121] R. Pandimurugan, S. Thambidurai. UV protection and antibacterial properties of seaweed capped ZnO nanoparticles coated cotton fabrics. International Journal of Biological Macromolecules 105 (2017), pp. 788–795.

[122] H. Mirzaei, M. Darroudi. Zinc oxide nanoparticles: Biological synthesis and biomedical applications. Ceramics International 43 (2017), pp. 907–914.

[123] Z. Lu, J. Gao, Q. He, J. Wu, D. Liang, H. Yang, R. Chen. Enhanced antibacterial and wound healing activities of microporous chitosan-Ag/ZnO composite dressing. Carbohydrate Polymers 156 (2017), pp. 460–469.

[124] S. – M. Lam, J. – A. Quek, J. – C. Sin. Surfactant-free synthesis of ZnO micro/nanoflowers with efficient photocatalytic antibacterial performance. Materials Letters 195 (2017), pp. 34–36.

[125] R. Kumar, A. Umar, G. Kumar, H. S. Nalwa. Antimicrobial properties of ZnO nanomaterials: A review. Ceramics International 43 (2017), pp. 3940–3961.

[126] K. Kaviyarasu, C. M. Magdalene, K. Kanimozhi, J. Kennedy, B. Siddharda, E. Subba Reddy, N. Kumar Rotte, C. Shekhar Sharma, F. T. Thema, D. Letsholathebe, G. T. Mola, M. Maaza. Elucidation of photocatalysis, photoluminescence and antibacterial studies of ZnO thin films by spin coating method. Journal of Photochemistry & Photobiology, B: Biology 173 (2017), pp. 466–475.

[127] M. – L. Kääriäinen, C. K. Weiss, S. Ritz, S. Pütz, D. C: Cameron, V. Mailänder, K. Landfester. Zinc release from atomic layer deposited zinc oxide thin films and its antibacterial effect on Escherichia coli. Applied Surface Science 287 (2013), pp. 375–380.

[128] A. Joe, S. – H. Park, K. – D. Shim, D. – J. Kim, K. – H. Jhee, H. – W. Lee, C. – H. Heo, H. – M. Kim, E. – S. Jang. Antibacterial mechanism of ZnO nanoparticles under dark conditions. Journal of Industrial and Engineering Chemistry 45 (2017), pp. 430–439.

[129] D. – H. Jin, D. Kim, Y. Seo, H. Park, Y. – D. Huh. Morphology-controlled synthesis of ZnO crystals with twinned structures and the morphology dependence of their antibacterial activities. Materials Letters 115 (2014), pp. 205–207.

[130] Y. Jiang, L. Zhang, D. Wen, Y. Ding. Role of physical and chemical interactions in the antibacterial behavior of ZnO nanoparticles against E. coli. Materials Science and Engineering C 69 (2016), pp. 1361–1366.

[131] W. Jiang, H. Mashayekhi, B. Xing. Bacterial toxicity comparison between nano- and micro-scaled oxide particles. Environmental Pollution 157 (2009), pp. 1619–1625.

[132] J. Iqbal, N. Safdar, T. Jan, M. Ismail, S. S. Hussain, A. Mahmood, S. Shahzad, Q. Mansoor. Facile Synthesis as well as Structural, Raman, Dielectric and Antibacterial Characteristics of Cu Doped ZnO Nanoparticles. Journal of Materials Science & Technology 31 (2015), pp. 300–304.

[133] J. Iqbal, T. Jan, M. Ismail, N. Ahmad, A. Arif, M. Khan, M. Adil, Sami-ul-Haq, A. Arshad. Influence of Mg doping level on morphology, optical, electrical properties and antibacterial activity of ZnO nanostructures. Ceramics International 40 (2014), pp. 7487–7493.

[134] S. – C. Huang, K. M. Hsieh, T. W. Chang, Y. C. Chen, C. – T. R. Yu, T. – C. Lu, C. F. Lin, T. – Y. Yu, T. – T. Wang, H. Chen. ZnO nano flakes on silver wires with antibacterial effects. Ceramics International 42 (2016), pp. 7848–7851.

[135] D. Gao, L. Lyu, B. Lyu, J. Ma, L. Yang, J. Zhang. Multifunctional cotton fabric loaded with Ce doped ZnO nanorods. Materials Research Bulletin 89 (2017), pp. 102–107.

[136] Y. Zhang, X. Gao, L. Zhi, X. Liu, W. Jiang, Y. Sun, J. Yang. The synergetic antibacterial activity of Ag islands on ZnO (Ag/ZnO) heterostructure nanoparticles and its mode of action. Journal of Inorganic Biochemistry 130 (2014), pp. 74–83.

[137] R. K. Dutta, B. P. Nenavathu, M. K. Gangishetty. Correlation between defects in capped ZnO nanoparticles and their antibacterial activity. Journal of Photochemistry and Photobiology B: Biology 126 (2013), pp. 105–111.

[138] L. C. Ann, S. Mahmud, S. K. M. Bakhori, A. Sirelkhatim, D. Mohamad, H. Hasan, A. Seeni, R. A. Rahman. Antibacterial responses of zinc oxide structures against Staphylococcus aureus, Pseudomonas aeruginosa and Streptococcus pyogenes. Ceramics International 40 (2014), pp. 2993–3001.

[139] O. Bechambi, M. Chalbi, W. Najjar, S. Sayadi. Photocatalytic activity of ZnO doped with Ag on the degradation of endocrine disrupting under UV irradiation and the investigation of its antibacterial activity. Applied Surface Science 347 (2015), pp. 414–420.

[140] S. Baek, S. H. Joo, N. Kumar, M. Toborek. Antibacterial effect and toxicity pathways of industrial and sunscreen ZnO nanoparticles on Escherichia coli. Journal of Environmental Chemical Engineering 5 (2017), pp. 3024–3032.

[141] M. Altunbek, A. Baysal, M. Culha. Influence of surface properties of zinc oxide nanoparticles on their cytotoxicity. Colloids and Surfaces B : Biointerfaces 121 (2014), pp. 106–113.

[142] K. Akhil, J. Jayakumar, G. Gayathri, S. S. Khan. Effect of various capping agents on photocatalytic, antibacterial and antibiofilm activities of ZnO nanoparticles. Journal of Photochemistry & Photobiology, B : Biology 160 (2016), pp. 32–42.

[143] L. Zhang, Y. Jiang, Y. Ding, N. Daskalakis, L. Jeuken, M. Povey, A. J. O'Neill, D. W. York. Mechanistic investigation into antibacterial behaviour of suspensions of ZnO nanoparticles against E. coli. The Journal of Nanoparticle Research 12 (2010) pp. 1625–1636.

[144] S. Vignesh, J. K. Sundar. Investigations of visible light driven Sn and Cu doped ZnO hybrid nanoparticles for photocatalytic performance and antibacterial activity. Applied Surface Science 449 (2018), pp. 617–630.

[145] V. Lakshmi Prasanna, R. Vijayaraghavan. Chemical manipulation of oxygen vacancy and antibacterial activity in ZnO. Materials Science and Engineering C 77 (2017), pp. 1027–1034.

[146] A. Stankovic, S. Dimitrijevic, D. Uskokovic. Influence of size scale and morphology on antibacterial properties of ZnO powders hydrothemally synthesized using different surface stabilizing agents. Colloids and Surfaces B : Biointerfaces 102 (2013), pp. 21–28.

[147] A. Sirelkhatim, S. Mahmud, and A. Seeni, N. H. M. Kaus, L. C. Ann, S. K. M. Bakhori, H. Hasan, D. Mohamad. Review on Zinc Oxide Nanoparticles: Antibacterial Activity and Toxicity Mechanism. Nano-Micro Letters 7 (2015), pp. 219–242.

[148] W. Sangchay, A. Namsai. Antibacterial activity of ZnO powders against Stahylococcus aureus. Materials Today: Proceedings 4 (2017), pp. 6436–6443.

[149] Z. H. Chohan, M. Arif, M. A. Akhtar, C. T. Supuran. Metal-based antibacterial and antifungal agents: Synthesis, characterization, and in vitro biological evaluation of Co(II), Cu(II), Ni(II), and Zn(II) complexes with amino acid-derived compounds. Bioinorganic Chemistry and Applications 2006 (2006), pp. 1–13.

[150] Z. Ma, F. E. Jacobsen, D. P. Giedroc. Coordination Chemistry of Bacterial Metal Transport and Sensing. Chemical Reviews 109 (2009), pp. 4644–4681.

[151] K. L. Haas, K. J. Franz. Application of Metal Coordination Chemistry To Explore and Manipulate Cell Biology. Chemical Reviews 109 (2009), pp. 4921–4960.

[152] R. G. Parr, R. G. Pearson. Absolute Hardness: Companion Parameter to Absolute Electronegativity. Journal of the American Chemical Society 105 (1983), pp. 7512–7516.

[153] R. G. Pearson. Hard and Soft Acids and Bases. Journal of the American Chemical Society 85 (1963), pp. 3533–3539.

[154] L. A. Finney, T. V. O'Halloran. Transition Metal Speciation in the Cell: Insights from the Chemistry of Metal Ion Receptors. 300 (2003), pp. 931–937.

[155] M. L. Workentine, J. J. Harrison, P. U. Stenroos, H. Ceri, R. J. Turner. Pseudomonas fluorescens' view of the periodic table. Environmental Microbiology 10 (2008), pp. 238–250.

[156] J. A. Lemire, J. J. Harrison, R. J. Turner. Antimicrobial activity of metals: mechanisms, molecular targets and applications. Nature Reviews Microbiology 11 (2013), pp. 371–384.

[157] H. J. Klasen. Historical review of the use of silver in the treatment of burns. I. Early uses. Burns 26 (2000), pp. 117–130.

[158] P. Dallas, V. K. Sharma, R. Zboril. Silver polymeric nanocomposites as advanced antimicrobial agents: Classification, synthetic paths, applications, and perspectives. Advances in Colloid and Interface Science 166 (2011), pp. 119–135.

[159] V. Sambhy, M. M. Macbride, B. R. Peterson, A. Sen. Silver Bromide Nanoparticle/Polymer Composites: Dual Action Tunable Antimicrobial Materials. Journal of American Chemical Society 128 (2006), pp. 9798–9808.

[160] K. Kawahara, K. Tsuruda, M. Morishita, M. Uchida. Antibacterial effect of silver-zeolite on oral bacteria under anaerobic conditions. 16 (2000), pp. 452–455.

[161] B. M. Barngrover, C. M. Aikens. Incremental Binding Energies of Gold (I) and Silver (I) Thiolate Clusters. The Journal of Physical Chemistry A 115 (2011), pp. 11818–11823.

[162] A. N. Parikh, S. D. Gillmor, J. D. Beers, K. M. Beardmore, R. W. Cutts, B. I. Swanson. Characterization of Chain Molecular Assemblies in Long-Chain, Layered Silver Thiolates: A Joint Infrared Spectroscopy and X-ray Diffraction Study. The Journal of Physical Chemistry B 103 (1999), pp. 2850–2861.

[163] I. Sondi, B. Salopek-Sondi. Silver nanoparticles as antimicrobial agent: a case study on E. coli as a model for Gram-negative bacteria. Journal of Colloid and Interface Science 275 (2004), pp. 177–182.

[164] H. – L. Su, C. – C. Chou, D. – J. Hung, S. – H. Lin, I. - C. Pao, J. – H. Lin, F. – L. Huang, R. – X. Dong, J. – J. Lin. The disruption of bacterial membrane integrity through ROS generation induced by nanohybrids of silver and clay. Biomaterials 30 (2009), pp. 5979–5987.

[165] A. Vessey, Contact Killing on Copper Surfaces: From Lab to Application. International Pharmaceutical Industry 7 (2015), pp. 58–62.

[166] M. Hans, A. Erbe, S. Mathews, Y. Chen, M. Solioz, F. Mücklich. Role of copper oxides in contact killing of bacteria. Langmuir 29 (2013), pp. 16160–16166.

[167] T. Xia, M. Kovochich, M. Liong, L. Mädler, B. Gilbert, H. Shi, J. I. Yeh, J. I. Zink, A. E. Nel. Comparison of the Mechanism of Toxicity of Zinc Oxide and Cerium Oxide Nanoparticles Based on Dissolution and Oxidative Stress Properties. American Chemical Society nano 2 (2008), pp. 2121–2134.

[168] K. R. Raghupathi, R. T. Koodali, A. C. Manna. Size-Dependent Bacterial Growth Inhibition and Mechanism of Antibacterial Activity of Zinc Oxide Nanoparticles. Langmuir 27 (2011), pp. 4020–4028.

[169] M. Heinlaan, A. Ivask, I. Blinova, H. – C. Dubourguier, A. Kahru. Toxicity of nanosized and bulk ZnO, CuO and TiO2 to bacteria Vibrio fischeri and crustaceans Daphnia magna and Thamnocephalus platyurus. Chemosphere 71 (2008), pp. 1308–1316.

[170] L. Zhang, Y. Ding, M. Povey, D. York. ZnO nanofluids – A potential anti-bacterial agent. Progress in Natural Science 18 (2008), pp. 939–944.

[171] A. Awad, A. I. Abou-kandil, I. Elsabbagh, M. Elfass, M. Gaafar, E. Mwafy. Polymer nanocomposites part 1: Structural characterization of zinc oxide nanoparticles synthesized via novel calcination method. Journal of Thermoplastic Composite Materials 28 (2015), pp. 1343–1358.

[172] Y. H. Leung, C. M. N. Chan, A. M. C. Ng, H. T. Chan, M. W. L. Chiang, A. B. Djurisic, Y. H. Ng, W. Y. Jim, M. Y. Guo, F. C. C: Leung, W. K. Chan, D. T. W. Au. Antibacterial activity of ZnO nanoparticles with a modified surface under ambient illumination. Nanotechnology 23 (2012) pp. 475703.

[173] A. A. Ramos, A. Azqueta, C. Pereira-Wilson, A. R. Collins. Polyphenolic Compounds from Salvia Species Protect Cellular DNA from Oxidation and Stimulate DNA Repair in Cultured Human Cells. Journal of Agricultural and Food Chemistry 58 (2010), pp. 7465–7471.

[174] Y. Li, J. Niu, W. Zhang, L. Zhang, E. Shang. Influence of Aqueous Media on the ROS-Mediated Toxicity of ZnO Nanoparticles toward Green Fluorescent Protein-Expressing Escherichia coli under UV-365 Irradiation. Langmuir 30 (2014), pp. 2852–2862.

[175] J. Du, J. M. Gebicki. Proteins are major initial cell targets of hydroxyl free radicals. The International Journal of Biochemistry & Cell Biology 36 (2004), pp. 2334–2343.

[176] O. Yamamoto, M. Komatsu, J. Sawai, Z. Nakagawa. Effect of lattice constant of zinc oxide on antibacterial characteristics. Journal of Materials Science: Materials in Medicine 15 (2004), pp. 847–851.

[177] K. Hirota, M. Sugimoto, M. Kato, K. Tsukagoshi, T. Tanigawa, H. Sugimoto. Preparation of zinc oxide ceramics with a sustainable antibacterial activity under dark conditions. Ceramics International 36 (2010), pp. 497–506.

[178] K. Li, Y. Chen, W. Zhang, Z. Pu, L. Jiang, Y. Chen. Surface Interactions Affect the Toxicity of Engineered Metal Oxide Nanoparticles toward Paramecium. Chemical Research in Toxicology 25 (2012), pp. 1675–1681.

[179] K. H. Tam, A. B. Djurišić, C. M. N. Chan, Y. Y. Xi, C. W. Tse, Y. H. Leung, W. K. Chan, F. C. C. Leung, D. W. T. Au. Antibacterial activity of ZnO nanorods prepared by a hydrothermal method. Thin Solid Films 516 (2008), pp. 6167–6174.

[180] P. Chen, B. A. Powell, M. Mortimer, P. C. Ke. Adaptive Interactions between Zinc Oxide Nanoparticles and Chlorella sp. Environmental Science & Technology 46 (2012), pp. 12178–12185.

[181] O. Yamamoto. Influence of particle size on the antibacterial activity of zinc oxide. International Journal of Inorganic Materials 3 (2001), pp. 643–646.

[182] B. G. Applerot, A. Lipovsky, R. Dror, N. Perkas, Y. Nitzan, R. Lubart, A. Gedanken. Enhanced Antibacterial Activity of Nanocrystalline ZnO Due to Increased ROS-Mediated Cell Injury. Advanced Functional Materials 19 (2009), pp. 842–852.

[183] D. Yan, G. Yin, Z. Huang, L. Li, X. Liao, X. Chen, Y. Yao, B. Hao. Cellular Compatibility of Biomineralized ZnO Nanoparticles Based on Prokaryotic and Eukaryotic Systems. Langmuir 27 (2011), pp. 13206–13211.

[184] M. Janczarek, E. Kowalska. On the Origin of Enhanced Photocatalytic Activity of Copper-Modified Titania in the Oxidative Reaction Systems. Catalysts 7 (2017), 317.

[185] W. Zheng, R. Ding, X. Yan, G. He. PEG induced tunable morphology and band gap of ZnO. Materials Letters 201 (2017), pp. 85–88.

[186] F. M. Omar, H. A. Aziz, S. Stoll. Stability of ZnO Nanoparticles in Solution. Influence of pH, Dissolution, Aggregation and Disaggregation Effects. Journal of Colloid Science and Biotechnology 3 (2014), pp. 1–10.

Tampereen teknillinen yliopisto
PL 527
33101 Tampere

Tampere University of Technology
P.O.B. 527
FI-33101 Tampere, Finland

ISBN 978-952-15-4265-7
ISSN 1459-2045